International Journal of Antennas and Propagation

Antenna Measurement Systems and Antenna Technology for Next Wireless Generation

Guest Editors: Juan F. Valenzuela-Valdes, Sara Burgos, Alfonso Muñoz-Acevedo, and Pablo Padilla

Antenna Measurement Systems and Antenna Technology for Next Wireless Generation

International Journal of Antennas and Propagation

Antenna Measurement Systems and Antenna Technology for Next Wireless Generation

Guest Editors: Juan F. Valenzuela-Valdes, Sara Burgos, Alfonso Muñoz-Acevedo, and Pablo Padilla

Editorial Board

Contents

Antenna Measurement Systems and Antenna Technology for Next Wireless Generation, Juan F. Valenzuela-Valdes, Sara Burgos, Alfonso Muñoz-Acevedo, and Pablo Padilla
Volume 2013, Article ID 527582, 2 pages

Over-the-Air Testing of Cognitive Radio Nodes in a Virtual Electromagnetic Environment, Rajesh K. Sharma, Wim Kotterman, Markus H. Landmann, Christopher Schirmer, Christian Schneider, Frank Wollenschläger, Giovanni Del Galdo, Matthias A. Hein, and Reiner S. Thomä
Volume 2013, Article ID 945283, 16 pages

MIMO OTA Testing Based on Transmit Signal Processing, Jesús Gutiérrez, Jesús Ibáñez, and Jesús Pérez
Volume 2013, Article ID 670154, 7 pages

An Application of Artificial Intelligence for the Joint Estimation of Amplitude and Two-Dimensional Direction of Arrival of Far Field Sources Using 2-L-Shape Array, Fawad Zaman, Ijaz Mansoor Qureshi, Junaid Ali Khan, and Zafar Ullah Khan
Volume 2013, Article ID 593247, 10 pages

Adaptive Prediction of Channels with Sparse Features in OFDM Systems, Changwei Lv, Shujuan Hou, and Wenbo Mei
Volume 2013, Article ID 649602, 5 pages

Implementation of a Zero-Forcing Precoding Algorithm Combined with Adaptive Beamforming Based on WiMAX System, Hyunwook Yang and Seungwon Choi
Volume 2013, Article ID 976301, 7 pages

An Antenna Measurement System Based on Optical Feeding, Ryohei Hosono and Ning Guan
Volume 2013, Article ID 528950, 9 pages

A Compact Printed Quadruple Band-Notched UWB Antenna, Xiaoyin Li, Lianshan Yan, Wei Pan, and Bin Luo
Volume 2013, Article ID 956898, 6 pages

Limits on Estimating Autocorrelation Matrices from Mobile MIMO Measurements, Tricia J. Willink
Volume 2013, Article ID 345908, 6 pages

Hindawi Publishing Corporation
International Journal of Antennas and Propagation
Volume 2013, Article ID 527582, 2 pages
http://dx.doi.org/10.1155/2013/527582

Editorial

Antenna Measurement Systems and Antenna Technology for Next Wireless Generation

Juan F. Valenzuela-Valdes,[1] Sara Burgos,[2] Alfonso Muñoz-Acevedo,[3] and Pablo Padilla[4]

[1] *Departamento de Ingeniería de Sistemas Informáticos y Telemáticos, University of Extremadura, 06800 Mérida, Spain*
[2] *ORBIT/FR Europe GmbH, 85591 Vaterstetten, Germany*
[3] *Intel Mobile Communications, RF System Engineering, 85579 Neubiberg, Germany*
[4] *University of Granada, Departamento de Teoría de la Señal, Telemática y Comunicaciones, 18071 Granada, Spain*

Correspondence should be addressed to Juan F. Valenzuela-Valdes; juanvalenzuela@unex.es

Received 17 July 2013; Accepted 17 July 2013

Technologies introduced in next wireless generation, such as spatial multiplexing, transmit and receive diversity, and beamforming, are key components for providing higher peak rate and better system efficiency, which are essential for supporting future broadband data service over wireless links. Moreover, the multiple-input multiple-output (MIMO) has been a hot research topic in recent years [1], as it has been widely adopted by wireless standards such as LTE, HSPA, and WiMAX. New tests systems and antenna solutions have been proposed in order to achieve and validate the demanding features of the next generation systems. Major challenges remain in the field of measuring systems as well as in the design of new antennas for MIMO systems. In addition, it is also necessary to pay attention to channel modeling for these systems.

In this special issue, researchers from both academia and industry contribute to innovative research and future trends of this scientific area. These papers promote the exchange of information and the advancement both in measurement techniques as in terminal performance predictions for the next generation of wireless handsets.

This special issue contains 8 papers that gather some of the recent advancements in antenna measurement systems and antenna technology for the next wireless generation.

Regarding system design, the paper entitled "*An antenna measurement system based on optical feeding*" presents a radiation measurement system by using optical feeding. The system replaces conventional electrical feeding to antennas by the optical feeding which is composed of an electrical/optical (E/O) converter, a graded-index (GI) optical fiber, and an optical/electrical (O/E) converter. The paper entitled "*A compact printed quadruple band-notched UWB antenna*" presents a novel compact coplanar waveguide-(CPW-) fed ultra-wideband (UWB) printed planar volcano-smoke antenna (PVSA) with four band notches for various wireless applications.

Considering channel prediction and estimation, the paper entitled "*Adaptive prediction of channels with sparse features in OFDM systems*" presents a time domain channel prediction method exploiting features of sparse channel for orthogonal frequency division multiplexing (OFDM) systems. In this paper, the proposed prediction method is compared with the classical frequency domain method realized at each OFDM subcarrier and demonstrates that the proposed method increases the prediction accuracy and reduces the computational complexity. The paper entitled "*Limits on estimating autocorrelation matrices from mobile MIMO measurements*" presents a complete study about MIMO channel responses from mobile measurements in an urban microcell and the limits on estimating autocorrelation matrices.

In relation to multiple-input multiple-output over-the-air (MIMO OTA) systems [1], the paper entitled "*MIMO OTA testing based on transmit signal processing*" proposes a simple methodology that allows over-the-air (OTA) MIMO testing using a MIMO testbed solely, avoiding the use of channel

emulators. The method is fully flexible, so it is able to emulate any equivalent baseband narrowband MIMO channel by adequately selecting the weights of the linear combination. To prove its feasibility, the method has been tested over a commercial MIMO testbed. The paper entitled "*Over-the-air testing of cognitive radio nodes in a virtual electromagnetic environment*" provides an overview of ongoing research in OTA testing for next generation communication and data transmission devices with special consideration of cognitive radio (CR). Existing state-of-the-art techniques and their merits and limitations are discussed.

Finally, regarding pattern optimization and adaptive beamforming the paper entitled "*An application of artificial intelligence for the joint estimation of amplitude and two-dimensional direction of arrival of far field sources using 2-L-shape array*" proposes some artificial intelligence techniques, based on genetic algorithms [2] and simulated annealing, as global optimizers assisted with rapid local version of pattern search for optimization of the adaptive parameters. The paper entitled "*Implementation of a zero-forcing precoding algorithm combined with adaptive beamforming based on WiMAX system*" proposes a novel precoding algorithm that is a zero-forcing (ZF) method combined with adaptive beamforming in the Worldwide Interoperability for Microwave Access (WiMAX) system. This adaptive beamforming algorithm is used to achieve the desired SNR gain. It is verified the feasibility of the proposed method for realizing a practical WiMAX base station to utilize the channel resources as efficiently as possible.

Juan F. Valenzuela-Valdes
Sara Burgos
Alfonso Muñoz-Acevedo
Pablo Padilla

References

[1] M. Á. García-Fernández, J. D. Sánchez-Heredia, A. M. Martínez-González, D. A. Sanchez-Hernandez, and J. F. Valenzuela-Valdes, "Advances in mode-stirred reverberation chambers for wireless communication performance evaluation," *IEEE Communications Magazine*, vol. 49, no. 7, pp. 140–147, 2011.

[2] J. D. Sánchez-Heredia, M. Grudén, J. F. Valenzuela-Valdés, and D. A. Sanchez-Hernandez, "Sample-selection method for arbitrary fading emulation using mode-stirred chambers," *IEEE Antennas and Wireless Propagation Letters*, vol. 9, pp. 409–412, 2010.

Hindawi Publishing Corporation
International Journal of Antennas and Propagation
Volume 2013, Article ID 945283, 16 pages
http://dx.doi.org/10.1155/2013/945283

Research Article

Over-the-Air Testing of Cognitive Radio Nodes in a Virtual Electromagnetic Environment

Rajesh K. Sharma,[1,2] Wim Kotterman,[3] Markus H. Landmann,[4] Christopher Schirmer,[2,3] Christian Schneider,[1] Frank Wollenschläger,[5] Giovanni Del Galdo,[2,3] Matthias A. Hein,[2,5] and Reiner S. Thomä[1,2]

[1] *Electronic Measurement Research Lab, Institute for Information Technology, Ilmenau University of Technology, Helmholtzplatz 2, 98684 Ilmenau, Germany*
[2] *International Graduate School on Mobile Communications, Ilmenau University of Technology, Helmholtzplatz 2, 98684 Ilmenau, Germany*
[3] *Digital Broadcasting Research Lab, Institute for Information Technology, Ilmenau University of Technology, Helmholtzplatz 2, 98684 Ilmenau, Germany*
[4] *Fraunhofer Institute for Integrated Circuits IIS, 9I058 Erlangen, Germany*
[5] *RF and Microwave Research Lab, Institute for Information Technology, Ilmenau University of Technology, Helmholtzplatz 2, 98684 Ilmenau, Germany*

Correspondence should be addressed to Rajesh K. Sharma; rajesh-kumar.sharma@tu-ilmenau.de

Received 1 March 2013; Revised 17 June 2013; Accepted 18 June 2013

Academic Editor: Sara Burgos

This paper provides an overview of ongoing research in over-the-air (OTA) testing for next-generation communication and data transmission devices with special consideration of cognitive radio (CR). Existing state-of-the-art techniques and their merits and limitations are discussed. We identify the requirements and issues for the OTA test in a virtual electromagnetic environment (OTA*in*VEE) which needs to address the more complex scenario of future networks, where interference emulation becomes a highly challenging task. A complex interference scenario arises due to the attempt to simultaneously utilize several opportunity dimensions such as frequency, time, direction (space), and polarization, in a dynamic manner in a multiuser scenario. Although MIMO-OTA testing addresses many limitations of single antenna-conducted test systems, more dimensions and parameters to be addressed in the new scenarios imply further increase in cost and complexity. Closed-loop OTA test setups for CR evaluation are discussed along with an overview of other test scenarios.

1. Introduction

There is a constant quest that communication devices in daily use comply with user quality of service (QoS) requirements and regulations. To ensure this, their performance must be tested under realistic operating conditions. Although testing in a real environment, that is, through field tests, provides the full evaluation of the device for that particular environment, such testing should be repeated for each new environment, each new test condition, and for each new device under test (DuT). This is not practical since such tests are very expensive in terms of cost, planning, and effort, reproducibility of the results is difficult to achieve, and experimenting in live radio networks has obvious disadvantages in terms of interference and licensing. OTA testing in the context of this paper is an evaluation method performed in an emulated virtual electromagnetic environment (VEE) created in a shielded chamber, which approximately mimics the properties of a real environment. We, therefore, prefer to term the test system "OTA*in*VEE." Throughout this paper, if only the term OTA is used, it should be interpreted as OTA*in*VEE. Since the test is performed under controlled conditions, arbitrary

environments can be emulated in a reproducible way without the risk of interfering operational systems and without the need for licensing.

Future-generation radio communication technologies like LTE-A, WiMAX evolution (IEEE802.11m), and WLAN with MIMO (IEEE802.11n) employ MIMO transfer principles for increased throughput. The potential gain of MIMO, by multiple independent data streams at the same frequency and location, can only be realized through the use of multiple antennas on the transmitter and receiver sides of the radio link in combination with the spatiotemporal characteristics of the radio environment. Shunting the antennas like that done in conducted testing removes this vital aspect of MIMO communications. In contrast, in the VEE of OTA test setups, the MIMO capabilities of multiantenna devices can be assessed for realistic environments. Additionally, OTA test systems can be employed for evaluating terminals in networks that have not yet been rolled out.

The main use cases for OTA tests considered in this paper are those radio systems that use MIMO transfer, for example, 802.11n or WIMAX mobile, LTE-A and beyond, and cognitive radio (CR) devices. Note that CR functionality for LTE Advanced is already foreseen, like carrier aggregation. Cognitive devices are listed while, since the second decade of CR research has already begun [1], it is time to pay due attention to OTA evaluation of CR terminals. In this regard, the verification that secondary transmissions of CR devices do not cause detrimental interference to primary users (PU) will be a focus of this paper. Such proof is urgently needed for convincing PU and/or regulators that CR devices will comply with regulations under practical circumstances.

In recent years, joint research efforts in MIMO-OTA have been undertaken for standardization purposes for LTE and LTE-A. For example, the Wireless Association (CTIA), the Third-Generation Partnership Project (3GPP RAN WG4), and the European COST2100 and COST IC1004 projects are involved in such activities. The earlier standardized single-input-single-output OTA (SISO-OTA) testing for GSM and UMTS (resulting from similar joint efforts) was relatively straightforward while purely a function of the device, but MIMO-OTA testing has to incorporate the interaction between the propagation characteristics of the radio channel and the receive (Rx) antennas of the DuT [2] and assesses system performance, not only system-relevant device properties. Additional challenges for the test system are posed when addressing the combined effect of multiple antennas and special algorithms that dynamically change the RF performance of the device [3].

Important issues in the literature connected to the above-mentioned standardization are channel emulation aspects and simplified test methodologies [4–13]. Also, state-of-the-art techniques were developed and commercial products became available for OTA tests of SISO and MIMO. We will expand on this, in a later section.

In contrast, consideration of the uplink (mobile terminal to base station) in OTA testing is generally lacking in the literature. Emulation of the uplink is necessary for assessing the performance of any bidirectional radio communication system, especially when operating in multiuser interference scenarios. In this context, to the best of our knowledge, only few papers on OTA testing of CR equipment have appeared in the literature, and no mature study is available. Emulation of the uplink under realistic channel conditions is crucial for testing CR performance as this is the link on which the DuT may potentially interfere with PU while communicating with other secondary users (SU). This requires accurate emulation of the uplink channels for PU and SU. Of the available papers, an OTA test strategy for evaluating CR nodes has been presented in [14], in which the activities of PU and SU are emulated with respect to received power spectral densities and spatial structures of their radio channels. In order to cope with the complexity, a multilevel test procedure has been proposed to implement different levels of increasing complexity in terms of the operation modes of the DuT, the accuracy of emulation of the radio environment, and the allowed complexity of the test setup. In [15], a test-bed based on a software-defined radio and an OTA test environment has been proposed to analyze the performance of an energy-based sensing algorithm in multiple bands and different directions, enabling reconstruction of PU and SU activities in an authentic radio environment. Realistic OTA simulation of multiuser interference has, however, not been addressed in existing work yet. In this respect, also state-of-the-art equipment has limited resources regarding the number of dimensional variables for spanning emulation space. For instance, most of the setups aim at single-band scenarios with nondirectional resources. Our requirement, however, is a setup for scenarios where multiple communication nodes with multiple transmission policies and standards (PU and SU), equipped with multiple antennas looking for opportunities in multiple directions, coexist at the same geographical location [16, 17]. In sum, the aspects that account for complexity in OTA testing of CR comprise the following:

(i) simultaneous use of multiple frequency bands, either as intrinsic system feature, for example, in cellular systems or secondary use by cognitive systems,

(ii) multiple users, not necessarily at the same location, meaning that determining the system response for a single user does not suffice as loading the system generally changes its characteristics,

(iii) radio channel characteristics including time-variant multipath propagation for multiple communication entities; in particular systems that do not operate in free space suffer or take benefit from the radio channel variations due to reflection, scattering, diffraction, Doppler shift, and so forth,

(iv) spectral and angular dispersion and spatial/temporal variations experienced by systems that themselves are nonstationary or reside in nonstationary environments,

(v) antenna-environment interactions: as an example, for MIMO systems, the transmit (Tx) and Rx antenna arrays determine to which degree the multiplexing potential of the channel can be realized and/or exploited,

(vi) the activity patterns of different communication entities, for example, spectral occupation, including output power, activity factor and temporal traffic distribution, and spatial distribution.

Please note that the consequence of adding all these dimensions to the problem adds to an ever-increasing complexity, which is the main reason to propose the multilevel scheme for OTA testing mentioned earlier [14].

The remainder of the paper is organized as follows: Section 2 provides a general overview of OTA testing addressing the requirements of the testing solution, followed by Section 3 on state-of-the-art methods and equipment. Section 4 discusses OTA setups for the complex closed-loop test scenario in which both uplink and downlink channels are emulated, which is essential especially for CR evaluation. The hardware and calibration issues are also discussed in this section. Section 5 discusses some other scenarios and use cases for OTA testing and the required modifications. Concluding remarks are given in Section 6.

2. OTA Testing Basics

A typical multipath communication scenario with the corresponding parameters of interest is shown in Figure 1. To address OTA testing in such a complex scenario, we introduce a layered measurement procedure, schematically drawn in Figure 2. The lowest layer is the OTA installation, including all the mapping of signals onto the OTA channels and antennas. The second layer deals with the propagation layer, differentiating between single-user and multiuser propagations, the latter needing multiple propagation models. In both cases, the propagation models used may differ according to scenario and/or required model complexity. The third layer is the radio layer including the PHY access schemes. It could also distinguish between single-user and multiuser, although the current level of OTA seems still to be single-user. The additional users in the multiuser scenario could be cooperative or interacting ones, but the multiuser influence could also be emulated by additive interference, markedly reducing the emulation overhead. The fourth layer describes the changes in scenario, propagation environment, user activity, user behavior, and so forth. The fifth layer performs overall measurement control, including retrieving performance parameters and producing condensed performance figures. By presenting this layered scheme, some confusion may arise with the well-known standardized OTA procedures for total reference sensitivity (originally: total isotropic sensitivity) and total radiated power in GSM and UMTS. However, these first OTA procedures are not tests of system performance but of (performance relevant) system parameters [18, 19]. We emphasize the system aspect because, as explained in Section 1, OTA is an overall assessment of DuT, like terminals or other radio system entities, not of their constituting parts. One consequence of testing the performance of systems is that the DuT is tested in operational mode and that the tests must be performed in real time. Like mentioned earlier, "operational" also means the tests must be bidirectional, involving both uplink and downlink. Testing radio systems in operational mode calls for emulating radio environments in such a way that, through its antennas, the DuT will not notice the difference between being exposed to emulated fields and operating in a real radio environment. Therefore, as mentioned in Section 1, the OTA emulation should provide a VEE.

A typical implementation of an OTA test setup for the single-user downlink scenario for mobile communication user equipment (UE) is depicted in Figure 3. Scenario control and signal generation are taken care of by a base-station emulator or mobile communications test set that provides system specific base-band measurement sequences, including the scenario-specific protocol handling, that are modulated onto an appropriate carrier. Then, channel emulators (real-time wideband time-variant filter devices) impose temporal dispersion onto the output signals of test set, much like in conducted tests. In an alternative embodiment, the signal exchange between test set and channel emulators is at base-band level, requiring the channel emulators to provide the generation of RF signals. The channel emulators drive the OTA antennas that, stemming from the similarity with the near-field antenna measurement practice, are often referred to as "probes." The OTA antennas radiate the fields that through superposition have to render a well-defined resultant field in the center of the antenna configuration. The field emulation will be discussed later. Because of the potentially very wide angular distributions of the multipath components in the mobile channel, OTA antenna arrays typically are annular. In order to allow protocol handling/system control and to transport measurement results of the UE performance back to the measurement device, some form of return channel must be provided. Usually, this is realized by a small pick-up antenna outside the OTA ring, effectively a line-of-sight (LoS) uplink.

An important parallel exists between virtual electromagnetic environments and acoustical wave field synthesis. The latter creates a virtual acoustic reality, in which the position and character of sound sources can be manipulated at will, as well as the acoustic properties of the room [20]. When done well, a human observer is not able to tell whether the soundscape is artificial or real. One major difference, though, is that acoustic perception is a subjective one, whereas in electromagnetics, objective evaluation is required, which demands objective metrics for emulation accuracy. On the other hand, this does not mean that in a VEE, the emulation accuracy metric is independent of the properties of the DuT. In particular the effective aperture of the antennas of the DuT, determining its angular resolution, should be taken into consideration. For instance, fast variations over angle in the emulated field, that is, field components with high spatial frequencies, will not excite strong responses from small apertures (e.g., of the order of a wavelength or smaller). As a result, emulation errors at high spatial frequencies are less important than errors at the lower spatial frequencies.

2.1. Emulation of Wave Fields in Downlink Scenarios. When considering OTA emulation of complex incoming wave fields for downlink scenarios, two main emulation principles can be discerned:

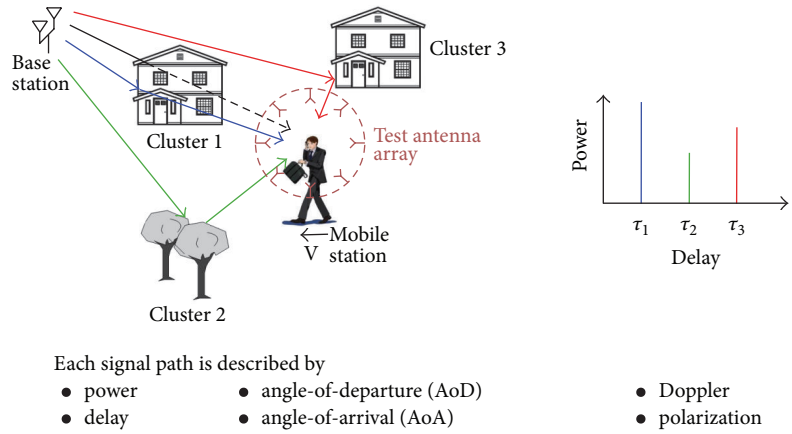

Figure 1: A typical multipath scenario and parameters to be considered in OTA emulation in a virtual electromagnetic environment (OTA*in*VEE).

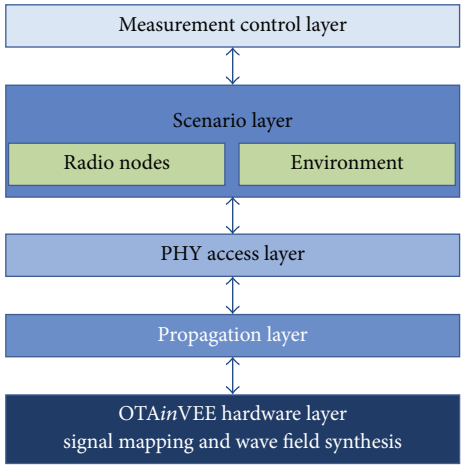

Figure 2: A layered measurement procedure for OTA emulation in a virtual electromagnetic environment (OTA*in*VEE).

(1) Wave field synthesis (WFS), emulating accurate wave fronts,

(2) emulation of (second-order) spatiotemporal statistics of the wave field.

2.1.1. Wave Field Synthesis. With the first principle, by the use of wave field synthesis, the field is emulated in an anechoic chamber as a superposition of discrete wave components; such decomposition is well known for the modeling of mobile radio channels. Wave fronts with a particular direction are emulated by coherent superposition of elementary waves, radiated by several antennas, each with different delays and complex amplitudes, as illustrated by Figure 4. The units controlling the signal fed to the antennas are channel emulators/fading generators similar to those used in conducted tests, one for every OTA antenna.

2.1.2. Generation of Statistical Moments of the Field. The second emulation principle builds on a popular practice in fading generators for (software) simulation of mobile communication systems and is applied to OTA testing of mobile equipment too. There are two implementations of this approach. One is the "prefaded signals synthesis" in setups very similar to those for wave field synthesis. A proprietary form of it described by Kyösti et al. aims at reproducing the spatial correlation function for the specific scenario [8], by generating random components, with an optimization procedure to make sure the delay and angular spread of the scenario are achieved with special attention for approximating the spatial correlation function.

The second implementation is by using reverberation chambers (Figure 5), preferably of the stirred-mode type in which the internal standing wave patterns or mode configurations, are continuously and stochastically changed [21]. Averaged over time, the angular spectrum of incoming waves is isotropic. With the aid of additional channel emulators, the power delay profile can be shaped, but how to shape the angular distributions is still an open question [2, 22]. Proponents say averaging over measurement time resembles the DuT response to an averaged field with effectively isotropic incidence (hence, a Rayleigh distribution), but, actually, the result is taken to be the average over many DuT responses to different instantaneous angular spectra, which is not necessarily the same, as the DuT response is strongly non linear. A clear advantage is the lower cost, as the chamber is considerably smaller and fewer generators are required. Emulating the spatiotemporal statistics of radio fields is well suited to deal with highly complex, stochastic fields, but as the statistics are controlled instead of the fields, control is lost over the actual angular spectrum which makes it not suited for testing directional sensing.

2.1.3. Other Methods. Apart from the above-mentioned division, a hybrid principle is proposed, also called the two-stage method [4]. It is applicable in cases where the antenna characteristics of a DuT can be determined independently. This is by no means trivial, especially for small devices; see [4] for details. Determination of the antenna characteristics is the first stage. Then, by projecting the time-variant spatiotemporal distributions of the radio environment onto the antenna

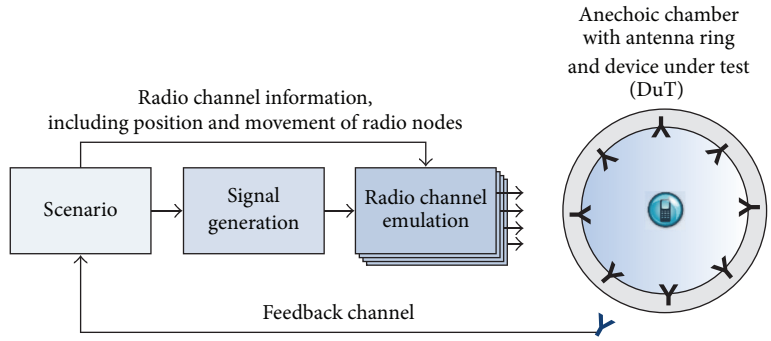

Figure 3: A typical implementation of an OTA*in*VEE test setup for the single-user downlink scenario for mobile communication UE.

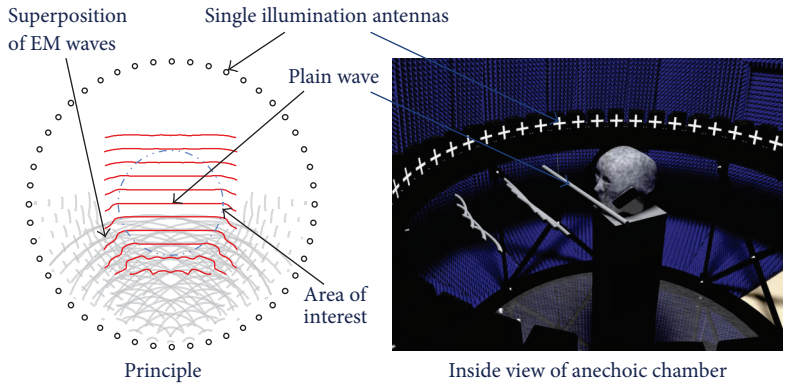

Figure 4: Wave field synthesis for OTA emulation in a virtual electromagnetic environment (OTA*in*VEE).

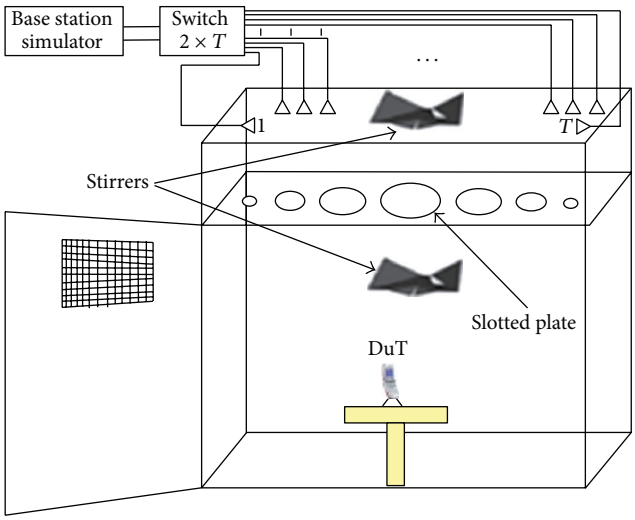

Figure 5: Reverberation chambers with multiple cavities. Reproduced by permission of EMITE Ing.

pattern(s), the time-variant filter is derived that is used to convolve the transmitted data with in order to render the antenna port signals for this particular radio environment, including DuT orientation and data stream(s). The antenna port signals are fed, in a conducted way, to the antenna ports of the DuT, bypassing the antennas. This comprises the second stage. This method is especially suited for larger DuT that do not fit the OTA installation, but only in case antenna patterns can be determined properly. One clear advantage over full OTA is that fewer resources are needed; for instance, no special chambers are required.

Additionally, for mobile communications a two-channel method is proposed [5], but the philosophy behind it is that DuT performance results from the combined performance of antenna(s), front-end, and base-band signal processing. As the latter two purportedly are extremely well tested and probably are very similar among competing products, the aim is assessing antenna performance only, not system performance. In short, according to this philosophy, the second stage of the two-stage method is superfluous. Anyhow, application of the two-channel method to, for instance, CR scenarios is not obvious.

2.2. Testing MIMO Systems in Complex Scenarios. The major difference between OTA testing of MIMO systems and SISO systems is the increased complexity. For each transmitter antenna of a MIMO system, the appropriate incoming fields on the DuT need to be emulated. Because these fields are different, as are the data streams, the required amount of resources for WFS or prefaded signal synthesis has to be multiplied with the number of transmitter antennas. Earlier it was remarked that multiuser (MU) interference could be modeled as an additive stochastic process, but in scenarios for cooperative MIMO, at least additional BS fields have to be emulated. This raises the overall complexity again.

MU scenarios in which multiuser interference cancellation techniques are to be tested call for realistic emulation of other users, require similar emulation strategies. Modeling the interference as a spatially colored stochastic process might not be realistic enough, but even the spatial coloring will demand additional emulation resources. Yet another increase is to be expected with multiband operation, especially if different OTA antennas are needed for the different bands. For emulation in anechoic chambers, the transition from SISO to MIMO will not require additional OTA antennas as long as the sweet spot (i.e., the area over which the field quality can be guaranteed) is commensurate with the size of the DuT. In case also the uplink has to be emulated, yet another increase in complexity is required, as will be discussed later.

For reverberation chambers, more OTA antennas would definitively be necessary. On the other hand, it is still open to research whether MIMO devices can be properly tested in reverberation chambers, one of the main reasons being the difficulty to shape the angular distributions and then multiple of them, according to the properties of transmit antennas and environment [2, 22].

2.3. Channel Models. When speaking about channel models in OTA testing, mainly the same models appear that were also used in the development phase for simulations and often also are the models specified for conformance testing. In the present standardization of MIMO-OTA, the SCME model [23] is a point in case. The model was initially designed by the WINNER project group as an interim solution to aid development of beyond-3G systems until the release of the WINNER model. One of its features is the 100 MHz bandwidth instead of the 5 MHz of the preceding SCM model [24], another that the frequency range runs from 2 to 5 GHz, and a third that the two model scenarios, for urban macrocellular and urban microcellular environments, both have one 6-cluster constellation prescribed; essentially meaning that only one single drop can be generated. The model is two dimensional and single polarized. OTA implementations for OTA ring arrays of eight antennas exist, but the possibilities of using only six OTA antennas have already been investigated too [25]. Not the number of OTA antennas is the problem, but the number of channel emulators equaling the number of OTA antennas. Apart from the anechoic room, the channel emulators are the most expensive parts. Note that emulation of a 2×2 system in a dual-polarized setup with 6 antennas still requires 24 channel emulators (6 antennas times 2 BS fields times 2 polarization directions). Because of this multiplication by two when going from single polarized to dual polarized, the MIMO-OTA community is reluctant to adopt dual-polarized emulation, although the comprehensive channel models WINNER [26] or COST2100 [27] both are full polarimetric. On the other hand, the huge complexity of these models, in terms of the number of individual delay components that have to be emulated, is the reason they are not used in OTA testing. The same applies to measurements, although another reason is that good measurement data are scarce [28].

The comprehensive models also account for the 3D spatial structure of the channel, one that further increases the emulation overhead. In this case, the increase in overhead is caused by the spatial domain, as many more OTA antennas are needed for covering (a part of) a sphere, each requiring a separate channel emulator. However, some attempts have been made to use small 3D-like OTA arrays for increasing the elevation spread of incoming fields, emulating modified IMT-advanced channel models [29]. Predictably, the achievable sweet spot was rather small [30]. On the other hand, a recent study based on measurements shows that simplifications from 3D dual-polarized channels to 2D dual polarized channels, under circumstances, do not greatly impair the realism of the emulation. The two effects in the emulated channel are loss of rank and loss of power. The loss of rank does not seem to be a problem for small MIMO systems, but the loss of power can only be compensated under conditions of perfect power control [31]. However, especially when reducing the 3D full-polarimetric measured data to 2D single polarized, a significant difference in performance can be observed.

3. State-of-the-Art Products and Test Methods in MIMO-OTA

3.1. Brief Literature Review. The major test challenge for MIMO-OTA is creating a repeatable scenario which accurately reflects the MIMO antenna radiation performance in a realistic wireless propagation environment. MIMO-OTA methods differ in the way to reproduce a specified MIMO channel model. In [5], two complementary metrics and corresponding measurement procedures for evaluation of MIMO-OTA performance were presented, in order to address the diversity of possible propagation scenarios. Measurement results from preliminary implementations, including comparison between different LTE devices, were provided.

The channel modeling for MIMO-OTA for small multiple antenna devices along with realistic test challenge has been discussed in [6]. The devices considered were relatively small devices: typically UE, terminal, or laptop device. For the practical performance measurement 802.11n device with 2×2 MIMO was used as a DuT. In [7], the viability of MIMO-OTA test method in terms of creating an appropriate propagation environment in an anechoic chamber was verified in terms of amplitude distribution of fading coefficients, power delay profile, Doppler spectrum, and spatial autocorrelation. The results were compared to theoretical and reference model characteristics considering radio channel models 3GPP SCM, SCME, and IEEE 802.11n or simplifications of them. The authors claimed good agreement between OTA measurements and the reference model in most cases.

In [8], the authors indicated that emulation of a propagation environment inside an anechoic chamber requires unconventional radio channel modeling, namely, a specific mapping of the original models onto the probe antennas. Two methods to generate fading emulator channel coefficients were introduced: the prefaded signals synthesis and the plane-wave synthesis, and simulation results were provided to verify both methods. The plane-wave synthesis for MIMO-OTA was described there as an extension to disciplines of acoustics and electromagnetic plane-wave synthesis as considered in [9]. The authors showed that the geometric description is a prerequisite for the original channel model.

As an important issue related to the cost and complexity of the test system, the authors in [10] reviewed the required number of probes for synthesizing the desired fields inside the multiprobe system and proposed some rules as a function of the test zone size for certain uncertainty levels of the field synthesis. Similarly, [11] presents a theoretical study of the generation of the plane-wave conditions for the MIMO-OTA test zone with a finite number of antennas which lie in the horizontal plane on a circle around the test zone. Relations between the size of the test zone and the accuracy of the plane-wave field due to a finite number of antennas were presented considering different angles of arrival of the plane wave. The authors showed that in the case where the OTA antennas are located in the 90° azimuth angle region with 45° intervals (3 antennas), the test zone diameter is smaller than if the antennas are located in the 360° azimuth angle region with 45° intervals (8 antennas). In [9], the aliasing effect caused by a small number of antennas available in MIMO-OTA setups was discussed.

In wave field synthesis for MIMO-OTA test setups with anechoic chamber, it was reported in [32] that the effective volume of the test zone increases with respect to the shape of the emulated wave fronts through the use of small vertical arrays. Also, the decay of the emulated field over distance has been found reduced. It was suggested to use passive networks for exciting the array elements, such that no additional channel emulators are needed.

In [12], emulation methodology of multiple cluster channels for OTA testing was investigated using a reverberation chamber. This methodology has been used along with the implementation of the single-input-multiple-output (SIMO) LTE standard. It consists of evaluating effective diversity gain level of SIMO LTE orthogonal frequency division multiplex (OFDM) system for different channel models according to the received power, by establishing an active link between the transmitter and the receiver. Significant improvements attained by the implemented system compared to SISO were reported.

Identifying appropriate figures-of-merit is an important aspect for MIMO-OTA evaluation. In [13], some new figures-of-merit, aimed at serving the purpose of evaluating the operators' top priorities for MIMO-OTA compliance testing, were provided based on the LTE MIMO-OTA round robin data from 3GPP. The new figures are MIMO throughput effectiveness, MIMO device throughput effectiveness, MIMO throughput gain, and MIMO device throughput gain.

Apart from the literature, there exist some commercial products and solutions on MIMO-OTA testing. Here, we discuss a few of them regarding their methods and available features. Some important specifications and features are also summarized in Table 1 for convenience. Please note that the specifications in the table are just for information rather than for comparison since a fair comparison is not possible due to their unique characteristics.

3.2. Commercial Products

3.2.1. Elektrobit. It is a MIMO-OTA test solution where flexible configuration for SISO, MISO/SIMO, and MIMO up to 4 × 4 or 8 × 4 are available. It supports 3GPP Release 10 and Release 11 enhancements including carrier aggregation up to 160 MHz, multiple RF bands, coordinated multipoint, and relaying. It provides the channel modeling applications for MIMO, beamforming, multiuser MIMO, smart antenna, and virtual drive testing. It provides integrated uplink and downlink signal separation, meaning there is no need for external duplexers. Both unidirectional and bidirectional fading modes are available and the system is compatible within the Electrobit Propsim product family [33].

3.2.2. Spirent. This MIMO-OTA solution determines the downlink MIMO-OTA performance using an anechoic chamber. The software facilitates comprehensive performance characterization including antenna, RF front-end, and base-band signal processing implementations. Through the characterization of antenna gain or efficiency, branch imbalance, and antenna correlation, for dual-polarized antenna conditions, it enables to precisely characterize the difference between a good and a poor design [34].

3.2.3. SATIMO. Measurement capabilities of their solution [35] include evaluation of receiver diversity-based handsets, evaluation of MIMO performances of WiFi, LTE and WiMAX-based handsets, and emulation of widely standardized 3GPP channel. It employs propagation models in a controlled environment, namely, single cluster, multiple cluster, and uniform. Emulation of variable angles of arrival, angular spread, cross polar ratio (XPR), Doppler, and delay spread are supported. The figures-of-merit are the device throughput in controlled fading environments, channel capacity and bit error rate, and antenna-related parameter characterization such as correlation and diversity gain.

3.2.4. Rohde and Schwarz. The two-channel method was implemented by Rohde and Schwarz for verification of the OTA performance on MIMO devices with a focus on downlink (DL) 2 × 2 MIMO testing for spatial multiplexing and transmit diversity [5, 36]. Measurements of receiver sensitivity and throughput were evaluated with statistical metrics.

The TS8991 MIMO-OTA test system supporting the two-channel method consists of an OTA chamber having three angular positioners to control angles, two test antennas (downlink), and one circularly polarized communication antenna (uplink) integrated in the azimuth positionar. Furthermore, the access panel permits five RF connections to the test antennas placed in the chamber. Two quad-ridged horn antennas are utilized as test antennas, each of which is capable of creating orthogonal components of linearly polarized field.

3.2.5. ETS-LINDGREN. ETS-LINDGREN developed a MIMO-OTA test system (model AMS-8700) for a multipath environment. The simulated environment is suitable for evaluation of downlink MIMO performance for emerging wireless technologies such as LTE, WiMAX, and 802.11n Wi-Fi as well as receiving diversity performance of existing wireless technologies [37].

The system consists of a dual-polarized antenna array in an absorber lined fully anechoic chamber, connected to

Table 1: Summary of some available OTA test solutions.

Solution developer	Chamber type and dimension	Hardware support (available antennas/probes)	Channel model	Frequency range	Other features
Elektrobit [33]	Anechoic	2 × 2 to 8 × 4, up to 32 channels with 48 fading paths per fading channel available	Standard (LTE, ITU 3G), optional including LTE-A evaluation models, dynamic spatially evolving channel modeling	30–2700 MHz, RF interface channel signal BW 40 MHz	Supports carrier aggregation up to 160 MHz, multiple RF bands, coordinated multipoint, and relaying
Spirent [34]	Anechoic	4 to 32 probe layouts	Standard (3GPP, SCM/SCME, WINNER, and ITU) and classical user-defined models	Up to 6 GHz, signal BW 26 MHz (SR5500 Wireless Channel Emulator)	Transmit antenna having single as well as dual polarizations
SATIMO [35]	Anechoic	4 to 32 MIMO dual-polarized probes	Propagation models in a controlled environment (single cluster, multiple cluster, and uniform).	400 MHz to 6 GHz	Positioner feature allowing to choose desired azimuth for testing the DuT in more orientations
Rohde and Schwarz [5, 36]	Anechoic (5 m × 5 m × 5 m)	2 × 2 MIMO downlink	Static channel model	Test results reported for 10 MHz BW (LTE mode) in 0.7 GHz band (TS8991 MIMO-OTA)	Quad-ridged horn antennas, dedicated φ and θ antenna connectors
ETS-Lindgren [37]	Anechoic (4.9 m × 4.9 m × 3.7 m)	Not specified	Specially modified spatial channel models, appropriate Doppler and delay spreads to emulate the scattering effect of fixed and moving objects	700 MHz to 10 GHz (Model AMS-8700)	MIMO dual-polarized environment simulation antennas
Emite Ing [38]	Multimode-stirred reverberation chambers	8 × 8 MIMO Analyzer (Series E100) having ability to test up to 8 radiating element prototypes	Angle of arrival (AoA), angle spread (AS), number of multipath components (MPC), and the eigenvalues considered as channel parameters	Not specified	Different fading scenarios with and without the presence of the user, fast and nonexpensive
Agilent Technologies [39]	Reverberation, anechoic	2 × 2 MIMO	Correlation-based and geometry-based model	Not specified	Two-stage method

technology-specific communication test equipment through a spatial channel emulator. The antenna array transmits downlink signals from a range of angles of arrival (AoA). The spatial channel emulator uses specially modified spatial channel models to feed each antenna in the array with a statistical sampling of the source signal(s) with appropriate Doppler and delay spreads, to emulate the scattering effect of fixed and moving objects. A positioning system allows the wireless DuT to be rotated through the generated field structure, to determine its relative performance in different orientations [37].

3.2.6. EMITE Ing. They have provided a solution for MIMO measurements with a second-generation multimode-stirred chamber. A MIMO measurement service with the 8 × 8 MIMO Analyzer Series E100 is available where up to 8 radiating element prototypes can be tested. Diversity gain, MIMO capacity, efficiency, and other parameters are provided for a variety of fading scenarios with and without the presence of the user. The developers claim that testing with this service could be the only fast and nonexpensive alternative for novel LTE or WiMAX prototypes [38].

3.2.7. Agilent Technologies. The company is mainly involved in research and development of MIMO-OTA with focus on channel models and test methods for measuring the performance of MIMO devices in realistic environments. Results were presented for three OTA methods: the reverberation chamber method, anechoic chamber OTA, and two-stage OTA [39]. The results revealed that although the anechoic chamber method has the flexibility of emulating a variety of multipath conditions and does not require access to the user equipment antenna ports, it can become highly complex and costly to implement especially when dual-polarized measurements are required. This method also has the longest calibration and measurement times as well as the largest chamber requirements compared to other systems. It has been suggested to use a smaller number of probe antennas for reduced complexity and cost, but this makes system accuracy sensitive to calibration and measurement errors [39].

3.3. Noncommercial Test Facilities. There exist also some noncommercial facilities aimed mainly at research in OTA testing. Here we discuss the facilities available in Ilmenau. The important specifications and features of these facilities are also summarized in Table 2 for convenience.

3.3.1. Facility for Over-the-Air Research and Testing (FORTE). Within a collaboration between Ilmenau University of Technology and the Fraunhofer Institute for Integrated Circuits, a Facility for Over-the-Air Research and Testing (FORTE) has been built in Ilmenau which hosts two research platforms in satellite and terrestrial communication, called "SatCom" and "MIMO-OTA" test beds. The MIMO-OTA research is aimed mainly at OTA test methodologies and also meant to actively engage in standardization of OTA practices. Other parts of the research are into wave field synthesis and evaluation of CR nodes. A clear application is to study real-time antenna characteristics of mobile terminals in an OTA test setting. With the projected equipment, a state-of-the-art OTA installation will become available in near future [40]. Some important specifications for the signal generators for the OTA test laboratory are as follows: the connectivity of the OTA test system is 12×32 (physical channels). The signal bandwidth supported is 80 MHz across a frequency range from 350 MHz to 3 GHz (for 4×4 channels up to 18 GHz). For CR two frequency bands with larger separation can be used for emulation, but with instantaneous bandwidth of 80 MHz for each band. the RF output power is +10 dBm. For the generation of the delay characteristics two modes are available:

(i) mode 1: time domain processing similar to tap delay line,

(ii) mode 2: frequency domain processing.

Mode 1 supports 32 taps per physical channel. The delay accuracy better than 30 ps, phase accuracy better than 0.1°, and channel update rate up to 100 kHz are available.

3.3.2. Virtual Road Simulation and Test Facility at Ilmenau University of Technology (VISTA). VISTA is a test facility in Ilmenau similar but less comprehensive compared to the OTA measurement facility FORTE described before. One major activity on this facility is the conception and implementation of the "virtual road." We will discuss more on the motivation and development of this facility in Section 5.

4. Closed-Loop OTA Testing

Most of the products discussed in the former section are specifically designed for testing mobile communication systems in the downlink. However, these systems are bidirectional, meaning, and operating over an uplink too. From testing perspective, at least the protocol handling must be guaranteed, but almost any kind of return channel will suffice to get the protocol messages through, for instance, the small pick-up antenna in the anechoic chamber mentioned earlier. However, this will generally not be satisfactory for assessing system performance. In cellular mobile radio, every system design has to pay special attention to the uplink; therefore, replacing the time-variant and dispersive mobile channel in the uplink by a simple LoS link generally is not realistic.

4.1. Emulation of the Uplink. Emulation of the uplink is based on the same principle as that of the downlink, but effectively in reverse. Receivers are connected to the OTA antennas instead of transmitters; their outputs are filtered by channel emulators and coherently combined onto the Rx connectors of the secondary communication partner or communication tester. A schematic diagram of a closed-loop OTA*in*VEE test-bed realization, incorporating the uplink, is given in Figure 6. More description for this realization including hardware and calibration issues is provided later in this section. Note that in case of emulating MIMO systems, similar to the downlink with respect to the number of transmitters, the required number of channel emulators is multiplied by the number of Rx units of the secondary communication partner or test set. Because the uplink uses WFS too, the receivers should operate in a phase-coherent manner. However, in our experience, manufacturers do not easily promise that their channel emulators operate phase coherently and we expect that purchasing a large phase-coherent set of receivers will prove to be as difficult.

4.2. Practical OTA Setups. Although OTA for LTE-based systems is subject of a large standardization effort, closed-loop testing of LTE is practically impossible at the moment, because no measurement equipment is available that can cope with realistic uplink behavior. As the commercially offered base station (BS) emulators were exclusively designed for connected testing, they are not able to equalize channel fading.

4.2.1. Cognitive Radio Evaluation. The cognitive behavior of the DuT, with respect to relevance for OTA testing, will be interpreted in terms of the cognition cycle as defined by Mitola III and Maguire Jr. [1].

(i) Observe: a CR node performs spectrum sensing to be aware of the surrounding radio environment.

(ii) Orient and plan: the observed data are subjected to intelligent processing.

(iii) Decide: based on the results of the processing, the CR node decides on spectrum opportunities.

(iv) Act: the CR dynamically exploits the opportunities for transmission and avoids interference to PU.

(v) Learn: learning from previous events is a vital capability of CR.

Cognitive abilities numbers (ii), (iii), and (v) are not necessarily tested over the air, but gaining information over these internal states of cognitive nodes has consequences for the OTA setup. Based on the cognitive cycle, we see two different categories of possible OTA tests:

(i) spectrum sensing (observe, orient and plan, and decide),

(ii) secondary link performance (observe, orient and plan, decide, and act).

Table 2: Summary of the OTA test facilities in Ilmenau.

Test facility	Chamber type and dimension	Hardware support (available antennas/probes)	Channel emulation	Frequency range	Other features
FORTE [40]	Anechoic (5 m × 4.5 m × 3.1 m)	12 × 32 (physical channels)	Time domain processing similar to tap delay line (32 taps per physical channel) and frequency domain processing (unlimited fading paths per channel).	350 MHz to 3 GHz (for 4 × 4 channels up to 18 GHz), signal BW 80 MHz	Noncommercial, diverse applications including satellite and terrestrial communications
VISTA [41]	Anechoic (16 m × 12 m × 9 m), max. DuT size = 6 m	Under research	Dynamically evolving geometry-based stochastic channel model	70 MHz to 6 GHz	Noncommercial, combining EMC measurements with OTA testing and vehicular channel emulation

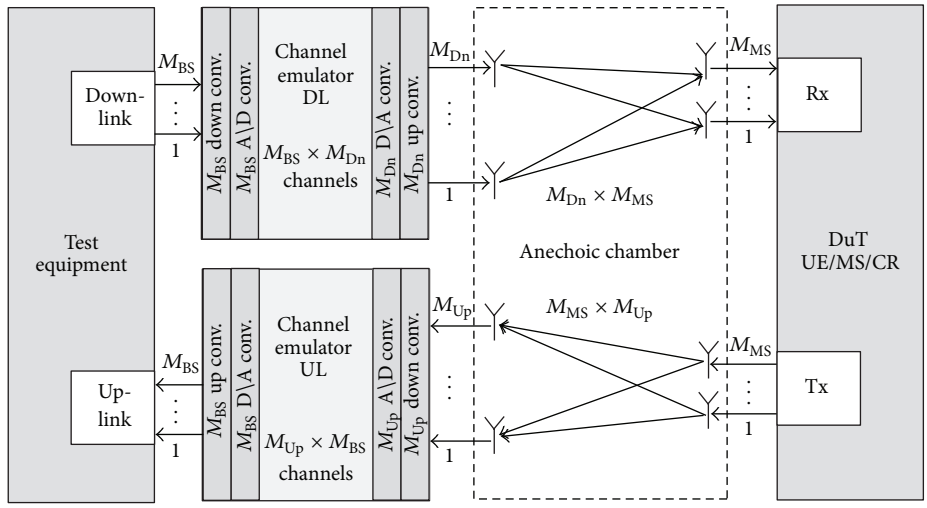

Figure 6: Schematic diagram of a closed-loop OTA setup (OTA*in*VEE) with full emulation of spatiotemporal channels in uplink (UL) and downlink (DL).

Spectrum Sensing. Spectrum sensing is an important component of the cognitive cycle which decides the presence or absence of primary (licensed) users in the spectrum of interest. Some existing spectrum sensing techniques are matched filtering, cyclostationary-based sensing [42, 43], energy detection (ED) [44], and correlation-based sensing [45]. The performance of each detection method in the given environment is to be evaluated for possible acceptance of the method in real CR applications. The performance of spectrum sensing methods is expressed using the receiver operating characteristics (ROC) which describes the relationship between the probability of correct detection (P_d) and the probability of false alarm (P_{fa}) [46].

In addition to the exploitation of conventional resources like frequency and time, some recent works have also considered direction as a potential resource to be exploited by a CR [17]. The evaluation for different sensing methods using omnidirectional as well as directional sensing can be realistically evaluated by OTA testing. For example, in [15], an evaluation of directional sensing using ED-based sensing algorithm in multiple bands has been presented in terms of ROC. The similar evaluation for more realistic multipath and multiuser environment is desired for possible acceptance of the sensing method utilized by CR.

In the case of spectrum sensing, only downlink behavior is tested, so no closed-loop test setup is required. It is even fair to say that the emphasis will be mostly on observe because the other two capabilities can also be tested off-line with software simulations. However, in order to monitor the sensing process, some means of information transfer is needed. Unfortunately, any conductive wire or cable attached to the device will influence the antenna characteristics in a rather unpredictable way. The smaller the device relative to the wavelength, the stronger this influence [47]. Therefore, a wireless, or nongalvanic, data connection is preferred. Using transfer over optical fiber is optimal; otherwise, data have to be stored internally in the device and retrieved off-line while preserving the synchronization between emulated signals and sense data, as this is crucial for evaluation.

As depicted in Figure 7, there might be several PU whose activity behavior has to be described accurately. Statistical models of PU activity have been published (e.g., [48]) that model the activity of radio nodes by binary spectrum occupancy. The use of a realistic statistical user activity

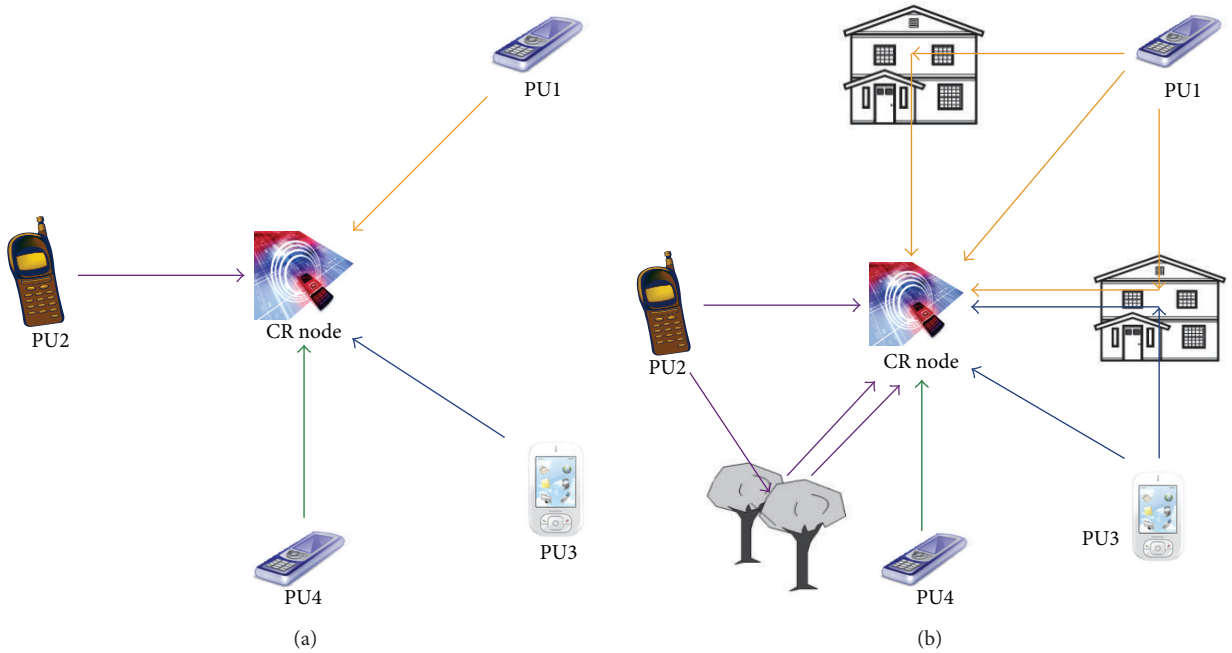

Figure 7: Cognitive radio in two sensing scenarios: LoS (a) and more realistic multipath (b).

model as an emulation basis has the advantage of avoiding playing back large amounts of recorded data when testing the sensing capabilities of the DuT in time-critical applications [49, 50]. The existing models are based on measurements, but, generally, the temporal resolution of the measurements is too low for accurately parameterizing the temporal properties of cellular bands [48, 51, 52]. However, it is possible to perform measurements with sufficient time resolution and to tune the model to a much higher intrinsic accuracy [53].

Secondary Link Performance. The transmissions of CR should not cause harmful interference to PU. Such a system would require SU to accurately detect and react to the varying spectrum usage by the PU network. The effect of secondary communication in the real environment is important to be monitored, which is actually the secondary link performance. In [54], a statistical model for aggregate interference of a cognitive network was proposed. This type of statistical behavior of the cognitive network interference can be tested and verified by using OTA testing. For such a verification, the interference emulation is the most important and challenging task. After the verification of such statistical model, it can be utilized by the OTA test system itself as an information inside the layered measurement procedure described in Figure 2 for further evaluation of the CR node performance. Additionally, any interference mitigation techniques can be evaluated by the system. The ultimate goal is to verify the possibility of coexistence of the primary and CR systems.

Uplink verification is associated with the next logical capability of a CR-Act. A test scenario consisting of secondary transmission in addition to sensing in typical multipath environment is shown in Figure 8. For this, the adaptive transmission should be tested with features as dynamic frequency and power control, adaptive modulation and coding,

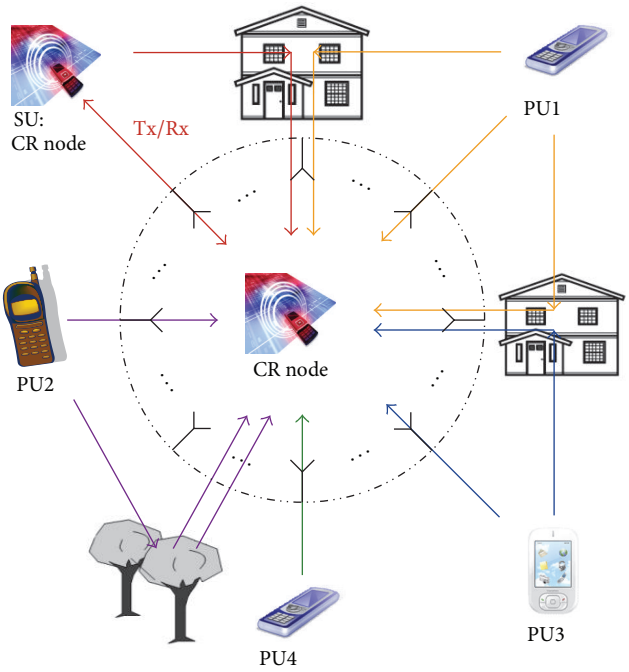

Figure 8: A typical multipath environment to be emulated for the evaluation of CR devices in OTA*in*VEE closed-loop test-bed [14].

and beam-steering. This makes it almost a complete system test and closed-loop testing is indispensable because the uplink is involved. Viable tests regard

(i) the proper exploitation of spectrum opportunities in frequency and/or space,

(ii) the SU tracking of PU with dynamic frequency occupation,

(iii) the sustainable secondary throughput under realistic propagation conditions.

These tests have different requirements. The first two call for measuring the instantaneous angular power spectrum of the CR under test while acting. This requires plane-wave analyses (near-field far-field transformations) of the wave fields radiated by the DuT, not necessarily in real time, as off-line processing is well possible). This requires that the DuT is encircled by OTA antennas for reception like in case of the downlink. The third testing of secondary throughput also requires reception of signals in the uplink by encircling antennas, but real-time processing is needed to impose realistic (spatiotemporal) channel fading onto the signals passed to the secondary communication partner. For the moment we assume that the communication partner of the DuT is passive or that the return link can be some simple LoS link inside the anechoic chamber. Providing a realistic secondary return channel will require many more emulator channel, because the downlink now consists of two different streams: the signals from the PU and the (secondary) return link. A very interesting test would also be the real-time analysis of performance degradation of operational PU by SU interference. However, we have no clue how to perform these tests within a single OTA setup as the channel from one PU to his communication partner differs from the one emulated for the DuT.

A schematic diagram of closed-loop setup of OTA*in*VEE test-bed realization for CR evaluation is shown in Figure 9.

4.2.2. Practical Setups for LTE (Advanced). Despite the fact that realistic tests of operational radio systems require emulation of uplink and downlink radio channels, the state of the art is that the largest standardization effort, that for LTE and LTE-A, is still trying to get grip on the essence of MIMO-OTA testing and deals with downlink aspects only. Additionally, in order not to complicate matters further, the link adaptation mechanisms of the system are suppressed by prescribing specific modulation-and-coding schemes.

4.3. Emulation Hardware. On the market a wide range of channel emulators are available that strongly differ in price, RF accuracy, and available features. Previously they were designed for conducted testing and therefore most of them are limited in output power, which is actually required for OTA. Furthermore, some of the vendors cannot guarantee phase coherence and stability of their outputs especially at elevated output power. For the emulation of the temporal structure of the channel, one typical implementation is a tapped-delay line with a limited number of possible taps and resolution for each signal path. Every individually emulated wave component requires at least one tap position in a number of signal paths. This approach is resource intensive in radio environments with rich multipath. The presence of dense multipath components (DMC) enriches the multipath situation even further [55], but an emulation with the tapped-delay line approach is almost impossible. Therefore, some vendors also offer channel emulators where the convolution of the communication signals with the propagation channel is performed in the frequency domain. This allows for an emulation of a large number of paths.

A further aspect when choosing a channel emulator is its connectivity. For the downlink emulation $M_{\mathrm{BS}} = 2 \cdots 4$ inputs and $M_{\mathrm{Dn}} = 2 \cdots 32$ outputs are commonly available. When considering an uplink emulation with the same quality as that of the downlink, $M_{\mathrm{Up}} = 2 \cdots 32$ inputs and $M_{\mathrm{BS}} = 2 \cdots 4$ outputs are required. The uplink case is therefore most challenging, but mandatory for the test of cognitive devices exploiting directional degrees-of-freedom.

Last but not least, the complexity of the channel (2D, 3D, and full polarization) to be emulated will define the overall connectivity needed for the OTA test setup. As remarked earlier, 3D environments for 2×2 MIMO configurations may be simplified to 2D, as long as the polarization characteristics are kept [31], but for larger MIMO configurations such a simplification will affect channel rank too much. In those cases, the resulting dual-polarized 3D emulation would require an extension of the number of generator outputs (in the downlink) and receiver inputs (in the uplink) to up to 200 channels for a sweet spot of 30 cm in diameter, at around 2 GHz. An extension to such a large number of phase coherent outputs is only available from few vendors, whereas such a large number of inputs are not available at all, to our knowledge. In consequence, this means that an uplink observation as required for CR tests may use different techniques such as channel sounding (fast switching over the angular dimension).

4.4. Calibration of OTA Setups. One crucial point when using the OTA methods, especially the multi-probe method, is the calibration of the setup as this determines the accuracy of the wave field synthesis [56]. As the wave field synthesis requires a coherent superposition of discrete wave components, the phase and amplitude differences of all signal paths $M_{\mathrm{BS}} \times M_{\mathrm{Dn}}$ and $M_{\mathrm{Up}} \times M_{\mathrm{BS}}$ as shown in Figure 6 have to be accounted for in calibration. In the context of phase and amplitude calibration, static and dynamic inaccuracies are relevant. Static differences mainly result from antenna feeds, OTA antennas, antenna positions and antennaalignment, and polarization purity. Dynamic phase and amplitude inaccuracies are mainly caused by phase changes while scanning the sweet spot (bending of RF or even optical fiber cable that is connected to the field probe for calibration) and long-term drift effects of each signal path ($M_{\mathrm{BS}} \times M_{\mathrm{Dn}}$ and $M_{\mathrm{Up}} \times M_{\mathrm{BS}}$) with different drift characteristics. The latter can be reduced to some extent only when carefully considering the temperature stability of the entire cabling arrangement. Note that CR applications additionally require the calibration of each frequency band applied.

Recently, during the inter-laboratory/intertechnique comparison test effort of the CTIA MIMO-OTA Special Group, a serious problem was experienced with the definitions of vital concepts of signal-to-noise ratio (SNR) and received power. Although seasoned experts were dealing with these concepts, at least three different implementations with different measurement outcomes resulted. This urged closer investigations.

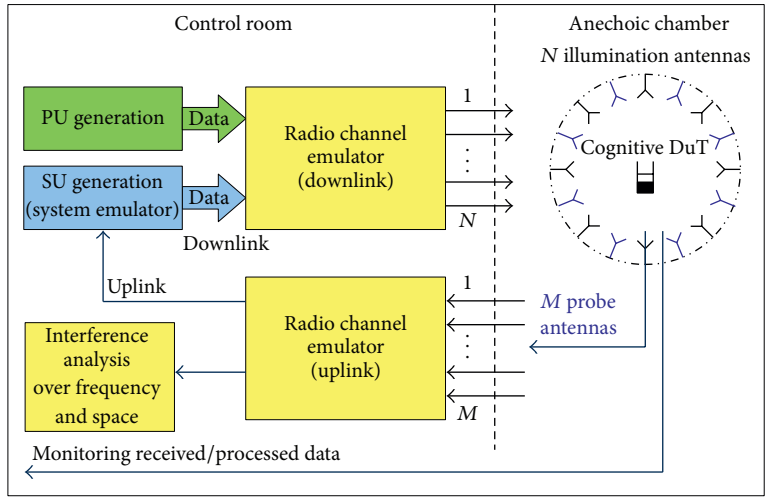

Figure 9: OTA*in*VEE test-bed realization for closed-loop evaluation of CR nodes.

4.5. Channel Modeling Requirements. One key issue for the development and operation of OTA test environments is the provision of application and scenario-specific propagation channel data sets. In the past, various channel models [57] were developed within the European projects COST [58], WINNER [26], or standardization bodies [59]. Furthermore, channel sounding data sets for different evaluation scenarios have gained an increased attraction [60–62]. While first proposals for channel models with focus on vehicle-to-vehicle communication applications [63, 64] have been driven, white spaces can be found in the area of channel models with specific focus to provide broadband directional channel data sets to evaluate CR nodes. A consistent channel model framework for CR applications can be derived from extensions of widely accepted models from 3GPP [59] and WINNER [26].

The main features of a channel model suitable for CR testing are multiband, multilink, and multi-scenario. Multiscenario is very interesting, because a CR node located in an outside environment will receive and hence sense signals from transmitters located above roof top (urban macrocell) and/or below roof top (urban microcell) and/or from nodes located inside a building (indoor to outdoor scenario). Furthermore, nodes located within these different scenarios usually use different communications standards and frequency bands. Therefore, the minimum extension of any current available channel model has to be multi-band and multi-scenario. Note, the uplink channel is likely to be similar to the downlink channel but certainly is not identical in frequency-division duplex (FDD) systems. Even with time-division duplex (TDD) systems, when the channel coherence time becomes short in comparison to the duplex time interval, reciprocity is not guaranteed any longer. A special case is CR, as the essence of secondary communications is not interfering with primary communications. Therefore, the RF activity of cognitive (secondary) systems in the uplink should be thoroughly scrutinized; the more so if the cognitive device uses directional antennas to diminish potential interference. Typically, the signals of the PU will be transmitted on the downlink, with the return link carrying the secondary communications. As secondary communication partners are not colocated with primary transmitters, secondary channels differ from primary ones, although they are on the same frequency.

5. Related Test Scenario: C2C/C2I Communication—Issues and Developments

Recently, channel measurements and test scenarios for Car-to-Car (C2C) and Car-to-Infrastructure (C2I) communications have gained large attraction. The term "Car" can be more generalized by using "vehicl." The embedding of vehicles as nodes into ad hoc and meshed network structures for safety, security, fleet and traffic management, and communication seems to be one key technology for future. Channel models and test methods have to consider the specific requirements of those network structures. The following features play an important role for any considered channel model approach.

(i) Continuous time evolution of the channel: because of the rapidly varying C2C/C2I channel, a continuous evolvement of the channel has to be introduced. With that the models can cover extended evaluation time series.

(ii) Realistic node traffic model: in order to cover long evaluation time series, realistic vehicle traffic models are necessary.

(iii) Joint clusters for different links and scenarios: to introduce realistic time evolution and correlations between emulated multilinks, joint or common clusters between links and even between scenarios (e.g., urban macro and micro) are required.

(iv) Modeling of realistic interference situations: an open issue is the modeling of realistic interference and coexistence situations. In particular, in rapidly changing vehicular scenarios, various and time-dependent interferences from different networks and/or other noncooperative sources (audio and sensing links within vehicles) have to be expected.

Considering high standards for safety and security, the testing of interference management and suppression algorithms for coexistence present major challenges of C2C/C2I communications.

C2C/C2I communications undergo a very rapid development, for example, alluding to the ITS-G5 standard. The issues of coexistence and interference resulting from a great number of equivalent communicating nodes in ad hoc and time-variant networks cannot be overestimated. In addition to propagation aspects and channel modeling, conventional and even more so electric cars comprise a multitude of electric and electronic systems for driver assistance, safety systems, data transmission, intravehicular networks, and radio connectivity to a multitude of services extending from tens of MHz well into the GHz range. Related to these rapid developments, issues of coexistence, interference, inter-operability, and quality assurance demand for measurement techniques, not only reliable conditions irrespective of time, place, region, or climate conditions, but also accounting for the specificities of vehicles. For C2C/C2I communications, accurate and reproducible measurement techniques are as important as or even more important than the multipath wave field synthesis. Typical scenarios can include from tens up to 200 cars, which can never be tested on real road, especially not in repeated manner for changing situations.

The Thuringian Center of Innovation in Mobility (ThIMo) at Ilmenau University of Technology [41] pursues a holistic approach towards solving such challenges related to mobility, with an explicit focus on information and communication technologies. The VISTA test facility is similar but less comprehensive compared to the FORTE described before. This installation aims at combining traditional antenna and electromagnetic compatibility measurement approaches with OTA testing and vehicular channel emulation. Fitting to and complementing with the research already ongoing at the FORTE in Ilmenau, alternative techniques are to be developed, to create synthetic radio environments and evaluate their interdependence with the vehicle, road infrastructure, and driver. The key objective of the approach is to emulate realistic radio scenarios as realistic as possible, possibly in real-time, under well-defined partial or fully anechoic conditions.

The first stage of the VISTA test facility comprises a semi-anechoic chamber and a chassis dynamometer integrated into a turntable. The dynamometer enables emulation of realistic driving scenarios synchronized with electromagnetic synthesis and measurement hardware in addition to electromagnetic compatibility (EMC) measurements of vehicles and powertrain components under operation. Some of the key parameters of the planned implementation are mentioned here. The chamber size is 16 m × 12 m × 9 m and the maximum DuT size is 6 m. The frequency range of operation is 70–6000 MHz, where the velocity up to 120 Km/h has been simulated.

6. Conclusions

This paper has provided an overview of an over-the-air test in virtual electromagnetic environment (OTA*in*VEE) for future communication devices, with the main focus on CR devices operating in highly complex environments with multiple dimensions of parameters, each having multiple elements. A brief survey of state-of-the-art methods and products has been presented. Closed-loop OTA*in*VEE has been discussed with issues related to hardware, calibration, and channel modeling. Some practical OTA scenarios including CR testing and setups have also been presented. Although closed-loop OTA testing is costly and complex, it is inevitable for successful implementation of future systems and for guaranteeing their performance.

Conflict of Interests

The authors would like to state that the aim of this paper is to provide research survey and propose scientific idea on OTA testing of the future communication devices. Markus Landmann has affiliation with Fraunhofer IIS, a research organization in Germany, which has close cooperation with the Ilmenau University of Technology. All the remaining authors have affiliation with the Ilmenau University of Technology and are being involved in research works, without any secondary interest with a particular commercial trademark. The authors have no secondary interest on mentioning the terms like "WIMAX mobile," "3GPP RAN WG4," "GSM," and "WINNER model," which have been taken as examples of the systems, workgroups, and models in the context of OTA testing. In particular, coauthor Wim Kotterman has been involved remotely in the standardization of GSM in the late eighties and has no commercial/financial interests in GSM or other standards. He is neither a member of 3GPP RAN WG4 nor has positions to defend in this committee. Wim Kotterman and Christian Schneider have been involved remotely in the definition of the WINNER model, which is a noncommercial, open-access mobile channel definition sponsored by the European Commission and is available in an open-source implementation. No author sees any conflict of interest from his side regarding the terms used in the paper.

Acknowledgments

The authors would like to thank the administration and members of Thüringer Innovationszentrum Mobilität (ThIMo) and the group of researchers of Powertrain-Radio Train (PORT) for their support and the Thüringer Aufbaubank TAB/ESF and the Carl-Zeiss Foundation for their kind funding.

References

[1] J. Mitola III and G. Q. Maguire Jr., "Cognitive radio: making software radios more personal," *IEEE Personal Communications*, vol. 6, no. 4, pp. 13–18, 1999.

[2] M. Rumney, R. Pirkl, M. H. Landmann, and D. A. Sanchez-Hernandez, "MIMO over-the-air research, development, and testing," *International Journal of Antennas and Propagation*, vol. 2012, Article ID 467695, 8 pages, 2012.

[3] M. D. Foegelle, "Over-the-air performance testing of wireless devices with multiple antennas," *RF Design*, vol. 2012, p. 4452, 2006, http://rfdesign.com/mag/602RFDF4.pdf.

[4] Y. Jing, X. Zhao, H. Kong, S. Duffy, and M. Rumney, "Two-stage over-the-air (OTA) test method for LTE MIMO device performance evaluation," *International Journal of Antennas and Propagation*, vol. 2012, Article ID 572419, 6 pages, 2012.

[5] Y. Feng, W. L. Schroeder, C. Von Gagern, A. Tankielun, and T. Kaiser, "Metrics and methods for evaluation of over-the-air performance of MIMO user equipment," *International Journal of Antennas and Propagation*, vol. 2012, Article ID 598620, 15 pages, 2012.

[6] J. P. Nuutinen, P. Kyösti, Y. Gao, and M. D. Foegelle, "On the MIMO OTA test system," in *Proceedings of the 5th International ICST Conference on Communications and Networking in China (CHINACOM '10)*, pp. 1–5, 2010.

[7] P. Kyösti, J. P. Nuutinen, and T. J. Jämsä, "MIMO OTA test concept with experimental and simulated verification," in *Proceedings of the 4th European Conference on Antennas and Propagation (EuCAP '10)*, April 2010.

[8] P. Kyösti, T. J. Jämsä, and J. P. Nuutinen, "Channel modelling for multiprobe over-the-air MIMO testing," *International Journal of Antennas and Propagation*, vol. 2012, pp. 1–11, 2012.

[9] W. A. T. Kotterman, A. Heuberger, and R. S. Thoma, "On the accuracy of synthesised wave-fields in MIMO-OTA setups," in *5th European Conference on Antennas and Propagation (EUCAP '11),* pp. 2560–2564, April 2011.

[10] A. Khatun, T. Laitinen, V. M. Kolmonen, and P. Vainikainen, "Dependence of error level on the number of probes in over-the-air multiprobe test systems," *International Journal of Antennas and Propagation*, vol. 2012, Article ID 624174, 6 pages, 2012.

[11] T. Laitinen, P. Kyösti, J.-P. Nuutinen, and P. Vainikainen, "On the number of OTA antenna elements for planewave synthesis in a MIMO-OTA test system involving a circular antenna array," in *Proceedings of the 4th European Conference on Antennas and Propagation (EuCAP '10)*, April 2010.

[12] N. Arsalane, M. Mouhamadou, C. Decroze, D. Carsenat, M. A. Garcia-Fernandez, and T. Monedire, "3GPP channel model emulation with analysis of MIMO-LTE performances in reverberation chamber," *International Journal of Antennas and Propagation*, vol. 2012, Article ID 239420, 8 pages, 2012.

[13] A. Marín-Soler, G. Ypia-García, Á. Belda-Sanchiz, and A. M. Martínez-González, "MIMO throughput effectiveness for basic MIMO OTA compliance testing," *International Journal of Antennas and Propagation*, vol. 2012, Article ID 495329, 10 pages, 2012.

[14] A. Krah, M. Grimm, N. Murtaza et al., "Over-the-air test strategy and testbed for cognitive radio nodes," in *Proceedings of the 30th URSI General Assembly and Scientific Symposium (URSIGASS '11)*, August 2011.

[15] M. Grimm, A. Krah, N. Murtaza et al., "Performance evaluation of directional spectrum sensing using an over-the-air testbed," in *Proceedings of the 4th International Conference on Cognitive Radio and Advanced Spectrum Management (CogART '11)*, ACM, New York, NY, USA, 2011.

[16] N. Murtaza, A. Krah, M. Grimm, A. Heuberger, R. Thomä, and M. Hein, "Multi-band direction-sensitive cognitive radio node," in *Proceedings of the 1st IEEE-APS Topical Conference on Antennas and Propagation in Wireless Communications (APWC '11)*, pp. 251–254, September 2011.

[17] N. Murtaza, R. K. Sharma, R. S. Thomä, and M. A. Hein, "Directional antennas for cognitive radio: analysis and design recommendations," *Progress in Electromagnetics Research*, vol. 140, pp. 1–30, 2013.

[18] "Test Plan for Mobile Station Over the Air Performance" CTIA—the Wireless Association, Oct. 2001, http://files.ctia.org/pdf/CTIA.

[19] "Measurements of radio performances for UMTS terminals in speech mode", 3GPP, Oct. 2006, http://www.etsi.org/deliver/etsi.

[20] A. J. Berkhout, "A holographic approach to acoustic control," *Journal of the Audio Engineering Society*, vol. 36, pp. 977–995, 1988.

[21] P. Kildal, X. Chen, C. Orlenius, M. Franzen, and C. S. L. Patane, "Characterization of reverberation chambers for OTA measurements of wireless devices: physical formulations of channel matrix and new uncertainty formula," *IEEE Transactions on Antennas and Propagation*, vol. 60, no. 8, pp. 3875–3891, 2012.

[22] Measurement of radiated performance for Multiple Input Multiple Output (MIMO) and multi-antenna reception for High Speed Packet Access (HSPA) and LTE terminals (3GPP TR 37. 976 version 11. 0. 0 Release 11), European Telecommunications Standards Institute (ETSI), Nov. 2012.

[23] D. S. Baum, J. Hansen, G. Del Galdo, M. Milojevic, J. Salo, and P. Kyösti, "An interim channel model for beyond-3G systems: extending the 3GPP spatial channel model (SCM)," in *Proceedings of the IEEE 61st Vehicular Technology Conference (VTC 2005-Spring '05)*, pp. 3132–3136, June 2005.

[24] Spatial channel model for MIMO simulations, 3GPP, 2003, 3GPP Document TR 25. 996. http://www.3gpp.org/.

[25] Simulation results of simplified SME channel model, 3GPP,Taipei, Taiwan, Feb. 2011, 3GPP TSG-RAN4 58, R4-111425, http://www.3gpp.org/ftp/tsg_ran/WG4_Radio/TSGR4_58/Docs/.

[26] IST-4-027756 WINNER II D1. 1. 2 V1. 2 WINNER II Channel Models, WINNER II, 2008, http://www.cept.org/files/1050/documents/winner2 - final report.pdf.

[27] R. Verdone, Ed., *Pervasive Mobile & Ambient Wireless Communications-the COST Action 2100*, Springer, London, UK, 2012.

[28] C. Schneider, G. Sommerkorn, M. Narandzic et al., "Multiuser MIMO channel reference data for channel modelling and system evaluation from measurements," in *Proceedings of International ITG Workshop on Smart Antennas (WSA '09)*, Berlin, Germany, February 2009.

[29] L. Hentilä, P. Kyösti, and J. Meinilä, "Elevation extension for a geometry-based radio channel model and its influence on MIMO antenna correlation and gain imbalance," in *Proceedings of the 5th European Conference on Antennas and Propagation (EuCAP '11)*, pp. 2175–2179, April 2011.

[30] P. Kyösti and A. Khatun, "Probe configurations for 3D MIMO over-theair testing," in *Proceedings of the 7th European Conference on Antennas and Propagation (EuCAP '13)*, pp. 1421–1425, Gothenburg, Sweden, April 2013.

[31] M. Landmann, M. Grossmann, N. Phatak, C. Schneider, R. Thomä, and G. D. Galdo, "Performance analysis of channel model simplifications for MIMO OTA LTE UE testing," in *Proceedings of the 7th European Conference on Antennas and Propagation (EuCAP '13)*, pp. 1856–1860, April 2013.

[32] W. Kotterman, "Increasing the volume of test zones in anechoic chamber MIMO over-the-air test set-ups," in *Proceedings of the International Symposium on Antennas and Propagation (ISAP '12),* pp. 786–789, November 2012.

[33] User-friendly Emulator for MIMO Performance Testing, Elektrobit (EB), 2012, http://www.elektrobit.com/file.php?id=3298.

[34] Spirent Wireless Channel Emulator- MIMO-OTA Environment Builder, Spirent Communications, 2011.

[35] MIMO Testing Solutions, SATIMO, Microwave Vision Group, 2010.

[36] Two-Channel Method for OTA Performance Measurements of MIMO-Enabled Devices White paper, Rohde & Schwarz, 2011 http://cdn.rohde-schwarz.com/dl_downloads/dl_application/application_notes/1sp12/1SP12_1e.pdf.

[37] AMS-8700 MIMO OTA Test System, ETS-Lindgren, 2012, http://www.ets-lindgren.com/all/MIMOWirelessTestSystem.

[38] MIMO measurements with second-generation multimode-stirred chamber, Emite Ing., 2012.

[39] *Theory, Techniques and Validation of Over-the-Air Test Methods For Evaluating the PerFormance of MIMO User Equipment Application Note*, Agilent Technologies, 2010, http://cp.literature.agilent.com/litweb/pdf/5990-5858EN.pdf.

[40] W. A. T. Kotterman, M. Landmann, A. Heuberger, and R. S. Thomä, "New laboratory for over-the-air testing and wave field synthesis," in *Proceedings of the 30th URSI General Assembly and Scientific Symposium (URSIGASS '11)*, August 2011.

[41] "Thüringer Innovationszentrum Mobilität," 2013, http://www.tu-ilmenau.de/wirtschaft/thimo/.

[42] J. Lundén, V. Koivunen, A. Huttunen, and H. V. Poor, "Collaborative cyclostationary spectrum sensing for cognitive radio systems," *IEEE Transactions on Signal Processing*, vol. 57, no. 11, pp. 4182–4195, 2009.

[43] D. Cabric, "Addressing the feasibility of cognitive radios: using testbed implementation and experiments for exploration and demonstration," *IEEE Signal Processing Magazine*, vol. 25, no. 6, pp. 85–93, 2008.

[44] H. Urkowitz, "Energy detection of unknown deterministic signals," *Proceedings of IEEE*, vol. 55, no. 4, pp. 523–531, 1967.

[45] R. K. Sharma and J. W. Wallace, "Correlation-based sensing for cognitive radio networks: Bounds and experimental assessment," *IEEE Sensors Journal*, vol. 11, no. 3, pp. 657–666, 2011.

[46] S. M. Kay, *Fundamentals of Statistical Signal Processing: Detection Theory*, vol. 2, Prentice Hall, 1998.

[47] W. A. T. Kotterman, G. F. Pedersen, K. Olesen, and P. Eggers, "Cable-less measurement set-up for wireless handheld terminals," in *Proceedings of the 12th International Symposium on Personal, Indoor and Mobile Radio Communications (PIMRC '01),* pp. B112–B116, October 2001.

[48] M. Wellens, J. Riihijärvi, and P. M. Mähönen, "Empirical time and frequency domain models of spectrum use," *Physical Communication*, vol. 2, no. 1-2, pp. 10–132, 2009.

[49] Y. Zhao, S. Mao, J. O. Neel, and J. H. Reed, "Performance evaluation of cognitive radios: metrics, utility functions, and methodology," *Proceedings of the IEEE*, vol. 97, no. 4, pp. 642–658, 2009.

[50] D. Fortin and D. A. Hall, *Test Radio Receivers With Recorded Signals*, 2008, http://mwrf.com/test-and-measurement/test-radio-receivers-recorded-signals.

[51] M. L. López-Benítez, F. Casadevall, D. L. López-Pérez, and A. V. Vasilakos, "Modeling and simulation of joint time-frequency properties of spectrum usage in cognitive radio," in *Proceedings of the 4th International Conference on Cognitive Radio and Advanced Spectrum Management (CogART '11)*, vol. 4, pp. 1–4, ACM, New York, NY, USA, 2011.

[52] L. Mendes, L. Gonçalves, and A. Gameiro, "GSM downlink spectrum occupancy modeling," in *Proceedings of the IEEE 22nd International Symposium on Personal, Indoor and Mobile Radio Communications (PIMRC '11)*, pp. 546–550, September 2011.

[53] C. Schirmer, M. Alsharef, A. Ihlow, G. Del Galdo, and A. Heuberger, "High time resolution spectrum occupancy model for testing of cognitive radio devices," in *Proceedings of the 24th IEEE International Symposium on Personal, Indoor and Mobile Radio Communications*, September 2013.

[54] A. Rabbachin, T. Q. S. Quek, H. Shin, and M. Z. Win, "Cognitive network interference," *IEEE Journal on Selected Areas in Communications*, vol. 29, no. 2, pp. 480–493, 2011.

[55] M. H. Landmann, *Limitations of experimental channel characterisation [Ph.D. dissertation]*, TU Ilmenau, 2008.

[56] W. Fan, X. Carreño, J. O. Nielsen, K. Olesen, M. B. Knudsen, and G. F. Pedersen, "Measurement verification of plane wave synthesis technique based on multi-probe MIMO-OTA setup," in *Proceedings of the IEEE Vehicular Technology Conference (VTC Fall)*, September 2012.

[57] P. Almers, E. Bonek, A. Burr et al., "Survey of channel and radio propagation models for wireless MIMO systems," *EURASIP Journal on Wireless Communications and Networking*, vol. 2007, Article ID 19070, 2007.

[58] *COST Action 2100—Pervasive Mobile & Ambient Wireless Communications*, EU Project, 2011, http://www.cost2100.org/.

[59] "Spatial channel model for Multiple Input Multiple Output (MIMO) simulations (release 7)," 3GPP Document TR 25.996, 3GPP, 2007, http://www.3gpp.org/ftp/specs/html-INFO/25996.htm.

[60] U. Trautwein, C. Schneider, and R. Thomä, "Measurement-based performance evaluation of advanced MIMO transceiver designs," *EURASIP Journal on Applied Signal Processing*, vol. 2005, no. 11, pp. 1712–1724, 2005.

[61] R. S. Thomä, D. Hampicke, A. Richter, G. Sommerkorn, and U. Trautwein, "MIMO vector channel sounder measurement for smart antenna system evaluation," *European Transactions on Telecommunications*, vol. 12, no. 5, pp. 427–438, 2001.

[62] F. Kaltenberger, D. Gesbert, R. Knopp, and M. Kountouris, "Correlation and capacity of measured multi-user MIMO channels," in *Proceedings of the IEEE 19th International Symposium on Personal, Indoor and Mobile Radio Communications (PIMRC '08)*, September 2008.

[63] J. Karedal, F. Tufvesson, N. Czink et al., "A geometry-based stochastic MIMO model for vehicle-to-vehicle communications," *IEEE Transactions on Wireless Communications*, vol. 8, no. 7, pp. 3646–3657, 2009.

[64] A. F. Molisch, F. Tufvesson, J. Karedal, and C. F. Mecklenbräuker, "A survey on vehicle-to-vehicle propagation channels," *IEEE Wireless Communications*, vol. 16, no. 6, pp. 12–22, 2009.

Hindawi Publishing Corporation
International Journal of Antennas and Propagation
Volume 2013, Article ID 670154, 7 pages
http://dx.doi.org/10.1155/2013/670154

Research Article

MIMO OTA Testing Based on Transmit Signal Processing

Jesús Gutiérrez, Jesús Ibáñez, and Jesús Pérez

Department of Communications Engineering, University of Cantabria, 39140 Santander, Spain

Correspondence should be addressed to Jesús Pérez; jperez@gtas.dicom.unican.es

Received 1 February 2013; Revised 17 May 2013; Accepted 19 May 2013

Academic Editor: Pablo Padilla

Usually, multiple-input-multiple-output (MIMO) testbeds are combined with channel emulators for testing devices and algorithms under controlled channel conditions. In this work, we propose a simple methodology that allows over-the-air (OTA) MIMO testing using a MIMO testbed solely, avoiding the use of channel emulators. The MIMO channel is emulated by linearly combining the signals at the testbed transmitter. The method is fully flexible, so it is able to emulate any equivalent baseband narrowband MIMO channel by adequately selecting the weights of the linear combination. We derive closed-form expressions for the computation of such weights. To prove its feasibility, the method has been implemented and tested over a commercial MIMO testbed.

1. Introduction

Multiple-input-multiple-output (MIMO) testbeds [1–3] allow over-the-air (OTA) testing of MIMO devices and algorithms in the laboratory. However, the channels in these indoor scenarios can be quite different from the channels where MIMO systems operate. So, MIMO testbeds are usually combined with MIMO channel emulators for carrying out the tests under desired and controlled channel conditions. However, channel emulators result in an increase in equipment cost. Some OTA emulation methods combine conventional channel emulators with anechoic chambers to fully control the propagation environment [4–6]. These solutions are fully flexible but expensive.

On the other hand, OTA channel emulation can be performed using reverberation chambers where the propagation environment is physically modified to get the desired channel response. Reverberation chambers can work either standing alone [7], or combined with conventional channel emulators [8, 9]. Their main drawbacks are the chamber cost and the lack of flexibility to emulate specific channel realizations. Both methods, based on anechoic and reverberation chambers, are used in combination with a MIMO testbed for MIMO testing.

In this work, we propose a methodology that allows narrowband OTA MIMO testing using the MIMO testbed solely, avoiding the use of channel emulators and additional facilities. It is based on the fact that the MIMO channel encountered in indoor research laboratories can be considered time invariant when the environment is static [10]. In a preliminary stage, this channel must be estimated by the MIMO testbed [10], including the device under test (DUT). Then, during the testing stage, the signals at the transmitter (Tx) are linearly combined in order to emulate the desired MIMO channel. This operation can be easily performed at the Tx baseband (BB) processor. The DUT(s) can be at the Tx and/or at the receiver (Rx). The DUT can be also a complete Rx able to estimate the channel. The proposed method is also well suited to test MIMO-specific algorithms (space-time coding, spatial multiplexing, etc.), that are usually implemented in the BB processors. The proposed method emulates baseband equivalent channel response, so, unlike reverberation chambers, it cannot emulate separately the effects of the multipath propagation scenario, antennas, or other embedded elements.

We consider two types of channel emulation: deterministic and stochastic. In the first case, the goal is to emulate a given channel realization (or a given sequence of channel realizations). We show closed-form expressions for the coefficients of the linear combination as functions of the actual channel in the laboratory and of the channel to emulate. In stochastic channel emulation, the objective is just to emulate

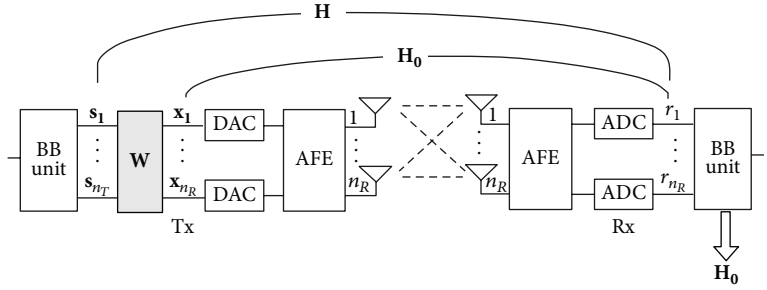

Figure 1: Proposed scheme using linear signal processing at the Tx. AFE denotes the analog front end, BB denotes baseband, and the DACs and ADCs are the digital-to-analog and the analog-to-digital converters, respectively.

a channel as a stochastic process with desired statistics (mean, spatial autocovariance, etc.), regardless of the channel realizations. The stochastic emulation is motivated by the fact that the field programmable gate arrays (FPGA) or digital signal processors (DSP) of the Tx testbeds can efficiently generate realizations of multiple independent and identically distributed (i.i.d.) random variables. Adequate linear combinations of such variables can be used to generate the coefficients for the channel emulation with desired statistics.

The proposed method has been implemented and tested over a commercial MIMO testbed in our laboratory. The experimental results show the accuracy of the method for OTA MIMO testing in any channel condition.

The rest of the paper is organized as follows. Section 2 describes the proposed scheme. From this, we derive closed-form expressions for the weights as a function of the channel to emulate and the actual channel in the laboratory. Section 3 deals with the implementation in a commercial testbed. Section 4 shows experimental results that validate the method. Finally, Section 5 is devoted to the concluding remarks.

2. MIMO Channel Emulation Scheme

Figure 1 depicts the proposed scheme for MIMO testing and channel emulation. To emulate a MIMO channel with n_T transmit and n_R receive antennas, a testbed Tx with n_R antennas is required. Let $\mathbf{H}_0 \in \mathbb{C}^{n_R \times n_R}$ be the equivalent baseband channel response between the testbed Tx and the Rx for a specific location in the laboratory, including the DUT (or the DUTs). As it was mentioned, the DUTs can be at the Tx and/or Rx. The DUT could be even a complete Rx. In any case, the BB processor at the Rx must estimate the channel, $\mathbf{H}_0$, which is assumed to be constant during the process. Let $\mathbf{s} \in \mathbb{C}^{n_T \times 1}$ be a vector comprising the equivalent baseband input signals. They are linearly combined by a weights matrix $\mathbf{W} \in \mathbb{C}^{n_R \times n_T}$ at the testbed Tx to produce the signal vector $\mathbf{x} \in \mathbb{C}^{n_R \times 1}$,

$$\mathbf{x} = \mathbf{W}\mathbf{s}. \tag{1}$$

Then, the testbed transmits $\mathbf{x}$. In the absence of noise, the receive signal vector will be

$$\mathbf{r} = \mathbf{H}_0\mathbf{x} = \mathbf{H}_0\mathbf{W}\mathbf{s}. \tag{2}$$

Therefore, the baseband equivalent channel

$$\mathbf{H} = \mathbf{H}_0\mathbf{W}. \tag{3}$$

2.1. Deterministic Channel Emulation. According to (3), the weights matrix to emulate a given channel realization, $\mathbf{H}$, will be

$$\mathbf{W} = (\mathbf{H}_0)^{-1}\mathbf{H}, \tag{4}$$

where we assume that $\mathbf{H}_0$ has been previously estimated by the BB unit at the Rx [10]. In (4), we assume that $\mathbf{H}_0$ is invertible. If this was not the case, we can change the location of the testbed in the laboratory to get a well-conditioned $\mathbf{H}_0$.

To emulate a given sequence of channel realizations (possibly time correlated), $\mathbf{H}[n]$, we will obtain the corresponding sequences of weights, $\mathbf{W}[n]$, from (4), assuming that $\mathbf{H}_0$ is time invariant. Otherwise, we should reestimate $\mathbf{H}_0$ and repeat the process whenever it changes. Note that the emulation of time-correlated channel sequences is straightforward.

In general, the emulation of a $n_R \times n_T$ MIMO channel requires a testbed Tx with n_R antennas. Therefore, to emulate a single-input-multiple-output (SIMO) channel with n_R antennas, a testbed Tx with n_R antennas is still required. But for multiple-input-single-output (MISO) channel emulation, $n_R = 1$, so we only need a single antenna testbed Tx. Obviously, this simple scheme is valid when the DUT is at the Rx or it is the complete Rx. Otherwise, if the DUT is at the radiofrequency part of the Tx, we still need a Tx with n_T branches.

2.2. Stochastic Channel Emulation. Now, the channel to emulate, $\mathbf{H}$, is a random process with a given distribution and spatial covariance. Using our scheme, the statistics of $\mathbf{H}$ can be emulated by using a random weights matrix $\mathbf{W}$ with adequate distribution and spatial covariance. In the following lines, we will derive the statistical properties of $\mathbf{W}$ as a function of the required statistics for $\mathbf{H}$, assuming that $\mathbf{H}_0$ is time invariant (deterministic) during the emulation process. We distinguish two cases regarding the mean of $\mathbf{H}$: emulation of MIMO channels with zero mean and with arbitrary mean.

2.2.1. Emulation of Channels with Zero-Mean. Let $\mathbf{H}$ be a random channel matrix with zero mean, $E[\mathbf{H}] = \mathbf{0}$, and

correlation matrix $\mathbf{R}$. From (3), $\mathbf{W}$ must be also zero-mean, and $E[\mathbf{W}] = \mathbf{0}$. The channel correlation matrix is defined as

$$\mathbf{R} = E\left[\text{vec}\,(\mathbf{H})\,\text{vec}\,(\mathbf{H})^H\right], \tag{5}$$

where vec($\mathbf{A}$) is the operator that stacks matrix $\mathbf{A}$ into a vector columnwise. From (3),

$$\text{vec}\,(\mathbf{H}) = \text{vec}\left(\mathbf{H}_0\mathbf{W}\right) = \left(\mathbf{I}_{n_T} \otimes \mathbf{H}_0\right)\text{vec}\,(\mathbf{W}), \tag{6}$$

where $\otimes$ denotes the Kronecker product. Combining (5) and (6),

$$\mathbf{R} = \left(\mathbf{I}_{n_T} \otimes \mathbf{H}_0\right)\mathbf{R}_W\left(\mathbf{I}_{n_T} \otimes \mathbf{H}_0^H\right), \tag{7}$$

where $\mathbf{R}_W = E[\text{vec}(\mathbf{W})\,\text{vec}(\mathbf{W})^H]$ is the correlation matrix of $\mathbf{W}$. Therefore, to get $\mathbf{R}$, the weights correlation matrix must be

$$\mathbf{R}_W = \left(\mathbf{I}_{n_T} \otimes \mathbf{H}_0^{-1}\right)\mathbf{R}\left(\mathbf{I}_{n_T} \otimes \left(\mathbf{H}_0^{-1}\right)^H\right). \tag{8}$$

As example, to emulate a Rayleigh channel with correlation matrix $\mathbf{R}$, we will generate realizations of the matrix $\mathbf{W}$ according to

$$\text{vec}\,(\mathbf{W}) = \mathbf{R}_W^{1/2}\,\text{vec}\left(\mathbf{W}_W\right), \tag{9}$$

where $\mathbf{R}_W$ is given by (8) and vec($\mathbf{W}_W$) is an i.i.d. complex Gaussian vector: $\text{vec}(\mathbf{W}_W) \sim \mathcal{CN}(\mathbf{0}, \mathbf{I}_{n_R n_T})$. The realizations of $\mathbf{W}_W$ can be efficiently generated, in real time, within the FPGA or DSP of the Tx.

2.2.2. Emulation of Channels with Arbitrary Mean. Let $\mathbf{H}$ be a random channel matrix with mean $E[\mathbf{H}] = \mathbf{M}$. From (3), $\mathbf{M} = \mathbf{H}_0\mathbf{M}_W$, where $\mathbf{M}_W = E[\mathbf{W}]$. Therefore, to emulate a channel with mean $\mathbf{M}$, the mean of the weights matrix must be

$$\mathbf{M}_W = \mathbf{H}_0^{-1}\mathbf{M}. \tag{10}$$

Let us write that $\mathbf{H} = \widetilde{\mathbf{H}} + \mathbf{M}$ and $\mathbf{W} = \widetilde{\mathbf{W}} + \mathbf{M}_W$, where $\widetilde{\mathbf{H}} = \mathbf{H}_0\widetilde{\mathbf{W}}$. The covariance matrix of $\mathbf{H}$, $\mathbf{C}$, is the correlation matrix of $\widetilde{\mathbf{H}}$. Similarly, the covariance matrix of $\mathbf{W}$, $\mathbf{C}_W$, is the correlation matrix of $\widetilde{\mathbf{W}}$. Then, from (7),

$$\mathbf{C} = \left(\mathbf{I}_{n_T} \otimes \mathbf{H}_0\right)\mathbf{C}_W\left(\mathbf{I}_{n_T} \otimes \mathbf{H}_0^H\right). \tag{11}$$

Therefore, to emulate a MIMO channel with covariance matrix $\mathbf{C}$, the covariance matrix of the coefficients must be

$$\mathbf{C}_W = \left(\mathbf{I}_{n_T} \otimes \mathbf{H}_0^{-1}\right)\mathbf{C}\left(\mathbf{I}_{n_T} \otimes \left(\mathbf{H}_0^{-1}\right)^H\right). \tag{12}$$

As example, to emulate a Ricean channel with mean $\mathbf{M}$ and covariance matrix $\mathbf{C}$, we will generate realizations of $\mathbf{W}$ according to

$$\text{vec}\,(\mathbf{W}) = \text{vec}\left(\mathbf{M}_W\right) + \mathbf{C}_W^{1/2}\,\text{vec}\left(\mathbf{W}_W\right), \tag{13}$$

where $\mathbf{M}_W$ and $\mathbf{C}_W$ are given by (10) and (12), respectively. As it was mentioned, realizations of $\mathbf{W}_W$ can be easily generated, in real time, within the FPGA or DSP of the testbed Tx.

2.3. Emulation of MIMO Channels Based on Dual-Polarized Antennas. The use of dual-polarized antennas at the Tx and Rx leads to a 2×2 MIMO channel. The diagonal elements of the channel matrix correspond to transmission and reception on the same polarization, while off-diagonal elements correspond to transmission and reception on orthogonal polarization. Assuming Rayleigh fading, the channel is usually modeled approximately as follows [11–13]:

$$\text{vec}\,(\mathbf{H}) = \text{vec}\,(\mathbf{X}) \odot \left(\mathbf{R}^{1/2}\,\text{vec}\left(\mathbf{H}_\omega\right)\right), \qquad \mathbf{H}_\omega \sim \mathcal{CN}(\mathbf{0}, \mathbf{I}), \tag{14}$$

where $\odot$ stands for the Hadamard product, $\mathbf{R}$ is now the so-called polarization correlation matrix (usually it is approximated in terms of the transmit and receive polarization correlation matrices: $\mathbf{R} = \mathbf{R}_t^T \otimes \mathbf{R}_r$), and $\mathbf{X}$ is the polarization leakage matrix given by

$$\mathbf{X} = \begin{bmatrix} \sqrt{1-\alpha} & \sqrt{\alpha} \\ \sqrt{\alpha} & \sqrt{1-\alpha} \end{bmatrix}, \tag{15}$$

where α is a parameter which depends on the cross polarization discrimination (XPD) of the antennas and of the cross polarization coupling (XPC) of the propagation environment, often collectively referred to as XPD.

In order to emulate a Rayleigh channel with given polarization correlation matrix, $\mathbf{R}$, and polarization leakage matrix, $\mathbf{X}$, one simply should use the weights vector $\mathbf{W}'$ given by

$$\mathbf{W}' = \mathbf{X} \odot \mathbf{W}, \tag{16}$$

where $\mathbf{W}$ is obtained from (8) and (9) as a function of $\mathbf{R}$. Now, the emulated channel will be

$$\mathbf{H} = \mathbf{H}_0\mathbf{W}' = \mathbf{X} \odot \mathbf{H}_0\mathbf{W}. \tag{17}$$

Then,

$$\text{vec}\,(\mathbf{H}) = \text{vec}\,(\mathbf{X}) \odot \left(\mathbf{I}_{n_T} \otimes \mathbf{H}_0\right)\text{vec}\,(\mathbf{W}). \tag{18}$$

Considering (9) and (7),

$$\begin{aligned} \text{vec}\,(\mathbf{H}) &= \text{vec}\,(\mathbf{X}) \odot \left(\mathbf{I}_{n_T} \otimes \mathbf{H}_0\right)\mathbf{R}_W^{1/2}\,\text{vec}\left(\mathbf{W}_W\right) \\ &= \text{vec}\,(\mathbf{X}) \odot \mathbf{R}^{1/2}\,\text{vec}\left(\mathbf{W}_W\right), \end{aligned} \tag{19}$$

which is exactly the model (14).

3. Hardware Implementation

The requirements for the hardware implementation of the proposed MIMO OTA testing method are as follows.

(i) A Tx and an Rx with adequate number of antennas (see Section 2).

(ii) A weighting block at the Tx where the baseband signals, **s**, are linearly combined according to the adequate weights, **W**.

(iii) Channel estimation capability at the Rx baseband processor.

The DUTs can be any part of the Tx and/or Rx (antennas, elements of the analog front ends (AFEs), MIMO algorithms implemented at the BB processors, etc.). The DUT can be also the complete Rx, provided that its BB processor is able to estimate the equivalent baseband channel, $\mathbf{H}_0$.

Figure 2 shows the hardware implementation scheme.

3.1. Hardware Description. Regarding hardware implementation, in the Tx, we add a new block called *weighting block* to the existing BB processor. This block is in charge of applying the weights calculated in Section 2. In general, the *weighting block* consists of $n_R n_T$ complex multipliers (each one comprising 4 real multipliers and 2 real adders) and 2 complex adders (each one comprises 2 real adders). The baseband inphase and quadrature (IQ) signal samples, **s**, are generated by the baseband (BB) processor and weights, **W**, are fed, along with the signal, to the complex multipliers. The outputs of the *weighting block*, **x**, are converted to the analog domain by n_R dual digital-to-analog converters (DAC) and then upconverted to RF signals by the analog front-end (AFE). As stated before, there does not exist additional processing or extra hardware at the receive side.

This methodology requires a preliminary estimation of the actual MIMO channel, $\mathbf{H}_0$, which is typically performed by the Rx processor at the Rx (it can be carried out as described in [10]). The weights are scaled within the range $[-1, 1]$ to ensure that in their maximum value the IQ signals are not affected by saturation that can occur at the *weighting block* or at the DACs. If a higher dynamic range is desired, there exists a control that allows varying the transmit power amplifier (PA) gain at the AFE.

As Figure 2 shows, the *weighting block* is fitted into the transmit FPGA. The DACs have 14 bits of resolution, so the output of the *weighting block* must be truncated to 14 bits. The transmit weight vector falls in the range $[-1, 1]$ with one bit for the sign and 15 bits for the decimal part.

3.2. System Operation. The whole system is able to work in two modes, each suited to different requirements. On the first mode, the system emulates a block-fading channel, that is, within a block-fading period, the desired channel, **H**, remains constant, varying from block to block according to some underlying distribution. To emulate a block-fading channel, the user should change the weights from time to time, and as a result, the time among channel realizations is determined by user decisions and the delays related to weight uploading and application. This implementation takes advantage of the fact that the maximal Doppler frequency of typical fading channels is often much smaller than the symbol rate or even the data frame size and that fading variation within channel coherence time is small.

The second operation mode considers a sample-based weight application, hence the possibility of emulating high demand variability environments. In this case, the weight realizations obtained from (4) and the transmit signals are stored in the synchronous dynamic random access memory (SDRAM) and are applied in a sample by sample manner. In a sample-based weight delivering, the sampling frequency of the transmitter determines the time resolution at which the channel realizations are applied. The limitation is that the data must be prestored in memory, which is finite.

Table 1: Average SNR of the estimates of $\mathbf{H}_0$.

	h_{11}	h_{21}	h_{12}	h_{22}
SNR (dB)	28.8073	22.3865	22.5993	21.7302

4. Validation and Test

The method described in the previous section was implemented in a 2×2 testbed (see Figure 2), operating at 5.6 GHz, using the multiantenna testbed nodes described in [1, 10]. The aim was to emulate a sequence of 200 MIMO 2×2 channel realizations, $\mathbf{H}[n]$. The first 20 samples of $\mathbf{H}[n]$ are depicted in Figure 4 with circle markers.

Firstly, the actual channel $\mathbf{H}_0$ between the Tx and Rx units of the testbed was estimated 100 times along 90 seconds using the method described in [10]. The estimates are depicted in Figure 3 showing the lack of variability of the channel in the laboratory.

Table 1 illustrates the performance of the channel estimation, where the signal-to-noise ratio (SNR) values are given by

$$\mathrm{SNR} = \frac{E\left(\left|h_{i,j}^0\right|^2\right)}{\mathrm{var}\left(h_{i,j}^0\right)}, \tag{20}$$

being $h_{i,j}^0$ the corresponding entry of $\mathbf{H}_0$, and $E()$ and var() being the sample expectation and variance, respectively. More details about the channel estimation algorithm and its performance can be found in [10].

Once $\mathbf{H}_0$ was estimated, the corresponding sequence of weight matrices, $\mathbf{W}[n]$, was calculated from (4). Each weight realization was fed to the *weighting block* and the overall channel realizations $\mathbf{H}_e[n]$ were estimated using again the method of [10]. These estimates are also depicted in Figure 4 but with square markers. The figure shows an excellent agreement between the sequence to emulate, $\mathbf{H}[n]$, and the actual emulated channels $\mathbf{H}_e[n]$. Similar agreement was observed for the rest of samples.

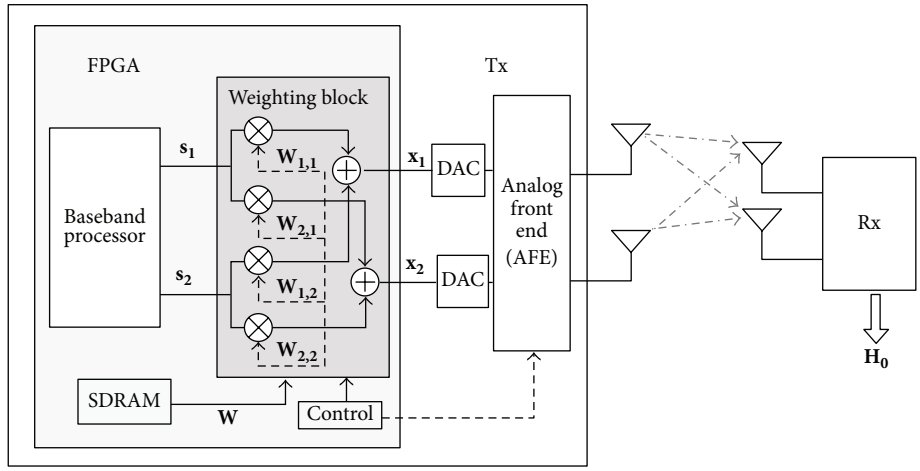

Figure 2: Scheme for 2 × 2 MIMO OTA testing and channel emulation.

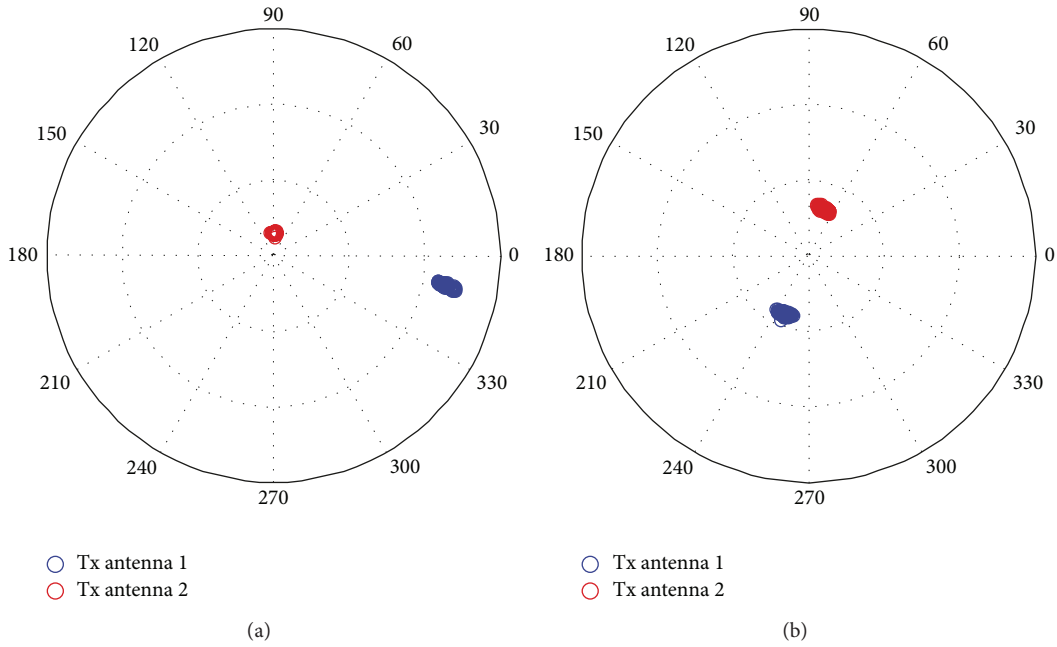

Figure 3: Estimates of $\mathbf{H}_0$. (a) Receive antenna 1. (b) Receive antenna 2.

Table 2: Performance of the emulation scheme.

	h_{11}	h_{21}	h_{12}	h_{22}
SNR (dB)	31.2819	21.9089	22.7801	18.7281

Table 2 shows the performance of the whole channel emulation procedure, where the SNR values are

$$\text{SNR} = \frac{E\left(\left|h_{i,j}\right|^2\right)}{E\left(\left|h_{i,j} - h_{i,j}^e\right|^2\right)}, \tag{21}$$

$h_{i,j}$ and $h_{i,j}^e$ being with the corresponding entries of $\mathbf{H}$ and $\mathbf{H}_e$, respectively. Comparing the values of Tables 1 and 2, one concludes that the emulation errors are mainly due to the errors in the estimation of $\mathbf{H}_0$.

5. Conclusions

This work proposes a simple and flexible method for narrowband MIMO OTA testing. It allows testing under any MIMO channel avoiding the need of channel emulators and other facilities like anechoic and reverberation chambers. The method is based on the linear combination of the baseband

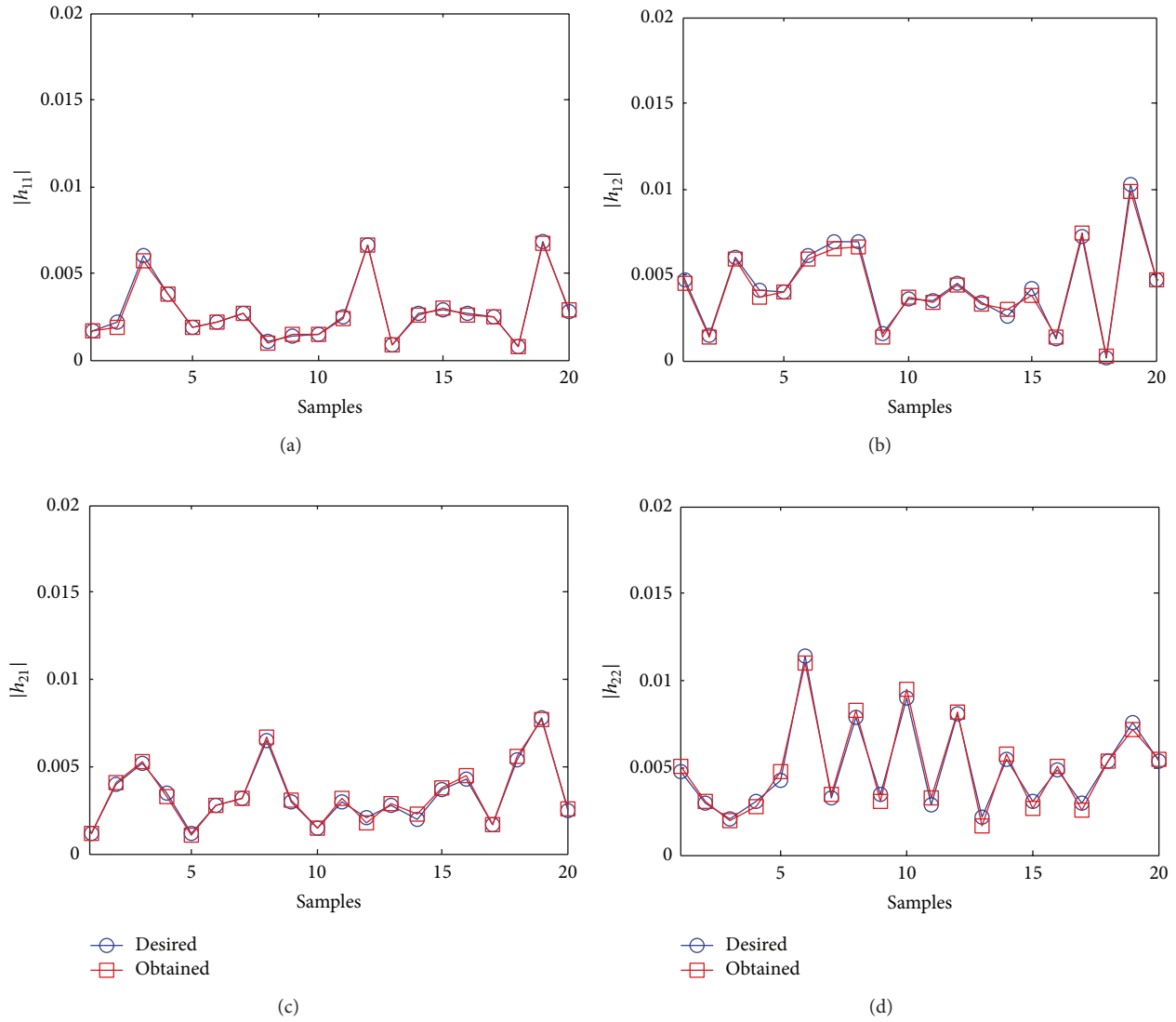

FIGURE 4: Comparison between the desired channel $\mathbf{H}[n]$ and the actual emulated channel $\mathbf{H}_e[n]$.

signals at the Tx. The solution is fully flexible in the sense that it can emulate any baseband equivalent channel realization by properly choosing the weights of the linear combination. These weights can be easily computed as functions of the channel to emulate and the actual channel between the Tx and Rx. The method relies on the stationarity of such channel in the laboratory where the testbed is placed. In a preliminary stage, this channel must be estimated by the BB processor at the Rx. In general, to emulate a $n_T \times n_R$ MIMO channel, a testbed with $n_R \times n_R$ antennas is required. The DUTs could be at the Tx and/or at the Rx. The DUT can be also a complete Rx provided that the BB processor at the Rx is able to estimate the equivalent baseband channel. The scheme is also well suited to test MIMO-specific algorithms (space-time coding, spatial multiplexing, etc.) that are usually implemented in the Tx and Rx baseband processors. To show its feasibility and performance, the proposed method was implemented on a conventional MIMO testbed with excellent results.

Acknowledgments

This work was supported by the Spanish Government, Ministerio de Ciencia e Innovacain (MICINN), under projects COSIMA (TEC2010-19545-C04-03) and COMONSENS (CSD2008-00010, CONSOLIDER-INGENIO 2010).

References

[1] L. Vielva, J. Vía, J. Gutiérrez, Ó. González, J. Ibáñez, and I. Santamaría, "Building a web platform for learning advanced digital communications using a MIMO testbed," in *Proceedings of the IEEE International Conference on Acoustics, Speech and Signal Processing (ICASSP '10)*, Dallas, Tex, USA, 2010.

[2] S. Caban, C. Mehlführer, R. Langwieser, A. L. Scholtz, and M. Rupp, "Vienna MIMO testbed," *Eurasip Journal on Applied Signal Processing*, vol. 2006, Article ID 054868, 2006.

[3] A. Guillén i Fàbregas, M. Guillaud, D. T. M. Slock et al., "A MIMO-OFDM testbed for wireless local area networks,"

Eurasip Journal on Applied Signal Processing, vol. 2006, Article ID 18083, pp. 1–20, 2006.

[4] M. Rumney, R. Pirkl, M. H. Landmann, and D. A. Sanchez-Hernandez, "MIMO over-the-air research, development, and testing," *International Journal of Antennas and Propagation*, vol. 2012, Article ID 467695, 8 pages, 2012.

[5] A. Kosako, M. Shinozawa, and Y. Karasawa, "Simplified configuration of fading emulator system for MIMO-OTA testing," in *Proceedings of the 2nd International Conference on Wireless Communication, Vehicular Technology, Information Theory and Aerospace and Electronic Systems Technology, Wireless (VITAE '11)*, pp. 1–5, March 2011.

[6] Y. Karasawa, Y. Gunawan, S. Pasisngi, K. Nakada, and A. Kosako, "Development of a MIMO-OTA system with simplified configuration," *Journal of the Korean Institute of Electromagnetic Engineering and Science*, vol. 12, no. 1, pp. 77–84, 2012.

[7] J. D. Sanchez-Heredia, J. F. Valenzuela-Valdés, A. M. Martínez-González, and D. A. Sánchez-Hernández, "Emulation of MIMO rician-fading environments with mode-stirred reverberation chambers," *IEEE Transactions on Antennas and Propagation*, vol. 59, no. 2, pp. 654–660, 2011.

[8] M. García-Fernández, J. Sánchez-Heredia, A. Martínez-González, D. Sánchez-Hernández, and J. Valenzuela-Valdés, "Advances in mode-stirred reverberation chambers for wireless communication performance evaluation," *IEEE Communications Magazine*, vol. 49, no. 7, pp. 140–147, 2011.

[9] X. Chen, P. Kildal, C. Orlenius, and J. Carlsson, "Channel sounding of loaded reverberation chamber for over-the-air testing of wireless devices: coherence bandwidth versus average mode bandwidth and delay spread," *IEEE Antennas and Wireless Propagation Letters*, vol. 8, pp. 678–681, 2009.

[10] J. Gutiérrez, Ó. González, J. Pérez et al., "Frequency-domain methodology for measuring MIMO channels using a generic testbed," *IEEE Transactions on Instrumentation and Measurement*, vol. 60, no. 3, pp. 827–838, 2011.

[11] A. Paulraj, R. Nabar, and D. Gore, *Introduction to Space-Time Wireless Communications*, Cambridge University Press, 2003.

[12] M. Coldrey, "Modeling and capacity of polarized MIMO channels," in *Proceedings of the IEEE 67th Vehicular Technology Conference (VTC '08)*, pp. 440–444, May 2008.

[13] T. Neubauer and P. C. F. Eggers, "Simultaneous characterization of polarization matrix components in pico cells," in *Proceedings of the IEEE VTS 50th Vehicular Technology Conference (VTC '99)*, pp. 1361–1365, September 1999.

Hindawi Publishing Corporation
International Journal of Antennas and Propagation
Volume 2013, Article ID 593247, 10 pages
http://dx.doi.org/10.1155/2013/593247

Research Article

An Application of Artificial Intelligence for the Joint Estimation of Amplitude and Two-Dimensional Direction of Arrival of Far Field Sources Using 2-L-Shape Array

Fawad Zaman,[1] Ijaz Mansoor Qureshi,[1] Junaid Ali Khan,[2] and Zafar Ullah Khan[1]

[1] *Department of Electronic Engineering, Faculty of Engineering and Technology, International Islamic University Sector H-10, Islamabad 44000, Pakistan*
[2] *Department of Electrical Engineering, COMSATS Institute of Information Technology, Attock 43600, Pakistan*

Correspondence should be addressed to Fawad Zaman; fawad.phdee31@iiu.edu.pk

Received 6 March 2013; Accepted 8 May 2013

Academic Editor: Juan Valenzuela-Valdes

An easy and efficient approach, based on artificial intelligence technique, is proposed to jointly estimate the amplitude, elevation, and azimuth angles of far field sources impinging on 2-L-shape array. In these proposed artificial intelligence techniques, the metaheuristics based on genetic algorithm and simulated annealing are used as global optimizers assisted with rapid local version of pattern search for optimization of the adaptive parameters. The performance metric is employed on a fitness evaluation function depending on mean square error which is optimum and requires single snapshot to converge. The proposed approaches are easy to understand, and simple to implement; the genetic algorithm specifically hybridized with pattern search generates fairly good results. The comparison of the given schemes is carried out with 1-L-shape array, as well as, with parallel-shape array and is found to be in good agreement in terms of accuracy, convergence rate, computational complexity, and mean square error. The effectiveness and efficiency of the given schemes are examined through Monte Carlo simulations and their inclusive statistical analysis.

1. Introduction

Two-dimensional direction of arrival (2D DOA) estimation for multiple signals received at sensors array is one of the indispensable steps for adaptive beamformer to maneuver the main beam in any preferred direction, while allocating nulls in the direction of unwanted signals [1, 2]. From this perspective, 2D DOA estimation has direct applications in radar, sonar, and mobile communications [3]. The most common problem in 2D DOA estimation includes pair matching between elevation and azimuth angles, estimation failure and computational complexity. In the literature, many algorithms have already been discussed in the last two decades to estimate 2-D DOA [4–7], but they have the aforementioned problems. In [8], Wu et al. proposed an algorithm based on propagator method (PM) to overcome the computational load of [7], but it fails to avoid the pair matching problem and estimation failure problem in the range of 1.2217 (radians) to 1.5708 (radians). Moreover, the parallel-shape array is used in [8] which not only needs more sensors but also requires a large number of snapshots to achieve the goal (at least 200 snapshots per sensor are required). Besides that, [8] also failed to estimate the sources amplitudes which also an important parameter to be estimated.

In order to overcome these problems, we thank evolutionary computing techniques (ECTs) and L-shape arrays (1-L and 2-L shape). It is well acknowledged in the literature that ECTs such as genetic algorithm (GA), ant colony optimization (ACO), differential evolution (DE), and particle swarm optimization (PSO) have achieved great success in solving different optimization problems especially in the field of array signal processing [9, 10]. These techniques have got attention among the researchers due to their ease in understanding, simplicity in implementation, and less probability to get stuck in the local minima. One of the other most significant aspects of ECT is that their accuracy and reliability increase more when hybridized with any other capable algorithm such as pattern search (PS), interior point algorithm (IPA), and active

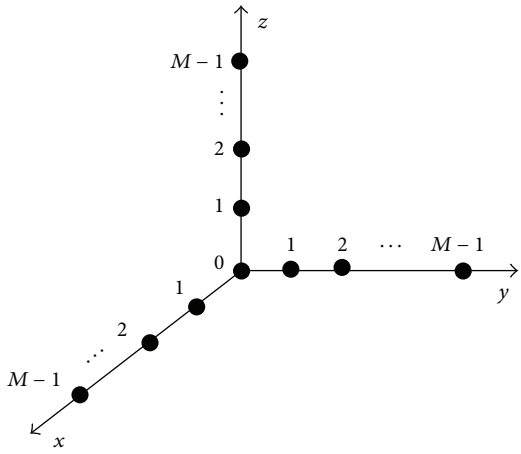

Figure 1: 2-L shape array consists of three subarrays.

set algorithm (ASA) [11–15]. In [13], GA is hybridized with IPA for 3D source localization of near field sources impinging on uniform linear array (ULA), and the hybrid GA-IPA approach has shown better performance as compared to GA and IPA alone. In [14], PSO is mixed with PS to estimate the DOA of far field sources, and again the hybrid PSO-PS technique produced better results as compared to PSO [9] and PS alone. GA is hybridized with PS to jointly estimate 3D parameters (amplitude, elevation angle, and azimuth angle) of far field sources arriving at 1-L shape array and again the results of hybrid GA-PS technique were remarkable as compared to GA and PS alone [15]. In [13–15], every time GA and PSO are treated as global optimizers, while PS and IPA are used as local search optimizers and mean square error (MSE) is used as a fitness function.

In this paper, an easy and efficient approach based on hybridized GA with PS (GA-PS) and hybrid simulated annealing (SA) technique with PS (SA-PS) are developed for joint estimation of amplitudes and 2-D DOA of far field sources impinging on 2-L-shape array. In these approaches GA and SA are exploited as global optimizers, while PS is incorporated for rapid local search to improve the results further. Mean square error (MSE) is used as an objective function based on an error between actual and estimated signals which is basically derived from maximum likelihood principle [13]. This fitness function needs single snapshot to achieve the results and avoids any uncertainty among the angles that are supplement to one another. The validity and effectiveness of the proposed approaches are tested on a large number of simulations which include different cases based on a different number of sources, a different number of sensors, computational complexity, and the proximity of the sources. Initially, the results of GA, PS, SA, SA-PS, and GA-PS are compared with each other for 2-L-shape array, and then, the entire results are compared with the results of 1-L-shape array [15]. Later on, the results are also compared with parallel shape array which uses PM [8].

Throughout the paper, the matrices are denoted by capital bold letters, while vectors are expressed by small bold letters, whereas "T" denotes the transpose of vectors or matrices.

The left behind paper is organized as follows: the problem formulation is discussed in Section 2, whereas its proposed methodology is provided in Section 3. Section 4 demonstrates the comprehensive simulations along with the discussion of the results, while conclusion and future directions for the research are revealed in Section 5.

2. Problem Formulation

In this section, we addressed the unknown parameters of the received signals. Consider a 2-L-shape array which consists of three uniform linear arrays (ULAs) placed along x-axis, y-axis, and z-axis. Each ULA contains $M-1$ elements with the same interelement spacing "d", while the reference sensor is common for all subarrays as shown in Figure 1 [16]. Consider K narrow band sources impinging on the 2-L-shape array where s_i, θ_i, and ϕ_i are the ith source amplitude, elevation angle, and azimuth angle, respectively.

Output Vector along z-Axis Subarray. The subarray along z-axis is used to estimate the elevation angle. The signal received at lth element from K sources can be written as

$$w_{zl} = \sum_{i=1}^{K} b_{zl}(\theta_i)\, s_i + \alpha_{zl}, \tag{1}$$

where $l = 0, 1, 2, \ldots, M-1$.

In matrix-vector form, the output of entire subarray can be written as

$$\mathbf{w}_z = \mathbf{B}_z(\theta)\, \mathbf{s} + \boldsymbol{\alpha}_z, \tag{2}$$

where $\mathbf{B}$ is called steering matrix, which contains steering vectors; that is,

$$\mathbf{B}_z = \left[\mathbf{b}_{z0}, \mathbf{b}_{z1}, \ldots, \mathbf{b}_{zM-1}\right]^T, \tag{3}$$

where

$$\mathbf{b}_{zl} = \left[b_{zl}(\theta_1), b_{zl}(\theta_2), \ldots, b_{zl}(\theta_k)\right],$$

$$b_{zl}(\theta_i) = \exp\left(-j\psi_{l,i}\right), \qquad \psi_{l,i} = \frac{2\pi l d \cos\theta_i}{\lambda} \qquad \text{for } i = 1, 2, \ldots, K. \tag{4}$$

Similarly, in (2),

$$\mathbf{w}_z = \left[w_{z0}, w_{z1}, \ldots, w_{zM-1}\right]^T,$$

$$\mathbf{s} = \left[s_1, s_2, \ldots, s_K\right]^T, \tag{5}$$

$$\boldsymbol{\alpha}_z = \left[\alpha_{z0}, \alpha_{z1}, \ldots, \alpha_{zM-1}\right]^T,$$

where $\boldsymbol{\alpha}_z$ is called additive white Gaussian noise (AWGN) added at the output of each sensor placed in z-axis subarray.

Output Vector along x-Axis Subarray. The subarray along x-axis is used to estimate the x-component of azimuth angle and elevation angle. The output at lth sensor placed in the x-axis subarray for K sources can be written as

$$w_{xl} = \sum_{i=1}^{K} b_{xl}(\theta_i, \phi_i)\, s_i + \alpha_{xl}. \tag{6}$$

Table 1: Parameter settings for GA, SA, and PS.

GA		PS		SA	
Parameters	Settings	Parameters	Setting	Parameters	Setting
Population size	240	Poll method	GPS positive basis 2 N	Annealing function	Fast
No. of generations	1000	Polling order	Consecutive	Reannealing interval	100
Migration direction	Both ways	Maximum iteration	800	Temperature update function	Exponential temperature update
Crossover fraction	0.2	Function evaluation	16000	Initial temperature	100
Crossover	Heuristic	Mesh size	01	Data type	Custom
Function tolerance	10–12	Expansion factor	2.0	Function tolerance	10–12
Initial range	[0-1]	Contraction factor	0.5	Max iteration	2000
Scaling function	Rank	Penalty factor	100	Max function evaluations	3000 ∗ number of variables
Selection	Stochastic uniform	Bind tolerance	10–03	Temperature update function	Exponential temperature update
Elite count	2	Mesh tolerance	10–06		
Mutation function	Adaptive feasible	X tolerance	10–06	Hybrid function call interval	End

In vector-matrix form, it can be written as

$$\mathbf{w}_x = \mathbf{B}_x(\theta,\phi)\,\mathbf{s} + \boldsymbol{\alpha}_x, \tag{7}$$

where

$$\begin{aligned} \mathbf{B}_x &= \left[\mathbf{b}_{x0}, \mathbf{b}_{x1}, \ldots, \mathbf{b}_{xM-1}\right]^T, \\ \mathbf{b}_{xl} &= \left[b_{xl}(\theta_1,\phi_1), b_{xl}(\theta_2,\phi_2), \ldots, b_{xl}(\theta_k,\phi_k)\right], \\ b_{xl}(\theta_i,\phi_i) &= \exp\left(-j\psi_{l,i}\right), \qquad \psi_{l,i} = \frac{2\pi l d \sin\theta_i \cos\phi_i}{\lambda}. \end{aligned} \tag{8}$$

Similarly,

$$\begin{aligned} \mathbf{w}_x &= \left[w_{x0}, w_{x1}, \ldots, w_{xM-1}\right]^T, \\ \boldsymbol{\alpha}_x &= \left[\alpha_{x0}, \alpha_{x1}, \ldots, \alpha_{xM-1}\right]^T, \end{aligned} \tag{9}$$

where $\boldsymbol{\alpha}_x$ is AWGN added at the output of each sensor in x-axis subarray.

Output Vector along y-Axis Subarray. In the same manner, the y-axis subarray is used to estimate the y-component of elevation and azimuth angle. The output at lth sensor in this subarray is given as follows:

$$\begin{aligned} w_{yl} &= \sum_{i=1}^{K} b_{yl}(\theta_i,\phi_i)\, s_i + \alpha_{yl}, \\ \mathbf{w}_y &= \mathbf{B}_y(\theta,\phi)\,\mathbf{s} + \boldsymbol{\alpha}_y, \end{aligned} \tag{10}$$

where

$$\mathbf{B}_y = \left[\mathbf{b}_{y0}, \mathbf{b}_{y1}, \ldots, \mathbf{b}_{yM-1}\right]^T, \tag{11}$$

where

$$\begin{aligned} \mathbf{b}_{yl} &= \left[b_{yl}(\theta_1,\phi_1), b_{yl}(\theta_2,\phi_2), \ldots, b_{yl}(\theta_k,\phi_k)\right], \\ b_{yl}(\theta_i,\phi_i) &= \exp\left(-j\psi_{l,i}\right), \qquad \psi_{l,i} = \frac{2\pi l d \sin\theta_i \sin\phi_i}{\lambda}. \end{aligned} \tag{12}$$

Similarly,

$$\begin{aligned} \mathbf{w}_y &= \left[w_{y0}, w_{y1}, \ldots, w_{yM-1}\right]^T, \\ \boldsymbol{\alpha}_y &= \left[\alpha_{y0}, \alpha_{y1}, \ldots, \alpha_{yM-1}\right]^T, \end{aligned} \tag{13}$$

where $\boldsymbol{\alpha}_y$ is AWGN added at the output of each sensor in y-axis subarray. Here, the problem in hand is very clear which is to estimate the unknown parameters, that is, amplitudes and 2D-DOA (elevation, azimuth) angles for K sources impinging from far field on 2-L-shape array.

3. Proposed Techniques

In this section, a brief introduction, parameter setting, and flow diagram are given for GA, PS, SA, GA-PS, and SA-PS.

Simulated Annealing. Simulated annealing (SA) technique is used for both discrete and continuous optimization problems. SA works on those problems, which have controlled heating and cooling properties as evident from its name "annealing", which means "To heat and then cool." Due to easiness in implementation and the capability to avoid getting stuck in local minima, SA is a well-liked technique over the last few decades and has been successfully used in wide range of engineering problems [17]. In this paper, an MATLAB "built-in optimization tool box" is used for which the parameter setting is shown in Table 1. The best individual result of SA is further passed through PS for further tuning.

Pattern Search. Pattern search (PS) was introduced by Hookes and Jeeves in 1961 which does not require the gradient or derivative of the problem and can be used for both local and global optimization problems. Basically, PS works on mesh which is defined according to some specific rules. If no improvement in cost function is achieved at the mesh points of current iteration, then the mesh is polished and the process

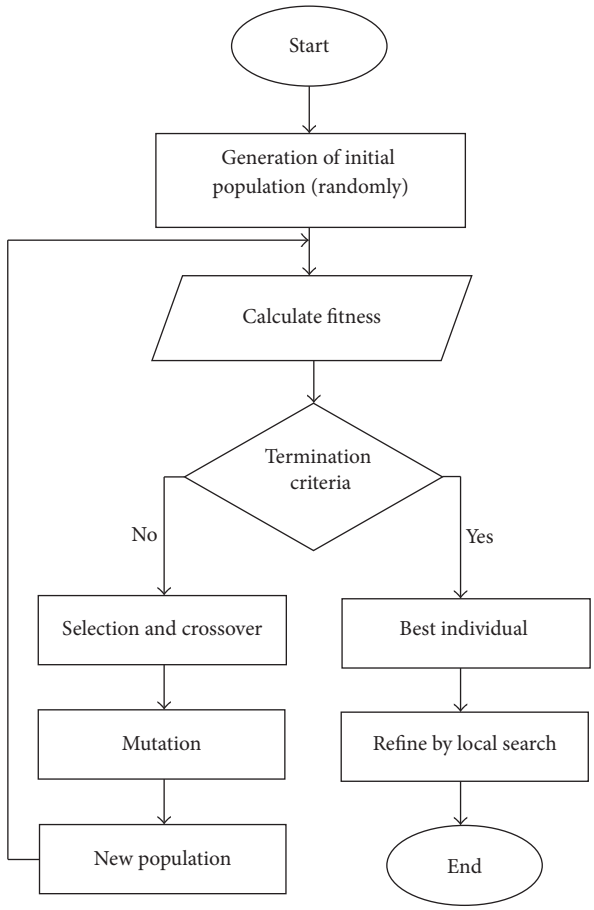

Figure 2: Generic structure of the hybrid intelligent approach.

is repeated. It has already got application almost in every field such as signal processing and soft computing [18].

Genetic Algorithm. GA is basically different from previously discussed algorithm (SA and PS) and is applicable to a wide range of optimization problems. GA is a more prominent and proficient algorithm than any other evolutionary computing technique due to its ease in conception, ease in implementation, and more importantly less probability to get stuck in the presence of local optima. GA is being successfully applied to a wide range of problems having application in commerce to the leading scientific research [19, 20]. The structure of GA exploited for the joint estimation is given in Figure 2.

The general settings consisting of population size, number of generations of the algorithm, function evaluations, and stoppage criteria are defined in Table 1, along with some specific parameter setting/values of the three algorithms based on GA, PS, and SA.

The logical steps for GA and GA-PS in the form of pseudo code are given in the following steps.

Step 1 (initialization). Generate randomly Q number of chromosomes (particles) where the length of each chromosome is $3\times K$. In each chromosome, the first K genes represent amplitudes, the next K genes contain the elevation angles, while the last K genes represent the azimuth angles. Mathematically, the qth chromosome can be written as

$$\mathbf{d}_q = \left[s_{q,1}, s_{q,2}, \ldots, s_{q,K}, \theta_{q,K+1}, \ldots, \theta_{q,2K}, \phi_{q,2K+1}, \ldots, \phi_{q,3K}\right]. \tag{14}$$

Here, $s_{qj} \in R : L_a \le s_{qj} \le U_a$ where L_a and U_a are the lower and upper bounds of signal amplitudes $\forall q = 1, 2, \ldots, Q$ and $j = 1, 2, \ldots, K$. In the same way, the elevation and azimuth angles are

$$\begin{aligned} &\theta_{qj} \in R : 0 \le \theta_{qj} \le \pi, \\ \forall q = 1, 2, \ldots, Q, \quad &j = K+1, K+2, \ldots, 2K, \\ &\phi_{qj} \in R : 0 \le \phi_{qj} \le 2\pi, \\ \forall q = 1, 2, \ldots, Q, \quad &j = 2K+1, 2K+2, \ldots, 3K. \end{aligned} \tag{15}$$

Step 2 (objective function). MSE is used as an objective evaluation function, which is derived from MLP [13]. For qth chromosome, it can be written as

$$E(q) = E_x(q) + E_y(q) + E_z(q), \tag{16}$$

where

$$\begin{aligned} E_x(q) &= \frac{1}{(M-1)} \sum_{x=1}^{M-1} \left|w_x - \widehat{w}_x^q\right|^2, \\ E_y(q) &= \frac{1}{(M-1)} \sum_{y=1}^{M-1} \left|w_y - \widehat{w}_y^q\right|^2, \\ E_z(q) &= \frac{1}{(M-1)} \sum_{z=1}^{M-1} \left|w_z - \widehat{w}_z^q\right|^2. \end{aligned} \tag{17}$$

w_z, w_x, and w_y are defined in (1), (3), and (7), respectively, while $\widehat{w}_x^q$, $\widehat{w}_y^q$, and $\widehat{w}_z^q$ at lth element of each subarray for qth chromosome are given as

$$\begin{aligned} \widehat{w}_{xl}^q &= \sum_{i=1}^{K} \exp\left[-j\pi l \sin\left(d_{q,K+i}\right) \cos\left(d_{q,2K+i}\right)\right] d_{q,i}, \\ \widehat{w}_{yl}^q &= \sum_{i=1}^{K} \exp\left[-j\pi l \sin\left(d_{q,K+i}\right) \sin\left(d_{q,2K+i}\right)\right] d_{q,i}, \\ \widehat{w}_{zl}^q &= \sum_{i=1}^{K} \exp\left[-j\pi l \cos\left(d_{q,K+i}\right)\right] d_{q,i}, \end{aligned} \tag{18}$$

where d_q is defined in (14).

Step 3 (termination criteria). The termination criteria depending on the following conditions are achieved.

(a) If the objective function value is achieved, which is predefined, that is, $\varepsilon \le 10^{-12}$.

(b) The total number of iterations is completed.

(c) The Tol Fun exceeded.

(d) Tol Con occurred.

Table 2: Estimation accuracy of 2-L-shape array for 2 sources.

Scheme	s_1	s_2	θ_1 (rad)	θ_2 (rad)	ϕ_1 (rad)	ϕ_2 (rad)
Desired values	1.0000	2.0000	0.5236	0.8727	1.2217	1.9199
GA	1.0003	2.0003	0.5240	0.8731	1.2221	1.9203
PS	1.0020	2.0021	0.5259	0.8748	1.2239	1.9220
SA	1.0977	2.0178	0.5385	0.8889	1.2361	1.9284
SA-PS	1.0047	2.0047	0.5278	0.8770	1.2260	1.9242
GA-PS	1.0000	2.0000	0.5235	0.8726	1.2216	1.9198

Table 3: Estimation accuracy of 1-L-type array for 2 sources [15].

Scheme	s_1	s_2	θ_1 (rad)	θ_2 (rad)	ϕ_1 (rad)	ϕ_2 (rad)
Desired values	1.0000	2.0000	0.5236	0.8727	1.2217	1.9199
GA	1.0008	2.0008	0.5243	0.8735	1.2225	1.9207
PS	1.0032	2.0033	0.5268	0.8759	1.2249	1.9231
SA	1.0196	2.0195	0.5432	0.8923	1.2413	1.9395
SA-PS	1.0063	2.0063	0.5299	0.8790	1.2281	1.9263
GA-PS	1.0003	2.0002	0.5233	0.8723	1.2220	1.9195

Step 4 (reproduction). New population is generated by using the operators of crossover, elitism, and mutation selection as provided in Table 1.

Step 5 (hybridization). In this step, the finest results got through GA are further given to PS for more improvement. The setting used for PS is also provided in Table 1.

Step 6 (storage). Store global best of the current iteration which will be used for comparison and better statistical analysis, and repeat Steps 2 to 5 for enough numbers of independent runs.

4. Results and Discussions

This section is broadly divided into two parts. In first part of simulations, GA, PS, SA, GA-PS, and SA-PS are examined for 2-L-shape array in terms of estimation accuracy, convergence rate, and at the same time, the results are compared with 1-L-shape array [15]. In the second part, the performance of the best scheme among the above-mentioned five schemes for 2-L-shape array is not only compared with 1-L-shape array but also with parallel-shape array [8]. Throughout the simulations, the distance "d" between two consecutive sensors in each subarray is kept $\lambda/2$. All the values of the DOA (elevation and azimuth angle) of sources are taken in radian (rad), and all the results for 2-L-shape array are carried out for threshold value of MSE 10^{-2}. The MATLAB built-in "Optimization Tool Box" is used for GA, SA, and PS for which the settings are provided in Table 1. As in [15], no noise is added to the system for estimation accuracy and convergence rate. All the results are comprehensively examined for 100 independent runs.

Case 1. In this case, the estimation accuracy of GA, PS, SA, GA-PS, and SA-PS is discussed for two sources impinging on 2-L-type array. For better comparison and analysis, all the values of amplitudes and DOA are the same as in [15] for 1-L-shape array, so the amplitudes and DOA values are $\{s_1, s_2, \theta_1, \theta_2, \phi_1, \phi_2\} = \{1, 2, 0.5236\,(\text{rad}), 0.8727\,(\text{rad}), 1.2217\,(\text{rad}), 1.9199\,(\text{rad})\}$ where s_1, θ_1, and ϕ_1 represent the amplitudes, elevation angle, and azimuth angles of first source and so on. The 2-L-shape array is composed of 4 sensors in which 1 sensor is placed along each subarray, while the reference sensor is common for them. As provided in Table 2, all the five mentioned techniques are quite capable of producing fairly good estimate of the actual values. However, among them, the hybrid approach GA-PS produced better results as compared to the other techniques used. The second and third best results are provided by GA and PS, respectively. The results of SA are also improved when hybridized with PS.

The results of 1-L-shape array for 2 sources are provided in Table 3 which requires 7 sensors [15]. The 1-L-shape array in [15] also uses the same techniques. One can clearly deduce from the comparison of Tables 2 and 3 that 2-L-shape array produced more accurate results as compared to 1-L-shape array with less number of sensors.

Case 2. In this case, the estimation accuracy of all the above-mentioned five techniques is discussed for three sources impinging on 2-L-shape array. This time the 2-L-shape array consists of 7 sensors; that is, 2 sensors are placed along each subarray, while the reference sensor is common for them. For better comparison with 1-L-type array, the same values of amplitudes and DOA are used as in [15], which are provided in Table 4. In this case, few local minima are observed due to which the performance of all five techniques especially SA, SA-PS, and PS is despoiled. However, again the hybrid GA-PS shows excellence in accuracy even in the presence of local minima. The second best result is shown by GA alone.

Now compare the results with 1-L-type array as provided in Table 5 which requires thirteen sensors [15]. Now, one can observe that 2-L-shape array not only requires less number of

Table 4: Estimation accuracy of 2-L-type array for 3 sources.

Scheme	s_1	s_2	s_3	θ_1 (rad)	θ_2 (rad)	θ_3 (rad)	ϕ_1 (rad)	ϕ_2 (rad)	ϕ_3 (rad)
Desired values	1.0000	2.0000	3.0000	0.1745	0.8727	1.3090	0.5236	1.9199	2.4435
GA	1.0043	2.0043	3.0042	0.1788	0.8769	1.3132	0.5278	1.9243	2.4478
PS	1.0189	2.0190	3.0189	0.1934	0.9005	0.8917	0.5427	1.9389	2.4624
SA	1.0509	2.0508	3.0509	0.2254	0.9237	1.3598	0.5744	1.9708	2.4944
SA-PS	1.0342	2.0342	3.0343	0.2087	0.9069	1.3432	0.5581	1.9541	2.4778
GA-PS	1.0003	2.0004	3.0003	0.1748	0.8730	1.3094	0.5240	1.9202	2.4439

Table 5: Performance of 1-L-type array for 3 sources [15].

Scheme	s_1	s_2	s_3	θ_1 (rad)	θ_2 (rad)	θ_3 (rad)	ϕ_1 (rad)	ϕ_2 (rad)	ϕ_3 (rad)
Desired values	1.0000	2.0000	3.0000	0.1745	0.8727	1.3090	0.5236	1.9199	2.4435
GA	1.0073	2.0073	3.0073	0.1818	0.8800	1.3163	0.5309	1.9272	2.4508
PS	1.0278	2.0277	3.0277	0.2023	0.9005	1.3368	0.5514	1.9477	2.4713
SA	1.0610	2.0611	3.0610	0.2355	0.9337	1.3700	0.5846	1.9809	2.5045
SA-PS	1.0432	2.0432	3.0432	0.2177	0.9159	1.3522	0.5668	1.9631	2.4867
GA-PS	1.0011	2.0011	3.0011	0.1756	0.8738	1.3101	0.5247	1.9210	2.4446

sensors but also produces more accurate results as compared to 1-L-shape array.

Case 3. In this case, the estimation accuracy is examined for 4-sources. The 2-L-shape array consists of 10 sensors; that is, 3 elements are placed along each subarray, while the reference element is common for them. As provided in Table 6, again the hybrid GA-PS leads the edge over the remaining four techniques in terms of estimation accuracy. The results for 1-L-shape array for the same schemes and the same number of sources are provided in Table 7 which needs fifteen sensors [15]. One can again make out the advantages of 2-L-shape array over 1-L-type array in terms of accuracy and the number of sensors required.

Case 4. In this case, the convergence rate is evaluated for 2-L-shape array against a different number of sources in the presence of 10 dB noise. As shown in Figure 3, the convergence rates of all schemes are degraded with the increase of sources. However, one can notice that the convergence rate of GA is remarkable in case of hybridization with PS. The second best convergence is produced by GA itself alone.

Now, by comparing with 1-L-shape array whose convergence rate is shown in Figure 4, one can conclude that all the five schemes have better convergence rate for 2-L-shape array as compared to 1-L-shape array.

Case 5. In this case, we checked the validation of all techniques for more practical scenario; that is, we considered DOA on the reference axis of L-shape arrays. For this, the 2-L-shape array is composed of 12 sensors where the amplitudes and DOA of the four sources are

$$\{s_1 = 2, \theta_1 = 1.5702\,(\text{rad}), \phi_1 = 0\,(\text{rad})\},$$
$$\{s_2 = 5, \theta_2 = 1.2217\,(\text{rad}), \phi_2 = 6.2832\,(\text{rad})\},$$

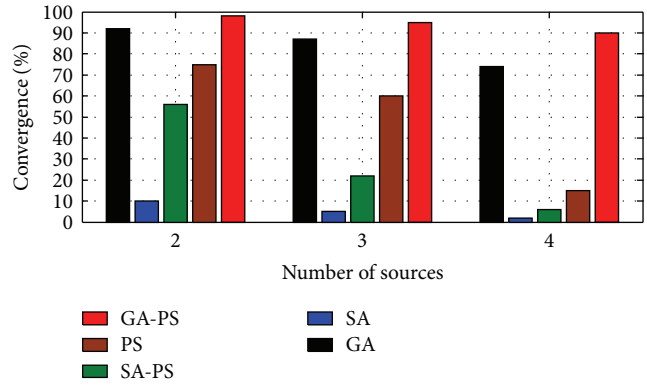

Figure 3: Convergence rate versus number of sources for 2-L-shape array at 10 dB noise.

$$\{s_3 = 1, \theta_3 = 0\,(\text{rad}), \phi_3 = 4.7124\,(\text{rad})\},$$
$$\{s_4 = 4, \theta_4 = 1.0472\,(\text{rad}), \phi_4 = 1.5702\,(\text{rad})\}. \quad (19)$$

As provided in Table 8, an obvious degradation can be observed in the estimation accuracy of each scheme for all the elevation angles taken near the reference axis, while for azimuth angle near the reference axis, the accuracy is slightly degraded. However, among all of them the GA-PS technique is less degraded as compared to the others.

Now, if we check the same DOA using 1-L-shape array, then one can see in Table 9 that the estimation accuracy of all schemes is degraded more as compared to 2-L-shape array.

Up till now, the performance of GA, PS, SA, SA-PS, and GA-PS is discussed for both 1-L- and 2-L-type arrays, and it has been shown through various cases that GA-PS produced fairly good results for both arrays. So, from now onwards, our focus will be limited to the GA-PS technique only. In the upcoming second part of the simulations, we will compare

Table 6: Performance of 2-L-type array for 4 sources.

Scheme	s_1	s_2	s_3	s_4	θ_1 (rad)	θ_2 (rad)	θ_3 (rad)	θ_4 (rad)	ϕ_1 (rad)	ϕ_2 (rad)	ϕ_3 (rad)	ϕ_4 (rad)
Desired	1.0000	2.0000	3.0000	4.0000	0.2618	0.6109	1.0472	1.4835	1.6581	2.1817	2.7925	3.4034
GA	1.0102	2.0103	3.0103	4.0102	0.2721	0.6212	1.0576	1.4937	1.6683	2.1920	2.8028	3.4137
PS	1.0313	2.0312	3.0313	4.0314	0.2932	0.6423	1.0787	1.5148	1.6895	2.2132	2.8239	3.4348
GA-PS	1.0040	2.0042	3.0043	4.0040	0.2659	0.6151	1.0514	1.4877	1.6624	2.1858	2.7966	3.4077
SA	1.1011	2.1010	3.1012	4.1010	0.3628	0.7122	1.1483	1.5846	1.7594	2.2829	2.8937	3.5044
SA-PS	1.0787	2.0786	3.0785	4.0787	0.3405	0.6895	1.1260	1.5624	1.7369	2.2606	2.8713	3.4821

Table 7: Performance of 1-L-type array for 4 sources [15].

Scheme	s_1	s_2	s_3	s_4	θ_1 (rad)	θ_2 (rad)	θ_3 (rad)	θ_4 (rad)	ϕ_1 (rad)	ϕ_2 (rad)	ϕ_3 (rad)	ϕ_4 (rad)
Desired	1.0000	2.0000	3.0000	4.0000	0.2618	0.6109	1.0472	1.4835	1.6581	2.1817	2.7925	3.4034
GA	1.0163	2.0163	3.0162	4.0163	0.2781	0.6272	1.0635	1.4998	1.6744	2.1980	2.8088	3.4197
PS	1.0425	2.0425	3.0426	4.0426	0.3043	0.6534	1.0897	1.5260	1.7006	2.2242	2.8350	3.4468
GA-PS	1.0083	2.0083	3.0083	4.0083	0.2701	0.6192	1.0555	1.4918	1.6664	2.1900	2.8008	3.4117
SA	1.1263	2.1263	3.1263	4.1164	0.3881	0.7372	1.1735	1.6098	1.7844	2.3080	2.9188	3.5306
SA-PS	1.0932	2.0932	3.0932	4.0932	0.3550	0.7041	1.1404	1.5767	1.7513	2.2749	2.8857	3.4966

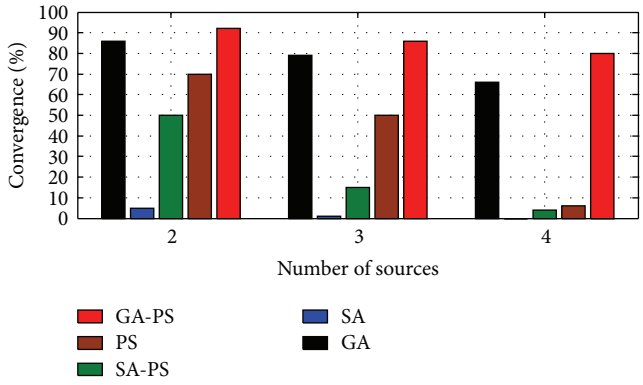

Figure 4: Convergence rate versus number of sources for 1-L-shape array at 10 dB noise.

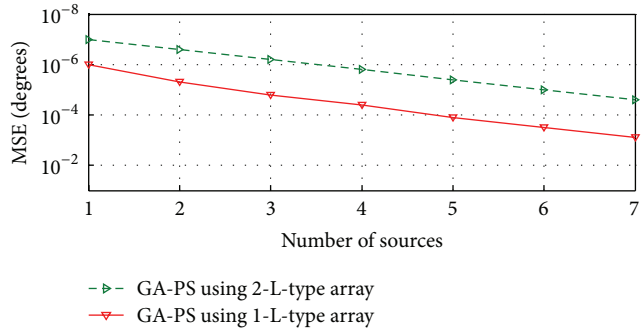

Figure 5: MSE versus number of sources at 10 dB noise.

the GA-PS technique used for 2-L-shape array not only with GA-PS technique used for 1-L-shape array but also with PM which utilizes parallel-shape array [8].

Case 6. In this case, the estimation accuracy in terms of MSE is discussed for GA-PS technique against the increasing number of sources. For this, the 2-L-shape array is composed of 13 sensors, while the 1-L-shape array is consisting of 19 sensors. As shown in Figure 5, the MSE is degraded for both L-shape arrays against the increasing number of sources. However, the MSE of GA-PS for 2-L-shape array is better than 1-L-shape array.

Case 7. In this case, Tables 10, 11, and 12 list the variances, means, and standard deviations for parallel-shape array with PM method and L-shape arrays with hybrid GA-PS approach. For this, the elevation angle varies between 1.2217 (rad) and 1.5708 (rad) for a fixed azimuth angle of 0.6109 (rad) in the presence of 10 dB noise.

The performance of PM method with parallel-shape array is worse for this range of elevation angle, while the 2-L-shape array with GA-PS technique produced accurate estimation. The second best result is produced by GA-PS for 1-L-shape array. This range of elevation angles is very important for mobile communication, and hence, 2-L-shape array with GA-PS is a good choice to be used. Moreover, the range of elevation and azimuth angles for 2-L-shape array is $(0, \pi)$ and $(0, 2\pi)$, respectively, while the parallel-shape array and 1-L-shape array have the range of elevation, and azimuth angles are $(0, \pi/2)$ and $(0, 2\pi)$, respectively, so both arrays cannot be operated for elevation angles beyond $\pi/2$. For more details, the readers are encouraged to see [21].

Case 8. In this case, we discussed the computational complexity of GA-PS used for L-shape arrays and PM with parallel-shape array. The PM required total $O(3 \times M \times T \times K)$ computations where M is the total number of sensors, K is the total number of sources, and T is the number of snapshots which is 200 [8]. On the other hand, the major computations involved in GA-PS with 2-L-shape array include the total number of multiplication in fitness function $O(Q^2(3 +$

Table 8: Performance of 2-L-type array for sources located on reference axis.

Scheme	s_1	s_2	s_3	s_4	θ_1 (rad)	θ_2 (rad)	θ_3 (rad)	θ_4 (rad)	ϕ_1 (rad)	ϕ_2 (rad)	ϕ_3 (rad)	ϕ_4 (rad)
Desired	2.0000	5.0000	1.0000	4.0000	1.5702	1.2217	0.0000	1.0472	0.0000	6.2832	4.7124	1.5702
GA	1.9897	5.0105	0.9897	4.0103	1.6633	1.2321	0.0838	1.0573	0.0192	6.3041	4.6914	1.5900
PS	2.0315	4.9688	0.9687	3.9687	1.7139	1.2485	0.1623	1.0785	0.0314	6.2500	4.7473	1.6090
GA-PS	2.0039	4.9958	1.0044	4.0041	1.6197	1.2259	0.0524	1.0514	0.0105	6.2919	4.7211	1.5830
SA	1.8989	5.1011	1.1010	3.8989	1.3439	1.3231	0.2234	1.1483	0.0489	6.3303	4.7613	1.5237
SA-PS	1.9213	4.9214	1.0783	3.9213	1.7453	1.3001	0.1955	1.1261	0.0401	6.3216	4.7490	1.5341

Table 9: Performance of 1-L-type array for sources located on reference axis [15].

Scheme	s_1	s_2	s_3	s_4	θ_1 (rad)	θ_2 (rad)	θ_3 (rad)	θ_4 (rad)	ϕ_1 (rad)	ϕ_2 (rad)	ϕ_3 (rad)	ϕ_4 (rad)
Desired	2.0000	5.0000	1.0000	4.0000	1.5702	1.2217	0.0000	1.0472	0.0000	6.2832	4.7124	1.5702
GA	2.0163	4.9837	1.0162	3.9837	1.7069	1.2381	0.1396	1.0635	0.0357	6.3190	4.7483	1.6059
PS	2.0425	4.9575	1.0426	4.0426	1.7698	1.2643	0.1991	1.0897	0.0598	6.3430	4.7721	1.6299
GA-PS	1.9917	5.0083	1.0083	4.0083	1.4661	1.2300	0.1065	1.0555	0.0375	6.2798	4.7301	1.5910
SA	2.1263	5.1263	0.8737	3.8836	1.8500	1.3480	0.2741	1.1735	0.0792	6.3467	4.7741	1.5067
SA-PS	1.9068	5.0932	0.9068	4.0932	1.3334	1.3150	0.2287	1.1405	0.0668	6.3328	4.7563	1.265

Table 10: Means, variances, and standard deviations at 10 dB noise for different elevation angles and fixed azimuth angle by using PM with parallel-shape array [8].

θ in radians for $\phi = 0.6109$ (rad)	Mean of θ (rad)	Variance of θ (rad)	Standard deviation of θ (rad)
1.2392	1.2227	0.0123	0.0146
1.2915	1.2728	0.0171	0.0167
1.3439	1.3207	0.0228	0.0200
1.3963	1.3696	0.0403	0.0265
1.4486	1.4155	0.0822	0.0379
1.5010	1.4552	0.1250	0.0467
1.5533	1.4784	0.1631	0.0534

Table 11: Means, variances, and standard deviations at 10 dB noise for different elevation angles and fixed azimuth angle by using GA-PS with 1-L-shape array [15].

θ in radians for $\phi = 0.6109$ (rad)	Mean of θ (rad)	Variance of θ (rad)	Standard deviation of θ (rad)
1.2392	1.2394	$2.0963e-006$	$1.9128e-004$
1.2915	1.2913	$2.2918e-006$	$2.0000e-004$
1.3439	1.3436	$2.4819e-006$	$6.5816e-004$
1.3963	1.3965	$3.8608e-006$	$2.5959e-004$
1.4486	1.4493	$2.1907e-006$	$1.9554e-004$
1.5010	1.5012	$3.6759e-006$	$2.5329e-004$
1.5533	1.5535	$2.3424e-006$	$2.0219e-004$

$16 \times K$)) plus the multiplications involved in crossover which is approximately $16 \times Q^2$ and the multiplication required for PS which is $16 \times K$. So, the total number of major multiplications involved in GA-PS for 2-L-shape array is $O(Q^2((3+32\times K))+16\times K)$. Similarly, the major computations required for GA-PS with 1-L-shape array are $O(Q^2((3 + 20 \times K)) + 20 \times K))$, where Q is the number of particles which is 12 in this work. The GA-PS technique with 2-L-shape array is less computationally expensive as compared to PM scheme with parallel-shape array [8]. However, it is little more computationally expensive from GA-PS with 1-L-shape array [15].

Table 12: Means, variances, and standard deviations at 10 dB noise for different elevation angles and fixed azimuth angle by using GA-PS with 2-L-shape array.

θ in radians for $\phi = 0.6109$ (rad)	Mean of θ	Variance of θ	Standard deviation of θ
1.2392	1.2392	$2.6389e-007$	$6.7866e-005$
1.2915	1.2915	$1.9565e-007$	$5.8436e-005$
1.3439	1.3439	$4.0858e-007$	$8.4446e-005$
1.3963	1.3964	$2.5674e-007$	$6.6940e-005$
1.4486	1.4487	$2.3073e-007$	$6.3459e-005$
1.5010	1.5011	$5.9533e-007$	$1.0193e-004$
1.5533	1.5534	$2.0944e-007$	$6.0460e-005$

Case 9. In this simulation, we compared the RMSE of GA-PS used for 2-L-shape array with its counterpart used for 1-L-shape array [15] as well as with PM for parallel-shape array [8]. In this, a single source is considered which has elevation and azimuth angles 1.0472(rad) and 1.9199(rad), respectively. The values of signal to noise ratio (SNR) are ranging from 5 dB to 25 dB. For GA-PS with L-shape arrays, we have used $10 \log \times \sqrt{(\text{MSE})}$ where MSE is defined in (16). It is quite obvious from Figure 6, that GA-PS with 2-L-shape array maintained minimum values of RMSE for all values of SNR. The second best RMSE is maintained by another GA-PS technique with 1-L-shape array.

Table 13: Comparison among 2-L-shape aray, 1-L-shape array [15] and parallel-shape array [8].

Property	Parallel-shape array [8]	1-L-shape array [15]	2-L-shape array
Scheme used	PM	GA-PS	GA-PS
Elevation and azimuth angles range	$(0, \pi/2)$, $(0, 2\pi)$	$(0, \pi/2)$, $(0, 2\pi)$	$(0, \pi)$, $(0, 2\pi)$
Number of estimated sources	2	2	2
Number of sensors required	33	7	4
Number of Snapshots required	$M * T$	1	1
Pair matching	Required	Not required	Not required
Failure estimation	1.2217 (rad) to 1.5708 (rad)	No failure	No failure

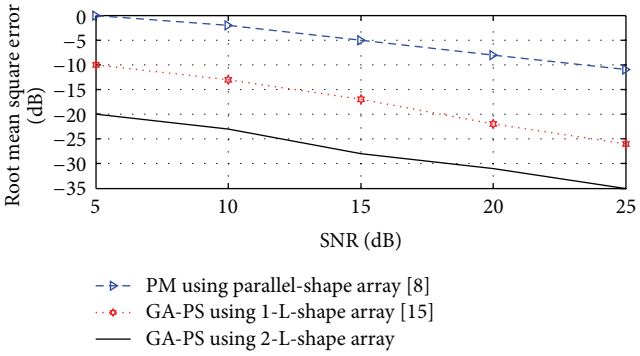

Figure 6: Root mean square error versus SNR.

Case 10. In Table 13, some general properties of parallel-shape array [8], 1-L-shape array [15] and 2-L-shape array are listed. The main drawbacks of parallel-shape array with PM method include estimation failure in the range of 1.2217 (rad) to 1.5708 (rad), its computational complexity, pair matching problem, and need of more sensors. Some of the drawbacks are covered in 1-L-shape array by using GA-PS technique. However, the main disadvantage of 1-L-shape array [15] is the range limitation of elevation angles beyond $\pi/2$, and it also requires more sensors. The 2-L-shape array with GA-PS technique is more effective and requires not only a minimum number of sensors but also covers the range of elevation angle beyond $\pi/2$ to π which is of great practical importance in mobile communication [21].

5. Conclusion and Future Work Direction

In this work, five techniques, that is, GA, PS, SA, SA-PS, and GA-PS, are used to jointly estimate amplitude, elevation angle and azimuth angle of far field sources impinging on 2-L-shape array. It has been shown through various simulations that the hybrid GA-PS technique is the best technique among them. It was also found that the GA-PS technique used for 2-L shape array performed well in terms of estimation accuracy, convergence rate, RMSE, number of sensors required as compared to 1-L-shape array and PM for parallel-shape array. Hence, GA-PS approach with 2-L-shape array is more practical and less expensive in terms of hardware budget for wireless communications.

In future, one can look into same hybrid approach for null steering and sidelobe reduction as well.

References

[1] Z. U. Khan, A. Naveed, I. M. Qureshi, and F. Zaman, "Independent null steering by decoupling complex weights," *IEICE Electronics Express*, vol. 8, no. 13, pp. 1008–1013, 2011.

[2] M. A. Atique-ur-Rehman, F. zaman, I. M. Qureshi, and Y. A. Sheikh, "Null and sidelobes adjustment of damaged array using hybrid computing," in *Proceedings of the IEEE International conference on Emerging Technology (ICET '12)*, pp. 386–389, Islamabad, Pakistan, 2012.

[3] H. Krim and M. Viberg, "Two decades of array signal processing research: the parametric approach," *IEEE Signal Processing Magazine*, vol. 13, no. 4, pp. 67–94, 1996.

[4] Q. I. Cheng, "Further study of the pencil-MUSIC algorithm," *IEEE Transactions on Aerospace and Electronic Systems*, vol. 32, no. 1, pp. 284–299, 1996.

[5] Y. Hua, T. K. Sarkar, and D. D. Weiner, "An L-shaped array for estimating 2-D directions of wave arrival," *IEEE Transactions on Antennas and Propagation*, vol. 39, no. 2, pp. 143–146, 1991.

[6] T. H. Liu and J. M. Mendel, "Azimuth and elevation direction finding using arbitrary array geometries," *IEEE Transactions on Signal Processing*, vol. 46, no. 7, pp. 2061–2065, 1998.

[7] V. S. Kedia and B. Chandna, "A new algorithm for 2-D DOA estimation," *Signal Processing*, vol. 60, no. 3, pp. 325–332, 1997.

[8] Y. Wu, G. Liao, and H. C. So, "A fast algorithm for 2-D direction-of-arrival estimation," *Signal Processing*, vol. 83, no. 8, pp. 1827–1831, 2003.

[9] F. Zaman, I. M. Qureshi, A. Naveed, and Z. U. Khan, "Real time direction of arrival estimation in noisy environment using particle swarm optimization with single snapshot," *Research Journal of Applied Sciences, Engineering and Technology*, vol. 4, no. 13, pp. 1949–1952, 2012.

[10] Y. A. Sheikh, F. Zaman, I. M. Qureshi, and M. Atique-ur-Rehman, "Amplitude and direction of arrival estimation using differential evolution," in *IEEE conference on Emerging Technology (ICET)*, pp. 386–389, Islamabad, Pakistan, 2012.

[11] A. K. Junaid, M. A. Z. Raja, and I. M. Qureshi, "Stochastic computational approach for complex non-linear ordinary differential equations," *Chinese Physics Letters*, vol. 28, Article ID 020206, 2011.

[12] A. K. Junaid, M. A. Z. Raja I, and M. Qureshi, "Numerical treatment of nonlinear Emden-Fowler equation using Stochastic Technique," *Annals of Mathematics and Artificial Intelligence*, vol. 63, no. 2, pp. 185–207, 2011.

[13] F. Zaman, I. M. Qureshi, A. Naveed, and Z. U. Khan, "Joint estimation of amplitude, direction of arrival and range of near field sources using memetic computing," *Progress in Electromagnetics Research C*, vol. 31, pp. 199–213, 2012.

[14] F. Zaman, J. A. Khan, Z. U. Khan, and I. M. Qureshi, "An application of hybrid computing to estimate jointly the amplitude and direction of arrival with single snapshot," in *Proceedings of the IEEE 10th IBCAST Conference*, Islamabad, Pakistan, 2012.

[15] F. Zaman, I. M. Qureshi, A. Naveed, J. A. Khan, and R. M. A. Zahoor, "Amplitude and directional of arrival estimation: comparison between different techniques," *Progress in Electromagnetics Research B*, vol. 39, pp. 319–335, 2012.

[16] F. Harabi, H. Changuel, and A. Gharsallah, "Direction of arrival estimation method using A 2-L shape arrays antenna," *Progress in Electromagnetics Research*, vol. 69, pp. 145–160, 2007.

[17] J. De Vicente, J. Lanchares, and R. Hermida, "Placement by thermodynamic simulated annealing," *Physics Letters A*, vol. 317, no. 5-6, pp. 415–423, 2003.

[18] X. Zhang and J. Ma, "Pattern search methods for finite minimax problems," *Journal of Applied Mathematics and Computing*, vol. 32, pp. 491–506, 2010.

[19] L. Zhang, Y.-C. Jiao, B. Chen, and H. Li, "Orthogonal genetic algorithm for planar thinned array designs," *International Journal of Antennas and Propagation*, vol. 2012, Article ID 319037, 7 pages, 2012.

[20] H. Gargama, S. K. Chaturvedi, and A. K. Thakur, "On the design and reliability analysis of electromagnetic absorbers using real-coded genetic algorithm and monte carlo simulation," *Progress in Electromagnetics Research B*, vol. 43, pp. 169–187, 2012.

[21] N. A. H. M. Tayem, *Direction of arrival angle estimation schemes for wirelerss communication systems [Ph.D. thesis]*, Wichita State University, 2005.

Hindawi Publishing Corporation
International Journal of Antennas and Propagation
Volume 2013, Article ID 649602, 5 pages
http://dx.doi.org/10.1155/2013/649602

Research Article

Adaptive Prediction of Channels with Sparse Features in OFDM Systems

Changwei Lv, Shujuan Hou, and Wenbo Mei

School of Information and Electronics, Beijing Institute of Technology, Beijing 100081, China

Correspondence should be addressed to Shujuan Hou; shujuanhou@bit.edu.cn

Received 30 January 2013; Revised 21 March 2013; Accepted 17 April 2013

Academic Editor: Alfonso Muñoz-Acevedo

A time domain channel prediction method exploiting features of sparse channel is proposed for orthogonal frequency division multiplexing (OFDM) systems. The proposed predictor operates in the time domain on each channel tap and separates the negligible taps from significant channel taps before performing prediction. We also compare the proposed prediction method with the classical frequency domain method realized at each OFDM subcarrier and demonstrate that our method increases the prediction accuracy and reduces the computational complexity. Simulations on the physical channel model verify the performance of the proposed method.

1. Introduction

OFDM has received considerable interest for its advantages of converting frequency-selective fading channels into a parallel collection of frequency flat subchannels and reducing intersymbol interference (ISI) [1]. Adaptive transmission is a promising technique to provide a good throughput performance for OFDM systems [2]. In adaptive transmission, accurate channel state information (CSI) for the upcoming transmission frame is needed. In fast variation channels, the estimated CSI will be soon outdated, and channel prediction is the sole way to provide the future CSI.

Due to the parallel transmission scheme of OFDM systems, existing channel predictors are often realized at each OFDM subcarrier in the frequency domain [3]. The variation at each subcarrier is a combined variation of multiple taps, which makes it difficult to accurately predict the channel. In the time domain, some effective channel predictors (such as [4]) have been proposed. In practical terms, wireless channels are often sparse [5]; that is, there are not so many channel taps with significant energy (if compared to the number of subchannels of OFDM), and several approaches have been proposed to exploit this property in channel estimation. One of the most widely used approaches is significant tap selection method [5, 6], which uses a measure to determine which channel tap is significant. In contrast to the significant tap selection approach, the matching pursuit type algorithm is employed in [7, 8] to estimate channel taps iteratively by maximizing the correlation of a column of the mixture matrix with the residual signal. More recently, the new field of compressive sensing has proposed effective solutions to exploit channel sparsity, such as [9, 10]. However, the existing time domain predictors ignore this sparsity of radio channel.

This paper presents a new time domain predictor exploiting the features of sparse channel for OFDM systems. Firstly, the proposed predictor transforms the estimated frequency domain channel samples in time domain and operates on each channel tap. Secondly, the predictor separates the negligible taps from the significant channel taps before performing prediction. The proposed predictor mainly has the following characteristics.

(1) The proposed channel predictor operates on channel taps in the time domain impulse response. Each channel tap contains a number of subpaths, while the variation at each subcarrier of OFDM is a combined variation of all taps. Thus, the single channel tap with less subpaths is more predictable than the subcarrier of OFDM [11].

(2) In sparse channel, many channel taps have no energy at all except for estimation noise. Separating those negligible channel taps from the significant ones

in channel will eliminate the noise perturbation and make the prediction more accurate.

(3) Since the number of significant channel taps is much smaller than that of OFDM subcarriers, the proposed time domain method operating on the significant channel taps has a much lower prediction complexity than the frequency domain method.

(4) As the number of significant channel taps to be predicted is small, we can employ the predictor with higher complexity but having a superior tracking ability for each tap, without worrying about the overall computational complexity.

The rest of this paper is organized as follows. Section 2 describes the system model. Section 3 proposes the time domain prediction method exploiting the features of sparse channel. Section 4 illustrates the performance evaluation, while Section 5 is the conclusion.

2. System Model

We consider an OFDM modulation system with K subcarriers operating over a wideband channel. The receiver architecture is shown in Figure 1. Note that the cyclic-prefix (CP) discarding is omitted in this figure. The received signal is

$$r[n] = \sum_{l=0}^{L_t-1} h[n,l]\, s[n-l] + z[n], \tag{1}$$

where L_t is the channel's maximum delay, $s[n]$ is the baseband transmit signal, $z[n]$ is additive noise, and $h[n,l]$ is the radio channel given as

$$h[n,l] = \sum_{i=0}^{L} h[n,l_i]\, \delta[l-l_i], \tag{2}$$

where $h[n,l_i]$ is the complex amplitude of ith tap at time n, and L is the number of channel taps. Note that L is usually much smaller than L_t due to the fact that the time domain impulse response of sparse channel consists of a large number of zero taps in the standard uniform tapped delay model.

In the receiver, the discrete-Fourier-transform (DFT) output frequency domain subcarrier symbol is [3]

$$R[m;k] = \mathrm{FFT}_K\{r[n]\} = H[m;k]\, S[m;k] + Z[m;k], \tag{3}$$

where $R[m;k]$ is the received signal at the kth subcarrier of the mth OFDM symbol, $S[m;k]$ is the transmitted signal modulating the kth subcarrier of the mth OFDM symbol, $Z[m;k]$ is the corresponding noise, and $H[m;k]$ is the channel coefficient given as

$$H[m;k] = \sum_{l=0}^{L_t-1} h[m;l]\, e^{-j2\pi lk/K}, \tag{4}$$

where $h[m;l]$ is the channel response of the lth delay in the mth OFDM symbol, and it is assumed to be constant over an OFDM symbol duration. Then, the DFT output $R[m;k]$ will be processed by the channel estimator, and we have the estimation result as [3]

$$\widehat{H}[m;k] = H[m;k] + \widehat{Z}[m;k], \tag{5}$$

where $\widehat{Z}[m;k]$ is the white Gaussian estimation noise caused by background noise and the receiver imperfections, with variance σ^2. Here, we define the estimation SNR as $\mathrm{SNR}_e = E[|H[m;k]|^2]/\sigma^2$.

Existing channel predictors for OFDM are often realized in the frequency domain. For the kth ($k = 0, 1, \ldots, K-1$) subcarrier, the frequency domain method is given by

$$\widetilde{H}[m+1;k] = \sum_{i=0}^{p-1} w_i^*[m;k]\, \widehat{H}[m-i;k], \tag{6}$$

where $\widetilde{H}[m+1;k]$ is the predicted channel sample at the kth subcarrier, $w_i[m;k]$ is the prediction coefficient at the kth subcarrier, and p is the prediction order. The prediction coefficients can be updated using adaptive algorithm, and it will be introduced in next section.

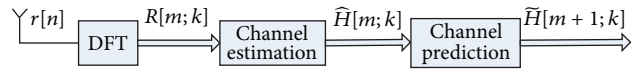

Figure 1: OFDM receiver.

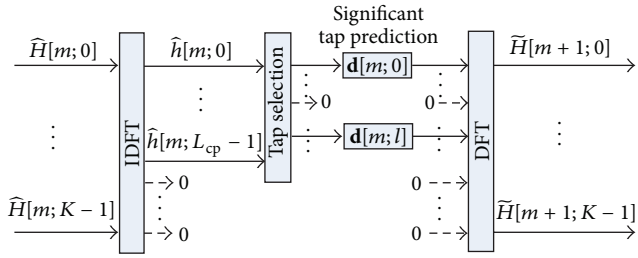

Figure 2: Time domain predictor for sparse channel.

3. The Proposed Time Domain Method

In OFDM systems, the entire channel is divided into many narrow parallel subchannels, and so it is easy to understand why the frequency domain methods realize at each OFDM subcarrier as (6). However, the frequency domain methods will be limited on the following grounds. Firstly, as introduced in Section 1, the subchannel of OFDM is not as predictable as the channel tap in time domain. Secondly, the number of OFDM subcarriers is much larger than that of taps in sparse channel, which leads to a high prediction complexity. Last but not least, the nonsignificant channel taps can be neglected to eliminate the noise perturbation and to make the prediction more accurate. The proposed time domain channel prediction method is described in the following.

For $l = 1, \ldots, L_{\text{cp}} - 1$,

Compare $\left|\underline{\widehat{h}}_1\right|^2, \ldots, \left|\underline{\widehat{h}}_{L_{\text{cp}}}\right|^2$:

(1) Select the L_s significant taps, and perform prediction on each significant tap;

(2) Set the other $L_{\text{cp}} - L_s$ taps as zeros.

For $l = L_{\text{cp}}, \ldots, K - 1$,

Set $\widetilde{h}[m+1; l] = 0$ directly.

(Note: $\left|\underline{\widehat{h}}_l\right|^2$ is the average power of lth tap, averaged from the previous estimation samples.)

Algorithm 1: Tap selection algorithm.

3.1. Predictor Architecture. The time domain predictor for sparse channel is shown in Figure 2. The input of the proposed predictor is the frequency domain channel estimation coefficients $\widehat{H}[m;k]$, $k = 0, 1, \ldots, K-1$. Firstly, a K-point IDFT is applied to the input, which yields

$$\widehat{h}[m;l] = \text{IFFT}_K\left\{\widehat{H}[m;k]\right\}. \tag{7}$$

Secondly, tap selection algorithm will select the significant channel taps. Then, if $\widehat{h}[m;l]$, the lth estimated tap is significant, and it will be applied to the predictor with prediction coefficients $\mathbf{d}[m;l]$; otherwise, it will be set as zero. Finally, the predicted time domain channel coefficients will be transformed back to frequency domain

$$\widetilde{H}[m+1;k] = \text{FFT}_K\left\{\widetilde{h}[m+1;l]\right\}. \tag{8}$$

In the proposed method, an additional operation is transformation between time and frequency domains. Due to the employment of FFT implementations, the computational complexity of the transformation is very low. In the following, we introduce the tap selection and the adaptive prediction algorithms.

3.2. Tap Selection. Assume that the CP length of OFDM system is L_{cp}, and the channel's maximum delay does not exceed L_{cp}. Then, for $l = 0, \ldots, L_{\text{cp}} - 1$, the time domain channel estimation of (7) can be written as

$$\widehat{h}[m;l] = \begin{cases} h[m;l] + \varsigma[m;l], & \text{significant tap,} \\ \varsigma[m;l], & \text{zero-valued tap,} \end{cases} \tag{9}$$

while for $l = L_{\text{cp}}, \ldots, K-1$, we have

$$\widehat{h}[m;l] = \varsigma[m;l], \tag{10}$$

where $\varsigma[m;l] = \text{IFFT}_K\{\widehat{Z}[m;k]\}$ is the noise, in time domain. In this paper, we use the most significant channel tap approach [5] to identify the significant channel taps. The selection algorithm is shown in Algorithm 1.

3.3. Adaptive Prediction. Since radio channel is time varying in practice, the predictor should adjust itself with the goal of tracking the change of channel. Least-mean-squares (LMS) and recursive-least-squares (RLS) [12] are two major adaptive methods used for channel prediction. It is well known that the LMS predictor is simple to implement, but its ability to track time-varying channel is also limited. In contrast, RLS predictor has a superior tracking ability, but with a much higher complexity. As a result, when computational complexity is a primary concern, the RLS will not be broadly adopted by the frequency domain methods, as too many predictors will be involved in such methods. In this paper, through exploiting the features of sparse channel, the proposed method only uses a small number of predictor. Hence, the RLS can be adopted for channel prediction without worrying about the prediction complexity. For significant channel taps, the RLS predictor is as follows:

$$\widetilde{h}[m+1;l] = \mathbf{d}^H[m;l]\,\widehat{\mathbf{h}}[m;l], \tag{11}$$

where

$$\begin{aligned} \mathbf{d}[m;l] &= \left[d_0[m;l], \ldots, d_{p-1}[m;l]\right]^T, \\ \widehat{\mathbf{h}}[m;l] &= \left[\widehat{h}[m;l], \ldots, \widehat{h}[m-p+1;l]\right]^T \end{aligned} \tag{12}$$

are the prediction coefficient vector and the estimated time domain channel coefficient vector, and p is the prediction order. The updated equation of RLS is as follows:

$$\mathbf{d}[m;l] = \mathbf{d}[m-1;l] + \mathbf{k}[m-1;l]\,e^*[m;l], \tag{13}$$

where

$$e[m;l] = \widehat{h}[m;l] - \mathbf{d}^H[m-1;l]\,\widehat{\mathbf{h}}[m-1;l] \tag{14}$$

is the prediction error, and

$$\mathbf{k}[m;l] = \frac{\mathbf{p}[m-1;l]\,\widehat{\mathbf{h}}[m;l]}{\lambda + \widehat{\mathbf{h}}^H[m;l]\,\mathbf{p}[m-1;l]\,\widehat{\mathbf{h}}[m;l]} \tag{15}$$

is the RLS gain vector, where λ is the forgetting factor. Further, the matrix $\mathbf{p}[m;k]$ can be calculated recursively as

$$\mathbf{p}[m;l] = \frac{1}{\lambda}\left(\mathbf{I} - \mathbf{k}[m;l]\,\widehat{\mathbf{h}}^H[m;l]\right)\mathbf{p}[m-1;l]. \tag{16}$$

4. Simulation Results

In this paper, we compare the NMSE performance of five channel prediction methods.

(1) *Frequency domain (FD) method* shows prediction at each OFDM subcarrier in the frequency domain; that is, $\widehat{H}[m;k]$, $k = 0, 1, \ldots, K-1$.

(2) *Time domain (TD) method* shows prediction on each channel tap in the time domain; that is, $\widehat{h}[m;l]$, $l = 0, 1, \ldots, K-1$.

(3) *The first L_{cp} taps of time domain* (L_{cp}*-TD*) show prediction on each of the first L_{cp} channel taps; that is, $\widehat{h}[m;l]$, $l = 0, 1, \ldots, L_{\text{cp}}-1$.

(4) *The L_s significant taps of time domain* (L_s*-TD*) show prediction on each of the L_s significant channel taps, which are selected by the tap selection algorithm.

(5) *Exact time domain (exact-TD) method* shows that the L channel taps are known exactly, and the prediction is operated on each of the L channel taps. This method provides a reference in the comparison.

The five methods all employ RLS predictors for prediction. All RLS predictors have the same parameters: the order $p = 10$ and the forgetting factor $\lambda = 0.9$.

In this paper, we use the standardized 3GPP channel models [13], which model the realistic scattering environments and generate realistic fading datasets, to test our prediction algorithm. The urban microscenario with $L = 6$ taps is simulated for performance evaluation. The carrier frequency is 2 GHz and the velocity of MS is 10 m/s, which leads to a maximum Doppler shift about $f_{\max} = 67$ Hz. The data sampling rate is set as 8 MHz, while the sampling rate used for channel estimation is set as $f_s = 8 f_{\max}$, which is much lower than the data rate and higher than double of the maximum Doppler shift. In this simulation, 200 channel samples are generated. The first 100 samples are used for observation and the prediction training, while the second 100 samples are for performance evaluation. The FFT size of OFDM system is 128, the CP length L_{cp} is 32, and the number of significant taps is set as $L_s = 2L$ according to [5].

The performance of different predictors is compared in terms of the NMSE defined as

$$\text{NMSE} = \frac{E\left[\left\|\mathbf{H}(m) - \widetilde{\mathbf{H}}(m)\right\|^2\right]}{E\left[\left\|\mathbf{H}(m)\right\|^2\right]}, \tag{17}$$

where

$$\begin{aligned} \mathbf{H}(m) &= [H[m;0], \ldots, H[m;K-1]]^T, \\ \widetilde{\mathbf{H}}(m) &= \left[\widetilde{H}[m;0], \ldots, \widetilde{H}[m;K-1]\right]^T \end{aligned} \tag{18}$$

are real and predicted frequency domain channel coefficient vectors.

The NMSE performance versus the estimation SNR for different predictors is shown in Figure 3. According to Figure 3, we have the following results.

(1) The NMSE performance of TD method is better than that of FD method. It is because the single channel tap is more predictable than the subcarrier of OFDM whose variation is a combined variation of all taps.

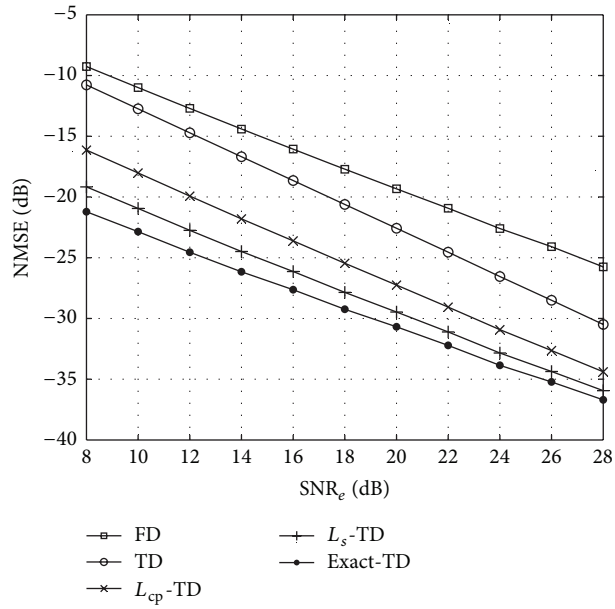

Figure 3: NMSE performance comparison for different channel predictors.

(2) The performance of L_{cp}-TD is better than TD method. It is because the noise taps whose delays are larger than L_{cp} are separated.

(3) The performance of L_s-TD is better than L_{cp}-TD. It is because L_s-TD can separate more negligible taps by exploiting sparse channel features.

(4) The exact-TD method provides a reference in the comparison. It represents the best NMSE performance achievable by exploiting the features of sparse channel.

(5) The numbers of RLS predictors employed by FD, TD, L_{cp}-TD, and L_s-TD are K, K, L_{cp}, and L_s, respectively. As L_s is small, L_s-TD has a lower computational complexity than the other three methods.

5. Conclusion

A new time domain approach for OFDM channel prediction is proposed, based on the features of sparse channel that many channel taps have no energy at all except for estimation noise, as well as the fact that the channel tap in time domain is more predictable than the subchannel in frequency domain. The proposed method separates the negligible channel taps and only performs prediction on the significant ones. Also, the RLS algorithm with superior tracking ability is employed to predict each significant tap. Although the coefficients update of RLS is complex, the overall computational complexity of the prediction method is not high, due to the limited quantity of significant channel taps. The effectiveness of the proposed approach is validated by the simulations on the physical channel model. As a result, the novel channel

prediction method can exploit the features of sparse channel and improve the prediction performance.

Future works will focus on the application of the proposed approach to adaptive transmission schemes in multiple antenna systems, including transmit selection diversity and adaptive beamforming.

References

[1] L. J. Cimini Jr., "Analysis and simulation of a digital mobile channel using orthogonal frequency division multiplexing," *IEEE Transactions on Communications*, vol. 33, no. 7, pp. 665–675, 1985.

[2] M. Sternad, T. Svensson, T. Ottosson, A. Ahlen, A. Svensson, and A. Brunstrom, "Towards systems beyond 3G based on adaptive OFDMA transmission," *Proceedings of the IEEE*, vol. 95, no. 12, pp. 2432–2455, 2007.

[3] A. Duel-Hallen, H. Hallen, and T. S. Yang, "Long range prediction and reduced feedback for mobile radio adaptive OFDM systems," *IEEE Transactions on Wireless Communications*, vol. 5, no. 10, pp. 2723–2732, 2006.

[4] D. Schafhuber and G. Matz, "MMSE and adaptive prediction of time-varying channels for OFDM systems," *IEEE Transactions on Wireless Communications*, vol. 4, no. 2, pp. 593–602, 2005.

[5] H. Minn and V. K. Bhargava, "An investigation into time-domain approach for OFDM channel estimation," *IEEE Transactions on Broadcasting*, vol. 46, no. 4, pp. 240–248, 2000.

[6] C. Carbonelli, S. Vedantam, and U. Mitra, "Sparse channel estimation with zero tap detection," *IEEE Transactions on Wireless Communications*, vol. 6, no. 5, pp. 1743–1753, 2007.

[7] S. Kim, "Angle-domain frequency-selective sparse channel estimation for underwater MIMO-OFDM systems," *IEEE Communications Letters*, vol. 16, no. 5, pp. 685–687, 2012.

[8] X. Jiang, W.-J. Zeng, and E. Cheng, "A fast algorithm for sparse channel estimation via orthogonal matching pursuit," in *Proceedings of the 73rd Vehicular Technology Conference (VTC Spring)*, pp. 1–5, May 2011.

[9] C. R. Berger, Z. Wang, J. Huang, and S. Zhou, "Application of compressive sensing to sparse channel estimation," *IEEE Communications Magazine*, vol. 48, no. 11, pp. 164–174, 2010.

[10] W. U. Bajwa, J. Haupt, A. M. Sayeed, and R. Nowak, "Compressed channel sensing: a new approach to estimating sparse multipath channels," *Proceedings of the IEEE*, vol. 98, no. 6, pp. 1058–1076, 2010.

[11] T. Eyceoz, S. Hu, and A. Duel-Hallen, "Performance analysis of long range prediction for fast fading channels," in *Proceedings of the 33rd Annual Conference on Information Sciences and Systems (CISS '99)*, vol. 2, pp. 656–661, 1999.

[12] S. Haykin, *Adaptive Filter Theory*, Prentice Hall, 3rd edition, 2002.

[13] "Spatial channel model for multiple input multiple output (MIMO) simulations," 3GPP Technical Report 25. 996 V6. 1. 0, Chichester, UK, 2003, http://www.3gpp.org/ftp/Specs/html-info/25996.htm.

Hindawi Publishing Corporation
International Journal of Antennas and Propagation
Volume 2013, Article ID 976301, 7 pages
http://dx.doi.org/10.1155/2013/976301

Application Article

Implementation of a Zero-Forcing Precoding Algorithm Combined with Adaptive Beamforming Based on WiMAX System

Hyunwook Yang and Seungwon Choi

School of Electrical and Computer Engineering, Hanyang University, 17 Haengdang-Dong, Seongdong-Gu, Seoul 133-791, Republic of Korea

Correspondence should be addressed to Seungwon Choi; choi@dsplab.hanyang.ac.kr

Received 1 February 2013; Revised 26 March 2013; Accepted 2 April 2013

Academic Editor: Juan Valenzuela-Valdes

We propose a novel precoding algorithm that is a zero-forcing (ZF) method combined with adaptive beamforming in the Worldwide Interoperability for Microwave Access (WiMAX) system. In a Multiuser Multiple-Input Multiple-Output (MU-MIMO) system, ZF is used to eliminate the Multiple Access Interference (MAI) in order to allow several users to share a common resource. The adaptive beamforming algorithm is used to achieve the desired SNR gain. The experimental system consists of a WiMAX base station that has 2 MIMO elements, each of which is composed of three-array antennas and two mobile terminals, each of which has a single antenna. Through computer simulations, we verified that the proposed method outperforms the conventional ZF method by at least 2.4 dB when the BER is 0.1%, or 1.7 dB when the FER is 1%, in terms of the SNR. Through a hardware implementation of the proposed method, we verified the feasibility of the proposed method for realizing a practical WiMAX base station to utilize the channel resources as efficiently as possible.

1. Introduction

MU-MIMO technology [**?** **?**] and array antenna technology, which is often referred to as a beamforming system [**?** **?**], have received extremely keen interest as next-generation communication technologies because they allow for drastic enhancement of system throughput and energy efficiency.

To realize an MU-MIMO system, the problem of Multiple Access Interference (MAI) caused by sharing a common resource by multiple mobile terminals must be resolved. In order to remove the MAI, a signal vector to be transmitted from the base station is precoded. In this paper, we adopt a zero-forcing (ZF) precoder to remove the MAI that employs an inversion of the channel matrix as a weight of the transmitting signal vector [**?**]. ZF is known to be the simplest precoding method. ZF eliminates the MAI by using the inverse of channel matrix as its precoder.

To realize a beamforming system, the phase to be applied to each antenna element must be determined in such a way that the signal transmitted to the target mobile terminal becomes in-phase when it arrives at the target terminal. In order to control the phase of each transmitted signal as described earlier, the Direction of Arrival (DOA) of the target user must be known to the base station. However, the DOA is not generally known. Based on the previous conditions, we adopted the Ordinary Lagrange Beamforming (OLB) algorithm to estimate the DOA for the target user(s) [**?**].

We implemented the precoding algorithm combined with the OLB on a WiMAX system. The base station consists of two MIMO elements, each of which is composed of a three-element beamforming array. Through computer simulations, we verify that the proposed method outperforms conventional ZF by about 2.4 dB when the BER is 0.1%, or by 1.7 dB when the FER is 1%. Furthermore, the proposed method outperforms conventional ZF even further when the SNR becomes lower, because the proposed technique reduces the channel estimation error.

This paper is organized as follows. Section 2 describes the system models and algorithms. And the implementation is

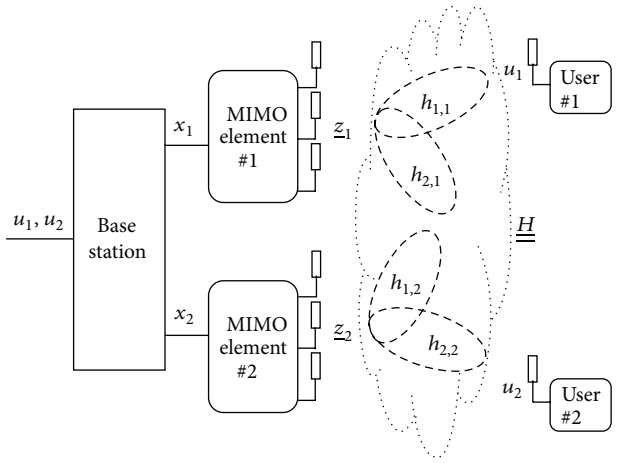

Figure 1: System model of MU-MIMO with adaptive beamforming.

also shown in Section 2. Section 3 compares the performance of the proposed and conventional methods, while Section 4 concludes this paper.

2. Materials and Methods

2.1. System Model and Algorithm. Figure 1 illustrates the structure of our system, which includes a base station consisting of two MIMO elements, each of which is composed of three-element array, and two users, each of which adopts a single antenna. We assume that the antenna separation is $\lambda/2$ where λ denotes the wavelength at the carrier frequency. And we assume that a channel correlation between array antennas is very high. In Figure 1, u_k is the modulation signal for the kth user, and x_i is the precoded signal to be transmitted from the ith MIMO element, with

$$\underline{x} = \frac{\underline{\underline{H}}^{-1}\underline{u}}{\left\|\underline{\underline{H}}^{-1}\underline{u}\right\|} \tag{1}$$

for $\underline{u} = [u_1 \;\; u_2]^T$ and $\underline{x} = [x_1 \;\; x_2]^T$. In (1), $\underline{\underline{H}}$ is a 2×2 Rayleigh MIMO channel matrix, and $h_{k,i}$ denotes the channel response for the (k, i)th component of $\underline{\underline{H}}$, which means the channel between the ith MIMO element and the kth user. Note that the channel inversion, $\underline{\underline{H}}^{-1}$, is the precoder. When using the ZF as the precoder, two users can share a common resource without the MAI. The precoded signal x_i is weighted by the vector $\underline{w}_i = [w_{1,i} \;\; w_{2,i} \;\; w_{3,i}]^T$ for beamforming, where $l = 1, 2, 3$ is the antenna index and i is the MIMO element index. Thus, the array output is determined as

$$\underline{z}_i = \underline{w}_i \cdot x_i, \tag{2}$$

where $\underline{z}_i = [z_{1,i} \;\; z_{2,i} \;\; z_{3,i}]^T$ is the beamformed signal vector consisting of a signal $z_{l,i}$ to be transmitted from the lth array antenna of the ith MIMO element, while the weight vector $\underline{w}_i$ is derived by the OLB algorithm in an uplink system as mentioned earlier. The transmitted signal vector is normalized to 1. The base station estimates the channel state information (CSI) of each user to determine the precoder and beamforming weight vector.

OLB Algorithm. It is assumed that the power of a desired signal is much larger than that of interference signals. In this circumstance, the OLB algorithm is used to find the weight vector that maximizes the norm of the beamformed signal vector. During the process of demultiplexing, the desired signal has processing gain. Therefore, we can use the OLB algorithm in a WiMAX system. In the uplink system, the process of finding the weight vector $\underline{w}_i(n)$ for the nth sampling time can be summarized as shown in (3)–(6) [**?**]. Consider

$$\underline{\underline{R}}_{zz}(n) = f \cdot \underline{\underline{R}}_{zz}(n-1) + \underline{z}_i(n) \cdot \underline{z}_i^{\,H}(n), \tag{3}$$

$$\underline{\nabla}(n) = 2\left(\underline{\underline{R}}_{zz}(n) \cdot \underline{w}_i(n-1) - \gamma(n) \cdot \underline{w}_i(n-1)\right), \tag{4}$$

$$\gamma(n) = b \pm \frac{\sqrt{b^2 - ac}}{a}$$

$$\Big(\text{where } a = \mu,$$

$$b = \mu \underline{w}_i^{\,H}(n-1) \cdot \underline{\underline{R}}_{zz}(n) \cdot \underline{w}_i(n-1),$$

$$c = b + 2\underline{w}_i^{\,H}(n-1) \cdot \underline{\underline{R}}_{zz}(n) \cdot \underline{w}_i(n-1)\Big), \tag{5}$$

$$\underline{w}_i(n) = \underline{w}_i(n-1) + \left(\frac{1}{2}\right)\mu \cdot \underline{\nabla}(n). \tag{6}$$

In (3)–(6), $\underline{\underline{R}}_{zz}(n)$ is the autocovariance of the signal vector $\underline{z}_i(n)$, and μ denotes the adaptive gain, which is a major factor for determining the convergence speed of the adaptive procedure of finding the DOA shown in (3)–(6) while f is a forgetting factor with $0 < f < 1$.

2.2. Implementation. In this paper, we implement the procedure of the beamforming MU-MIMO system. We selected a WiMAX system for our implementation [**?**] and modified the system to be an MU-MIMO system. The system parameters of the implemented system are shown in Table 1.

The implementation of the WiMAX system combined with the proposed scheme, which is shown in Figure 2, can be described for each part in more detail as follows.

2.2.1. Calculating the Beamforming Weight

(a) Demultiplexing. In the MU-MIMO system, the users share a data subcarrier, but the pilot subcarrier cannot be shared. Figure 3 illustrates the pilot subcarrier in the uplink frame structure.

As shown in Figure 3, since the pilot is not shared among the users, the demultiplexing can fully exploit the processing gain. Therefore, we used the pilot to estimate the DOA of

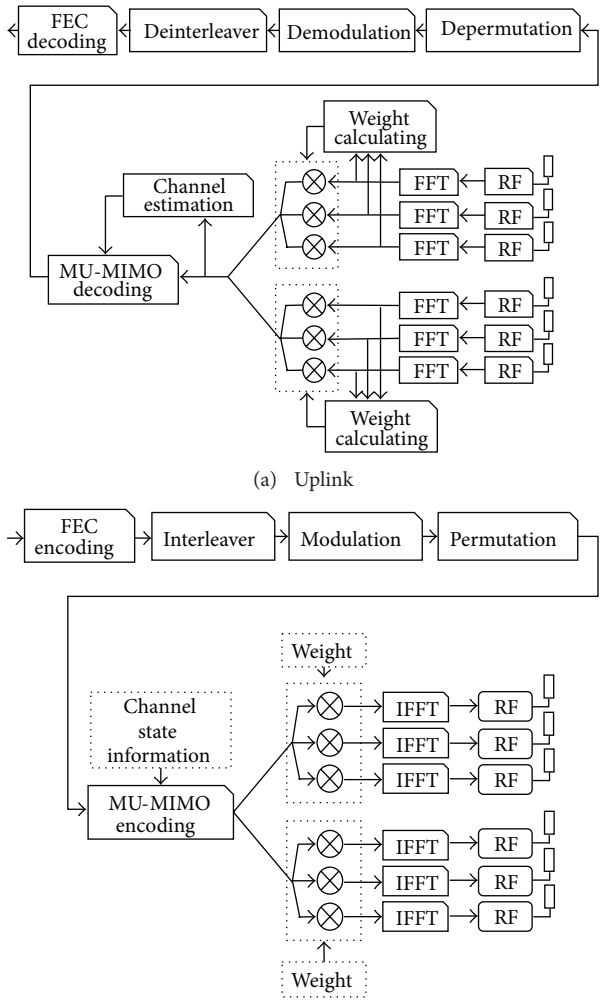

Figure 2: Required procedure for realizing the proposed system.

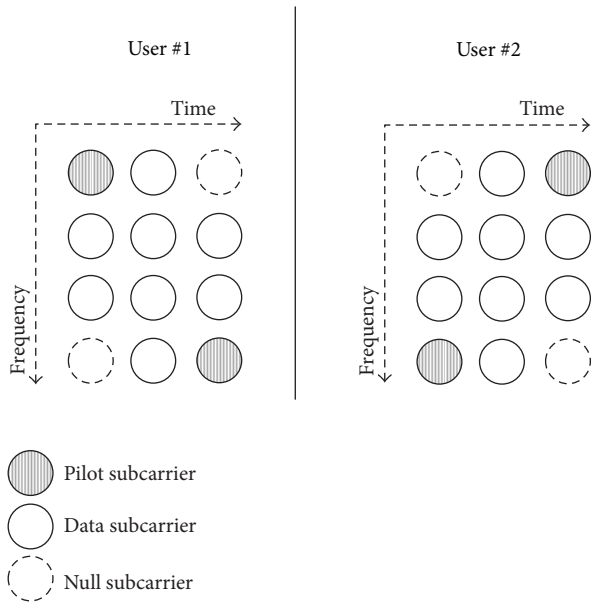

Figure 3: Arrangement of pilot subcarrier in uplink frame.

Table 1: Parameters for implementation.

Parameters	Base station	User
Number of antennas	$3 * 2$	1
Precoding	ZF	
Beamforming	OLB algorithm	
Waveform	WiMAX	
FEC	Convolutional Turbo Coding, $R = 1/2$	
Frame duration (DL/UL)	3.1104 ms/1.728 ms (for 5 ms)	
TTG/RTG	121.2 μs/40.4 μs (161.6 μs)	
FFT size	1024	
Number of symbols (DL/UL)	27/15	
Modulation scheme	16 QAM	
f_c	2.3 GHz	

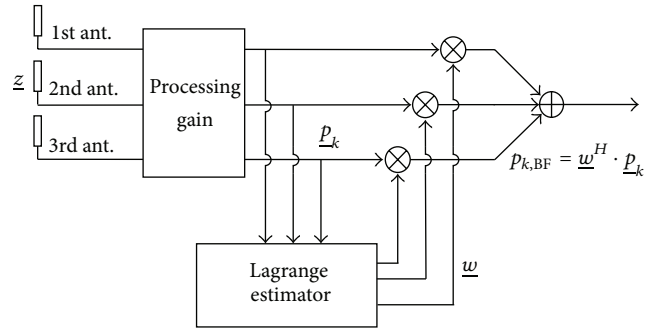

Figure 4: Block diagram of beamforming system.

the desired user. In addition, the system throughput can be doubled because a data subcarrier is shared by two users.

(b) OLB Algorithm. To beamform the signal of the kth user, the weight vector is derived by using the pilot vector $\underline{p}_k$ that belongs to the kth user. As mentioned earlier, in order to use the OLB algorithm, the desired signal has to have the largest norm of any of the other signals. The pilot signal, which is allocated differently for each user, has a processing gain. Figure 4 shows a block diagram of the beamforming system implemented with a three-antenna element, which adopts the OLB algorithm to abstract the pilot signal $p_{k,\mathrm{BF}}$ with a beamforming gain.

For the target users of the MU-MIMO system who share the frequency resource (i.e., subcarrier) of the common transmit data, the weight vector should be computed in such a way that the main lobe is provided in the direction of each of the target users sharing the common resource. Summing the weight vectors of all target user would be one way of achieving that purpose [**?**]. The final weight vector $\underline{w}$ can then be obtained as follows:

$$\underline{w} = \frac{\sum_{k=1}^{2} \underline{w}_k}{\left\| \sum_{k=1}^{2} \underline{w}_k \right\|}. \tag{7}$$

As shown in (7), the final weight vector $\underline{w}$ is generated by summing each user's weight vector $\underline{w}_k$ and then normalizing.

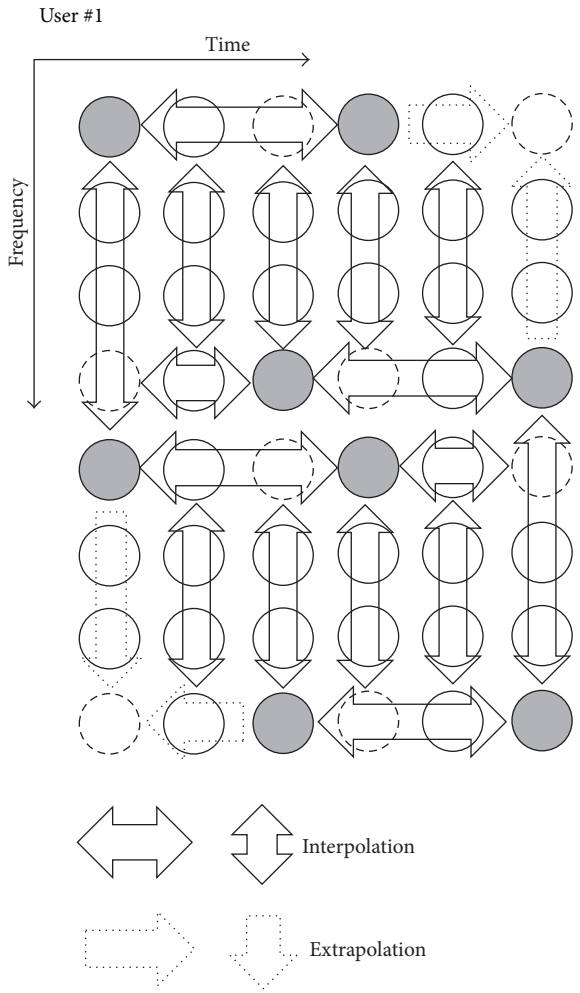

Figure 5: Procedure of channel estimation for user #1.

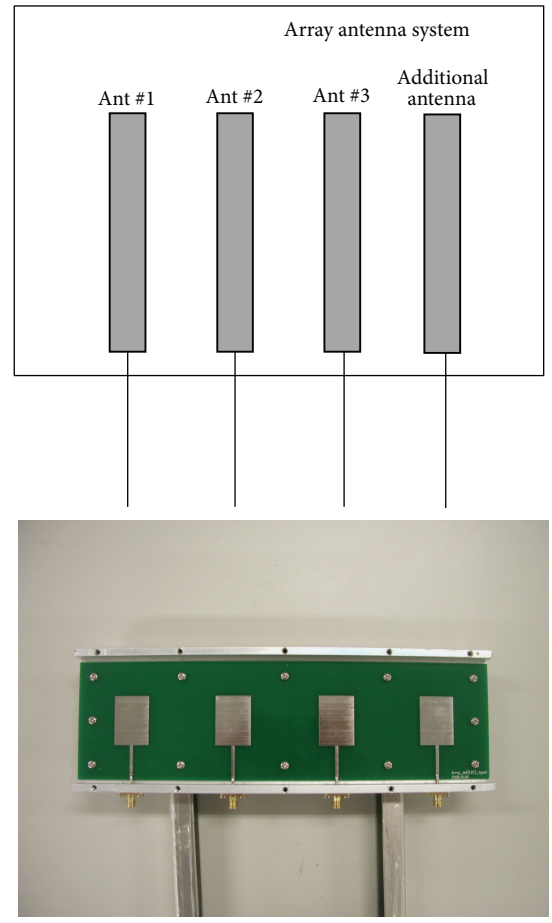

Figure 6: Array antenna system with added calibration antenna.

Therefore, the weight vector $\underline{w}_k$ for the kth user may disturb the other user's signals, all of which should be in-phase. Due to the reason mentioned earlier, beamforming technology in an MU-MIMO system does not generally provide beamforming gain exactly proportional to the number of antenna elements.

2.2.2. Channel Estimation. Channel estimation can be performed by using the pilot signals, the values of which are known at the receiver. In this paper, the channel estimation is first performed along the time axis and later along the frequency axis. Figure 5 illustrates the procedure of channel estimation for user #1.

As shown in Figure 3, the pilot signals are mapped on the grey subcarriers shown in Figure 5. As shown in Figure 5, interpolation or extrapolation is properly adopted, and the CSI is estimated depending upon the location of the data subcarrier. A dotted line indicates a blank. The empty subcarriers are for user #2's pilot signals. The CSIs of all users are estimated for each antenna element composing the proposed beamforming MU-MIMO system.

2.2.3. Precoding and Beamforming. The precoder for the uplink system is designed based on the CSI estimation described in Section 3.2. In this paper, ZF has been adopted as the precoder. When ZF is used as the precoder, two users can share the same resource without interference. As mentioned earlier, the channel inversion matrix is the ZF precoder. The CSI is estimated as shown in Figure 5. The precoded signal, which is transferred to the MIMO element, is then processed by the beamforming procedure shown in Figure 2(b). We constrained the transmit power to be one for the experimental tests as well as for the computer simulations.

2.2.4. Calibration. Since each antenna element and its associated path must exhibit a different phase characteristic from the others, even if the same signal is applied to the feeding port of each transmit antenna, each transmitted signal must exhibit a different phase characteristic. Calibration is the procedure of compensating for the phase differences between each of the antenna elements and the associated antenna paths. Therefore, if we want to reuse the weight vector derived in the uplink procedure in the downlink procedure, calibration is needed. Figure 6 illustrates the array antenna containing the calibration antenna. An additional antenna is utilized for transmitting or receiving a test signal to or from

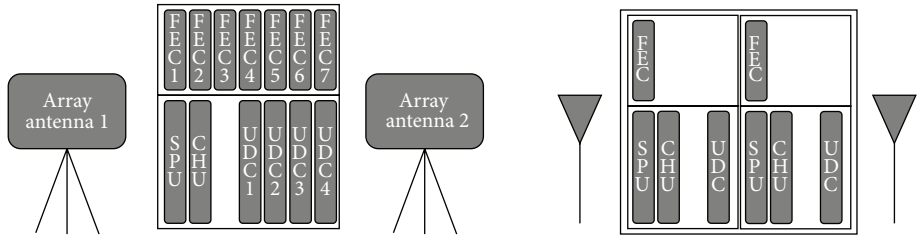

Figure 7: Overall system architecture of implemented MU-MIMO test-bed.

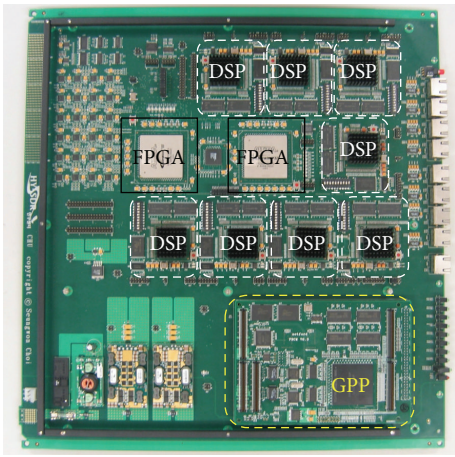

Figure 8: Implemented CHU.

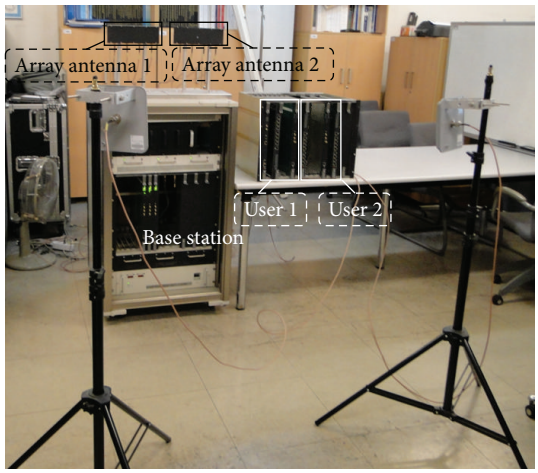

Figure 9: Implemented MU-MIMO test-bed.

each antenna for RX and TX calibration. The phase between the calibration antenna and each of the array antennas is measured in advance.

2.2.5. Total System Bed. Figure 7 illustrates the overall system architecture of the MU-MIMO test-bed that adopts ZF-based precoding combined with beamforming.

As shown in Figure 7, the RF signal is processed in the Front-End Unit (FEU), while the System Processing Unit (SPU) and Channel Card Unit (CHU) control and process the received signals, respectively. The user consists of an FEU, SPU, CHU, and UDC.

Figure 8 illustrates the CHU, which consists of a GPP (MPC8280), eight DSPs (TMS320C6416T), and two FPGAs (Altera Stratix II). In fact, the CHU performs the modem functionality of WiMAX. Therefore, the proposed algorithm is implemented in the channel card unit.

The allocation of the functions on the devices and the complexity of each function are described in the next section.

Figure 9 shows a photo of the implemented MU-MIMO test-bed.

3. Results and Discussion

This section provides a performance analysis of the proposed technique, including the precoder and beamformer.

3.1. Complexity. The complexity of the signal processing units is shown in Table 2.

Table 2 shows the complexity of the signal processing unit. It also shows how each of the functions has been allocated on the hardware devices of the implemented system. As shown in Table 2, the computational burden required for the functions of the proposed beamforming method, that is, the weight calculation (implemented for uplink at DSP-1) and weight multiplication (implemented for downlink at FPGA), takes only about 14% of the total complexity. Note that, as shown in Table 2, both weight calculation and weight multiplication take about 377 K gates while the required number of gates for the entire uplink and downlink computations is about (1587 + 1099) K gates.

3.2. Computer Simulation. We show the performance of the OLB-based beamformer through computer simulations. In this paper, we used "MATLAB" provided by "MathWorks" in order to implement the simulation [**?**]. It supports various functions of mathematics and tools for drawing graphs which are needed to implement the simulation.

The experimental environment consists of a single base station and two mobile terminals. The base station is composed of an MU-MIMO system consisting of two MIMO antenna elements, each of which is a three-element beamforming array, while each mobile terminal is equipped with a single antenna element. We assumed that the received power of each terminal is the same. We also assumed that the signal is propagated along the line of sight path. We generated

Table 2: Complexity of signal processing unit (all the digital signal processing is performed with 12 bits).

	Device	Functions	Complexity (K gates)
Uplink	FPGA	Ranging code Correlator	21.9
		FFT	338.2
		CP removal	8.3
		Timing synchronization	597.9
		Frequency synchronization	614.3
	DSP-1	Delay estimation	—
		Ranging code detection	—
		Weight calculation	—
	DSP-2	Channel estimation	—
		MIMO detection	—
	DSP-3	Demodulation	—
		FEC decoding	—
		Deinterleaving	
Total logic gates			1580.6
Downlink	FPGA	Weight multiplication	376.8
		IFFT	638.2
		Permutation	58.9
		CP addition	11.4
		Preamble	14.2
	DSP-1	Calibration	—
	DSP-2	MIMO encoding	—
	DSP-3	Modulation	—
		Concatenation	—
	DSP-4	Randomization	—
	DSP-5	FEC	—
		Interleaving	—
Total logic gates			1099.5

Table 3: Parameters for OLB-based beamformer simulation.

Parameters	Value
DOA	$0^\circ, 60^\circ$
E_b/N_o	5 dB
f in (3)	0.99
μ in (5)	0.01

the OLB-based beamformer in accordance with equations in Table 2. Simulation parameters are presented in Table 3.

Figure 10 illustrates the beam pattern provided by each of the three-element arrays at the base station.

As shown in Figure 10, each array provides a beam pattern with a gain of 2 for the DOA of each user, that is, 0° and 60°. From Table 3, we assumed that the two users are located at 0° and 60°. The error in the main lobe directions occurs because there are three antenna elements at each array, while there

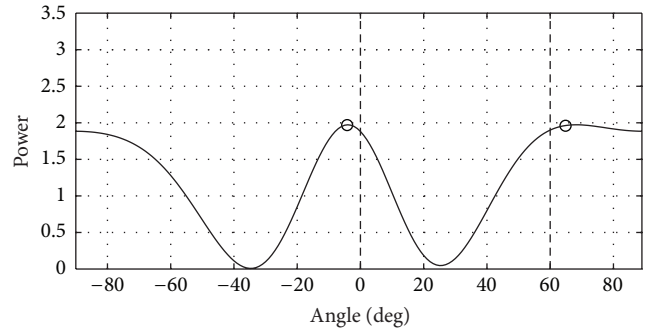

Figure 10: Beam pattern provided by a three-element array (two users located at 0° and 60°).

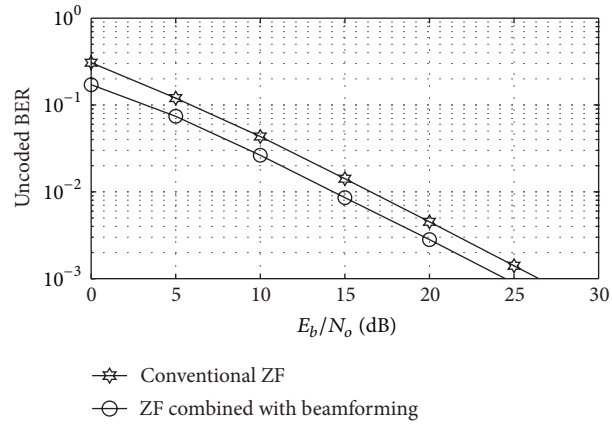

Figure 11: BER of MU-MIMO system with conventional ZF only and ZF with beamforming.

are two users to be supported. In order to provide a high-resolution beam pattern, the number of antenna elements at each array should be increased. However, the number of antenna elements at each array is restricted because each array must be a single element for the overall MIMO system.

Figure 11 illustrates the performance comparison in terms of the uncoded BER between two MU-MIMO systems which employ conventional ZF [**?**] only, which removes the MAI by using the inverse of channel matrix as its precoder, and ZF with beamforming, respectively.

From Figure 11, we can observe that the performance of the proposed method, which employs ZF-based precoding and OLB-based beamforming, far outperforms the conventional precoding-only MU-MIMO system. When the BER is 0.1%, for example, the proposed system improves the BER by about 2.4 dB due to the beamforming gain, which is shown in Figure 10. Furthermore, the proposed method outperforms the conventional ZF even further when the SNR becomes lower, because the proposed technique reduces the channel estimation error more effectively by exploiting the beamforming gain.

3.3. Measured FER. This section demonstrates the Frame Error Rate (FER) performance of the implemented system. Figure 12 illustrates the FER performance of our simulator

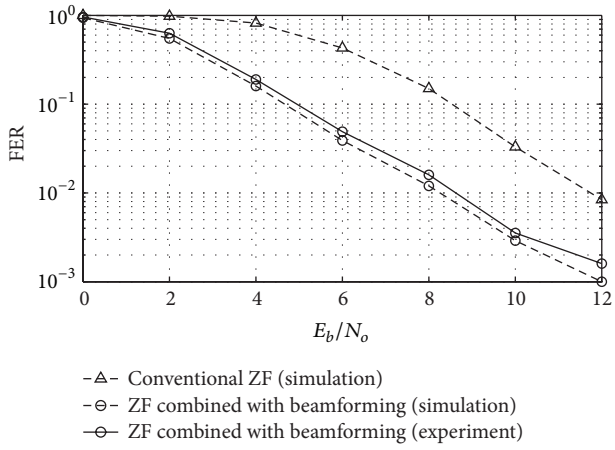

Figure 12: Measured FER performance.

in comparison with the measured FER obtained from the implemented system. The system parameters are defined in Table 1.

From Figure 12, we can compare the FER performance of the proposed system, that is, ZF + beamforming, and the conventional MU-MIMO system, that is, without beamforming. The proposed system outperforms the conventional system by about 1.7 dB when the FER is 1%. It can also be verified that the measured FER performance coincides very well with the simulation result.

4. Conclusion

In this paper, we proposed the ZF method combined with beamforming. The proposed technique was implemented for experimental tests of WiMAX waveforms. The experimental environment includes a single base station and two users, while the base station employs the proposed technique of ZF-based precoding (for two MIMO elements) and OLB-based beamforming (for three-element beamforming for each of the two MIMO elements), while each user is equipped with a single antenna.

We demonstrated that the proposed algorithm provides nearly twice the throughput compared to the Single-Input Single-Output (SISO) system, as well as twice the power gain compared to the conventional MU-MIMO system with precoding only. We also verified the feasibility of the proposed precoding method for real-time processing of a WiMAX base station system. The proposed method seems to be a good solution for increasing the throughput of a given frequency band.

Acknowledgment

This work was supported by the ICT Standardization program of The Ministry of Knowledge Economy (MKE).

References

[1] A. Goldsmith, S. A. Jafar, N. Jindal, and S. Vishwanath, "Capacity limits of MIMO channels," *IEEE Journal on Selected Areas in Communications*, vol. 21, no. 5, pp. 684–702, 2003.

[2] D. Gesbert, M. Kountouris, R. W. Heath, C. B. Chae, and T. Sälzer, "Shifting the MIMO Paradigm," *IEEE Signal Processing Magazine*, vol. 24, no. 5, pp. 36–46, 2007.

[3] S. Choi, "A novel adaptive beamforming algorithm for a smart antenna system in a cdma mobile communication environment," *IEEE Transactions on Vehicular Technology*, vol. 49, no. 5, pp. 1793–1806, 2000.

[4] R. Mudumbai, D. R. Brown, U. Madhow, and H. V. Poor, "Distributed transmit beamforming: challenges and recent progress," *IEEE Communications Magazine*, vol. 47, no. 2, pp. 102–110, 2009.

[5] T. Haustein, C. Von Helmolt, E. Jorswieck, V. Jungnickel, and V. Pohl, "Performance of MIMO systems with channel inversion," in *Proceedings of the IEEE 55th Vehicular Technology Conference (VTC '2002)*, pp. 35–39, Spring, May 2002.

[6] IEEE P802.16e/D12, "Air interface for fixed and mobile broadband wireless access systems," in *IEEE Standard for Local and Metropolitan Area Networks*, part 16, IEEE, 2005.

[7] W. C. Lee, S. Choi, and J. M. Kim, "Essential considerations in implementing the smart antenna system for downlink beamforming," *Wireless Personal Communications*, vol. 35, no. 3, pp. 227–240, 2005.

[8] The mathworks, http://www.mathworks.com.

[9] C. B. Peel, B. M. Hochwald, and A. L. Swindlehurst, "A vector-perturbation technique for near-capacity multiantenna multiuser communication—Part I: channel inversion and regularization," *IEEE Transactions on Communications*, vol. 53, no. 1, pp. 195–202, 2005.

Hindawi Publishing Corporation
International Journal of Antennas and Propagation
Volume 2013, Article ID 528950, 9 pages
http://dx.doi.org/10.1155/2013/528950

Research Article

An Antenna Measurement System Based on Optical Feeding

Ryohei Hosono and Ning Guan

Optics and Electronics Laboratory, Fujikura Ltd., Sakura-shi 285-8550, Japan

Correspondence should be addressed to Ryohei Hosono; ryohei.hosono@jp.fujikura.com

Received 30 January 2013; Revised 29 March 2013; Accepted 31 March 2013

Academic Editor: Sara Burgos

A radiation measurement system by using optical feeding is proposed. The system replaces conventional electrical feeding to antennas by the optical feeding which is composed of an electrical/optical (E/O) converter, a graded-index (GI) optical fiber, and an optical/electrical (O/E) converter. The GI fiber is used so as the O/E converter becomes very compact by using a simple means of coupling between the fiber and the photo-diode in the converter. A vertical surface emitting laser (VCSEL) is used in the E/O converter to make the system available till 6 GHz. This combination also makes the system cost-effective. The validity as well as the advantage of the system is demonstrated by measuring an ultra-wideband (UWB) antenna both by the optical and electrical feeding systems and comparing with a calculated result. Ripples in radiation pattern due to the electrical feeding are successfully suppressed by the optical feeding. For example, in a radiation measurement on the azimuth plane at 3 GHz, ripple amplitude of 1.0 dB that appeared in the electrical feeding is reduced to 0.3 dB. In addition, a circularly polarized (CP) antenna is successfully measured by the proposed system to show that the system is available not only for amplitude but also phase measurements.

1. Introduction

Recently, as wireless mobile devices become smaller and smaller, antennas used in the devices are required to be very compact. It becomes even more important to measure precisely such compact antennas for antenna development. However, an antenna must be fed when the antenna is to be measured and the feeding is generally made electrically by microstrip lines, coaxial cables, and so forth. Electrical feeding lines disturb the radiation of the antenna under test (AUT) due to their metallic bodies. In addition, there causes unbalanced currents on the feeding lines to excite unwanted radiation which interferes the original one. The influence becomes significant when the AUT is small. As a consequence, ripples or unwanted peaks appear in the radiation patterns of the AUT. Furthermore, the influence arises not only on the measurement of amplitude but also phase which is a very important parameter in some antennas such as a circularly polarized (CP) antenna.

Using smaller feeding lines and baluns is conventional technique to reduce the influence of feeding lines on antenna measurement. Ferrite chokes and cylindrical conductive caps set on coaxial cables are known to work as balun [1–6]. However, the balun or chokes are only available at narrow and low frequency band, for example, sleeve balun is generally designed near quarter wave length so that the bandwidth is limited [1–5]. On the other hand, replacing electrical feeding by optical one is an effective solution to this problem. For example, optical feeding is introduced to shut off unbalanced currents on electrical feeding lines and avoid influence on radiation of antenna under test (AUT), for wireless handheld terminals [7–9], a log-periodic antenna [10], a biconical antenna [11], a monopole antenna and a log-periodic antenna [12], a planar inverted F antenna (PIFA) [13], and a dipole antenna [14]. Both amplitude and phase of radiation are also evaluated by optical fiber measurement systems [8–10]. In these examples, a edge-emitting lasers such as distributed feed-back (DFB) laser and a single-mode fibers have been implemented. Although the implementations provide wide band measurement, they need external modulators, precise alignment, and relatively large spaces [11, 14]. This makes the system expensive and limits the system miniaturization.

In this paper, we propose a measurement system for radiation patterns by using optical feeding. We use direct

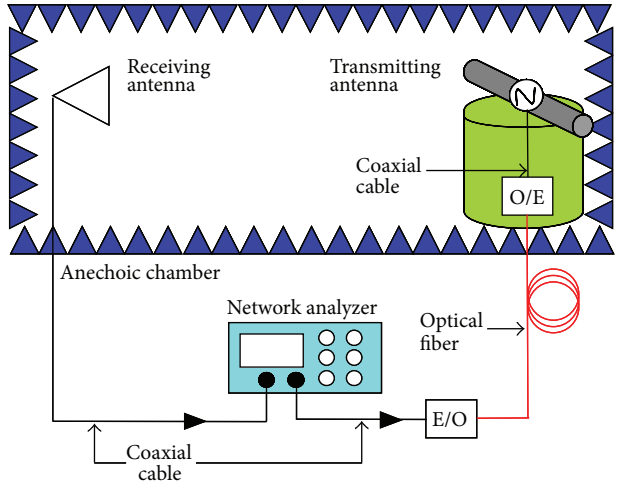

FIGURE 1: Measurement setup of optical feeding.

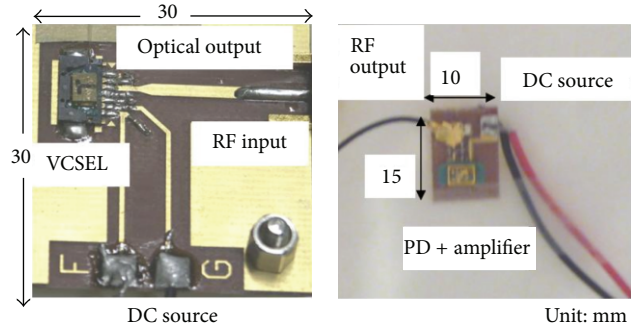

FIGURE 2: Details of E/O and O/E converters.

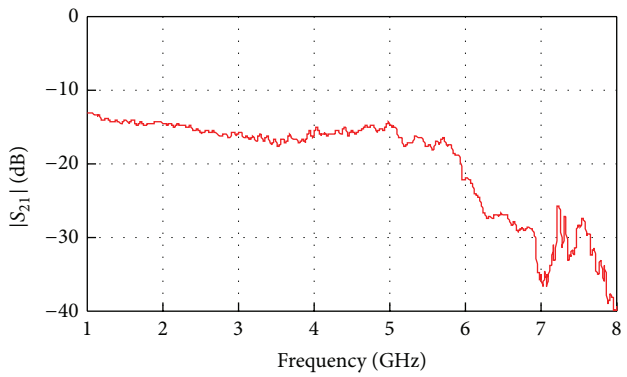

FIGURE 3: Frequency characteristics of transmission for directly connected E/O and O/E converters.

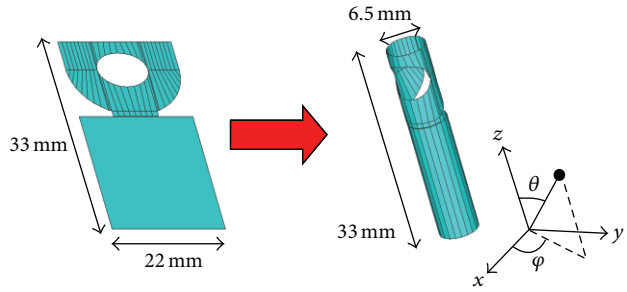

FIGURE 4: Rolled UWB antenna for measurement.

modulation on a vertical surface emitting laser (VCSEL) and a graded-index (GI) optical fiber as transmission line so as we can realize a compact and cost-effective system and extend the measuring frequency range up to 6 GHz easily. The VCSEL allows high speed modulation and low driving current thanks to its surface emission structure [15, 16]. Its emission profile matches very well with a multimode fiber so that cost-effective and compact butt-joint is available. In addition, the wafer-level testing makes the VCSEL chips cost-effective themselves.

To show the validity and the advantage of the system, a small antenna operating at an ultra-wideband (UWB) is measured by this system. We investigate the influence of the feeding line by changing its wiring with calculated and measured results. The measured results are compared with those measured by a conventional electrical feeding and those obtained

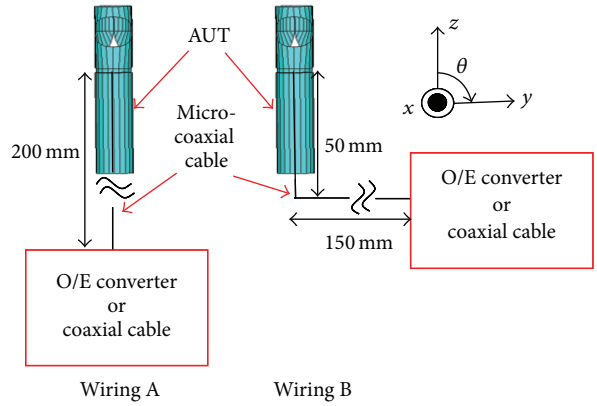

Figure 5: Antennas with two different wirings of micro-coaxial cable.

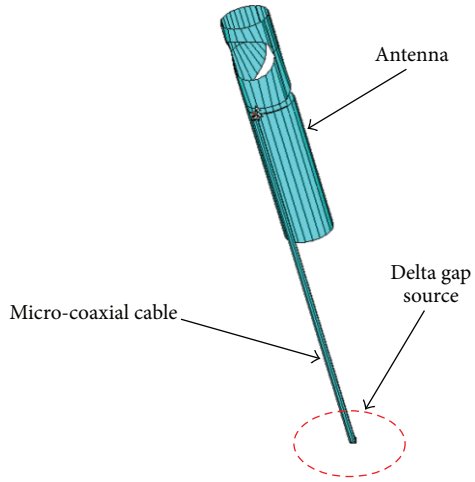

Figure 6: Antenna calculation model.

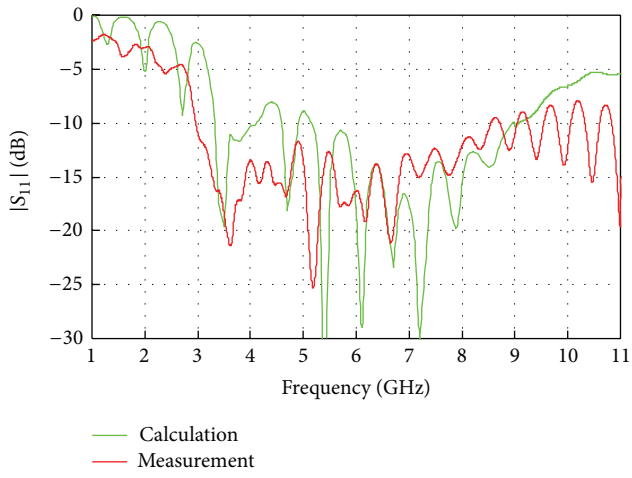

Figure 7: Input characteristics for rolled UWB antenna.

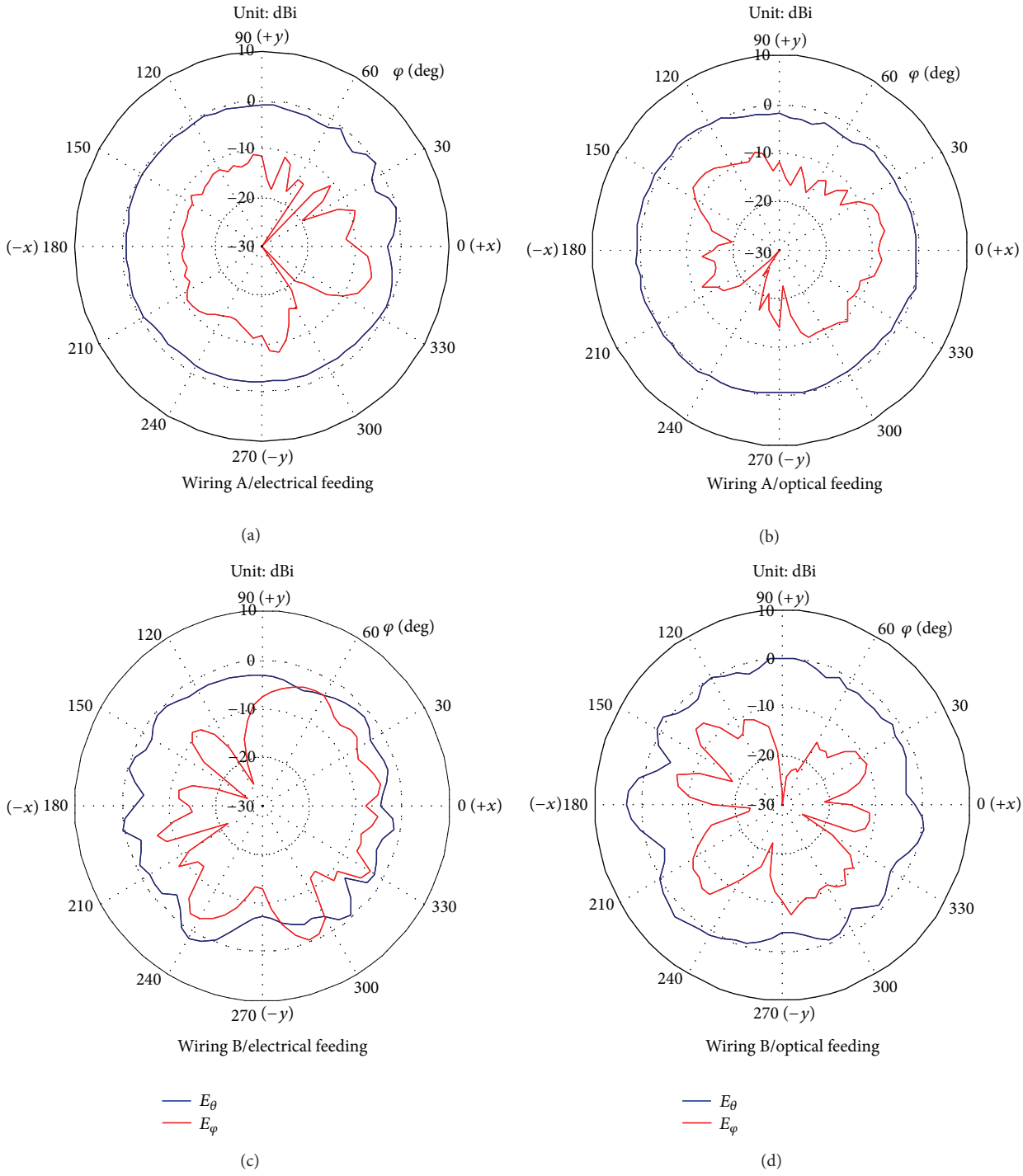

Figure 8: Measured radiation patterns in xy-plane at 5 GHz for optical and electrical feedings.

theoretically. A CP patch antenna for the global positioning system (GPS) application is also measured for investigating the accuracy on phase measurement. A comparison between the optical and electrical measurements and the calculation is also carried out. It is demonstrated that the proposed system can be used for precise measurement for not only amplitude but also phase characteristics of small antennas.

2. Measurement Setup

The proposed measurement setup is schematically shown in Figure 1. It replaces conventional electrical feeding line by electrical/optical (E/O) and optical/electrical (O/E) converters with a GI-fiber. The replacement is done only for the coaxial cable connecting to transmitting antenna. Details of

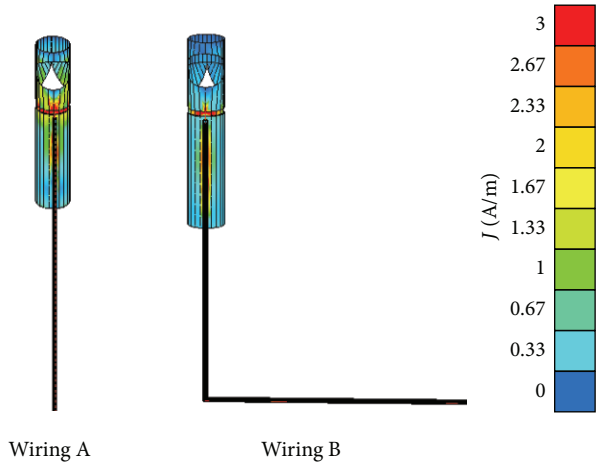

Figure 9: Current distributions on antenna and coaxial cable.

the E/O and O/E converters are shown in Figure 2. The E/O converter is composed of a VCSEL which is directly modulated by RF signal. A dynamic resistance of the VCSEL has a characteristic impedance of 35 Ohm at operating point so that there is slight impedance mismatch. The E/O converter has a size of $30 \times 30 \times 5\,\text{mm}^3$ which does not include the size of DC supply such as battery. The O/E converter is composed of a GaAs PIN photo-diode (PD) and an amplifier where the peak-to-peak output voltage is 250 mV. The PD is spatially coupled with the optical fiber by resin which acts as mirror so as the O/E converter including a tiny RF connector has a size of $10 \times 15 \times 5\,\text{mm}^3$ which does not include the size of DC supply. These E/O and O/E converters give much more compact and simpler configuration than previous reports in [10–14].

A micro-coaxial cable which has the characteristic impedance of 50 Ohm is used to connect the O/E converter to the AUT. The length of the coaxial cable is optimized to minimize metallic influence of the O/E converter and the radiation from the unbalanced currents on the coaxial cable. Figure 3 shows frequency characteristics of the transmission for directly connected O/E and E/O converters where the input power from a network analyzer is 0 dBm. The curve keeps flatness up to 6 GHz and shows a gradual decrease for higher frequencies. Loss emerged in the output power at whole frequencies is due to the conversion loss in the E/O and O/E converters.

3. Experimental Results

3.1. Amplitude Measurement. In order to verify the validity of the proposed system, an UWB antenna shown in Figure 4 is measured, where the antenna is rolled from a flexible flat film so as it has omni radiation patterns in its azimuth plane even at high frequencies [17]. The micro-coaxial cable with a diameter of 0.8 mm and a length of 200 mm is used to connect the antenna and the O/E converter. This long cable is used because we can separate the O/E converter from the antenna and try to investigate the influence of the cable by changing its wiring, as shown in Figure 5. Wiring A sets the coaxial cable parallel to the antenna axis while Wiring B sets a part of the coaxial cable perpendicular to the antenna axis. The antenna is also measured by the electrical feeding where micro-coaxial cable is used. Relative gain measurement [18] is used so that there is no influence from receiving antenna.

To theoretically analyze the antenna, an antenna model is constructed by using the commercial available software WIPL-D as shown in Figure 6, where the feeding cable fed by a delta-gap source [19] is taken into account.

Figure 7 compares the input characteristics of the antenna for the measurement and calculation. Reasonable agreement is obtained between them.

Figure 8 shows the measured radiation patterns in xy-plane at 5 GHz for the antenna with two different wirings shown in Figure 5, for the optical and electrical feedings. In Wiring A, omni-directional radiation patterns are observed in E_θ both for the electrical and optical feedings but fewer ripples occur in the latter one. The radiation of E_φ remains low level compared with that of E_θ for both the feedings. In Wiring B, The level of the radiation of E_φ reaches to 0 dBi and becomes compared to that of E_θ in the electrical feeding. In contrast, the level of the radiation of E_φ keeps relatively low with the maximum value less than −5 dBi, in the optical one. This phenomenon can be explained as follows: unbalanced currents existing on the coaxial cable perpendicular to the antenna axis couple strongly with the radiation of the antenna in the electrical feeding but they are successfully suppressed in the optical one.

Figure 9 shows the calculated current distributions on the antenna and coaxial cable at 5 GHz. It is demonstrated that currents flow on the antenna itself and through the outer conductor of the cable. It suggests that the unbalanced currents flow not only along the direction parallel to the antenna axis but also currents flow along the direction perpendicular to the antenna axis. Many ripples appear in the case of Wiring B because the radiation due to the unbalanced currents couples strongly with that from the antenna itself. Figure 10 shows the radiation patterns for total field at 3 GHz for both the optical and electrical feedings where Wiring A is applied. The calculated radiation patterns are also shown in Figure 10 where the micro-coaxial cable is modeled. The radiation patterns obtained by the optical feeding are better fit to the calculated ones. Null points can be recognized clearly and ripples appearing in the patterns of the electrical feeding are almost suppressed for the optical feeding. For example, ripple amplitude, which is defined as a RMS difference between the measured gain and its 10-point-centered moving average, is 1.0 dB in the electrical feeding and 0.3 dB in the optical one, for the measurement in xy-plane. Measured radiation patterns in xy-plane of the electrical and optical feedings at 3, 4 and 5 GHz are shown in Figure 11. It is also shown that the optical feeding can effectively reduce ripples and obtain omni-directional characteristics in a wide band.

3.2. Phase Measurement. Phase characteristics are also measured for a CP patch antenna shown in Figure 12.

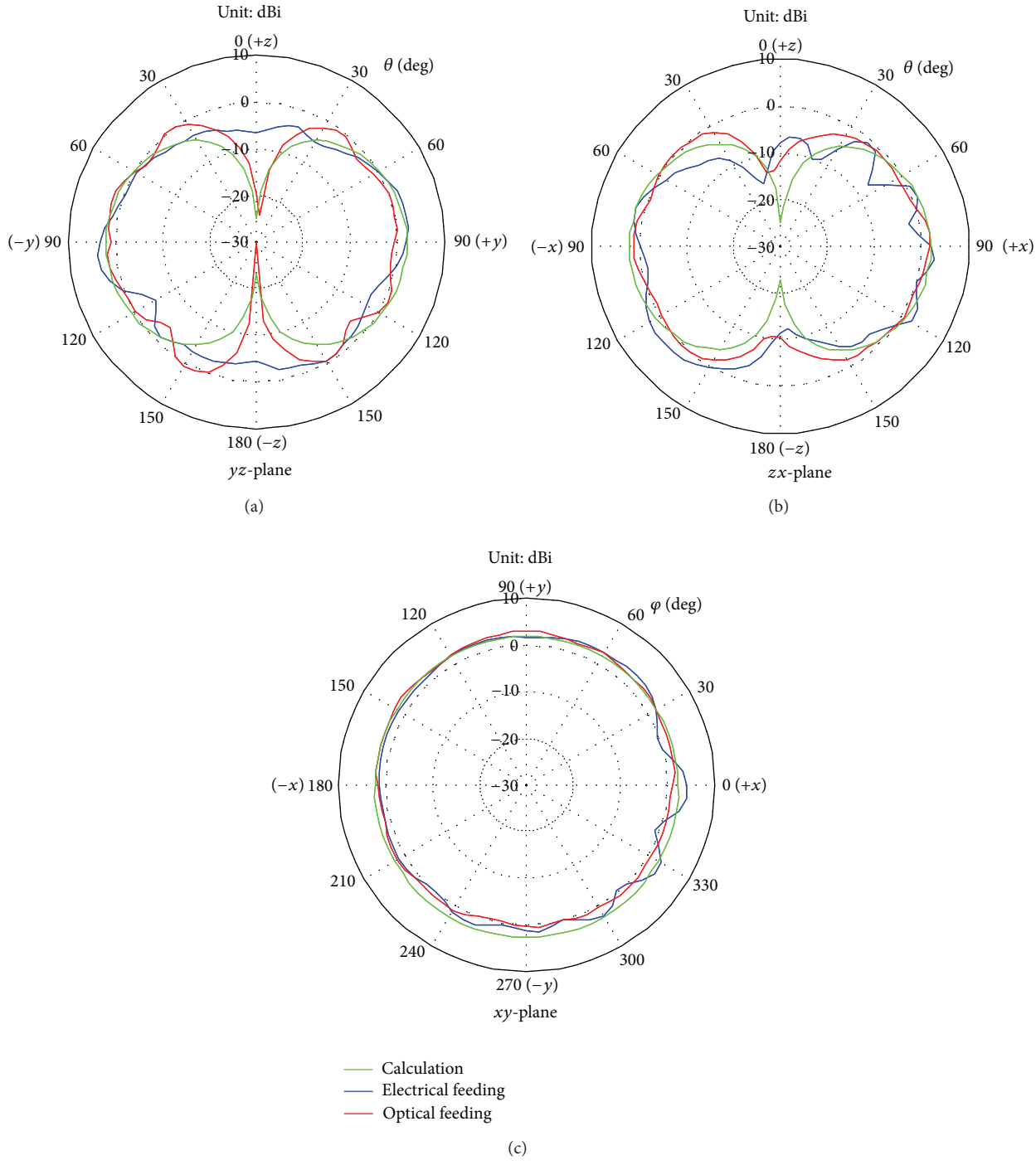

FIGURE 10: Measured and calculated radiation patterns for total field at 3 GHz.

The dimensions of SMA connector are precisely considered in this investigation. The antenna consists of a patch where two corners of the patch are truncated and the feeding point is shifted from the center to generate a right-handed circularly polarized (RHCP) electric field on a dielectric substrate backed by ground plane [20, 21]. This antenna is designed for the frequency range of the GPS applications from 1573.42 to 1577.42 MHz. The CP patch antenna is evaluated by using the phase-amplitude method [22, 23] in this investigation.

Figure 13 shows the calculated and measured input characteristics for the CP patch antenna. Reasonable agreement is obtained between the calculated and measured results. A difference less than 1.6 dB is observed from 1573 to 1577 MHz. It is shown that the antenna has a sufficient bandwidth at the GPS band.

Figure 14 shows the frequency characteristics of the axial ratio defined as the ratio between the amplitudes of the major and minor polarizations of the antenna at the direction of

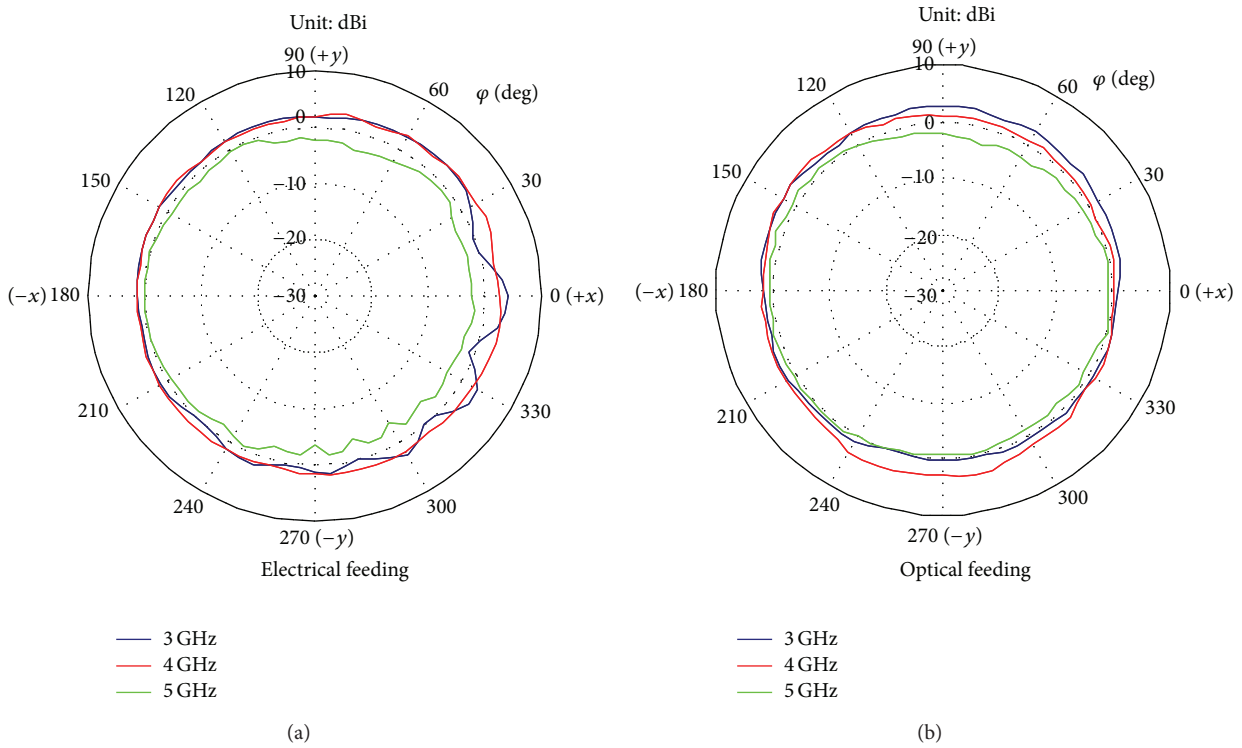

Figure 11: Measured radiation patterns for total field at xy-plane at several frequencies for Wirng A.

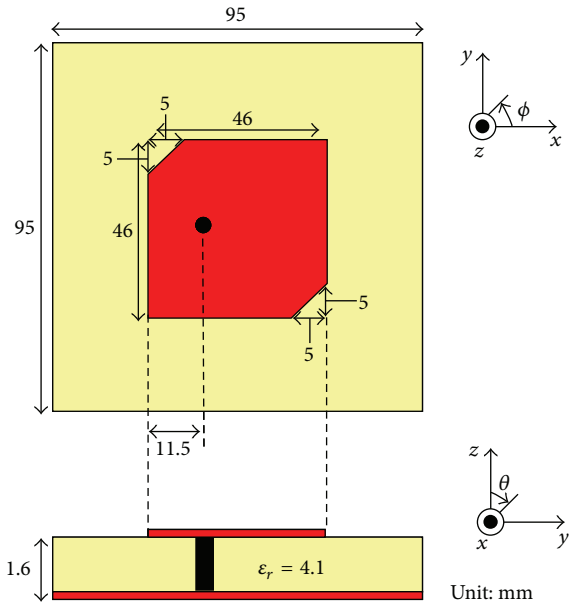

Figure 12: Geometry of CP patch antenna.

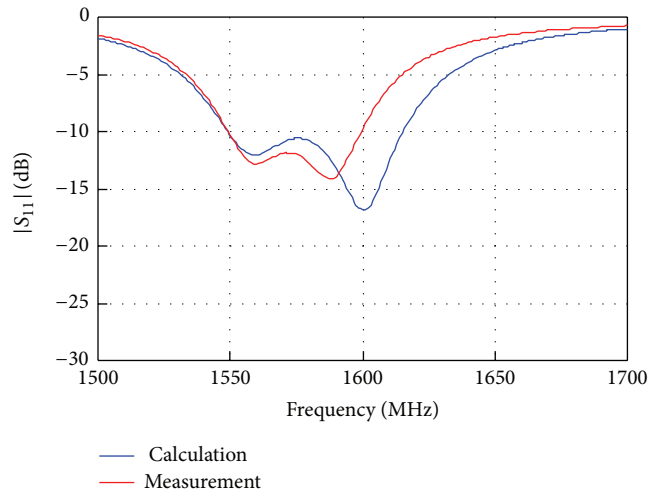

Figure 13: Input characteristics of CP patch antenna.

$\theta = 0$ and $\varphi = 0$ for both the measurements of the electrical and optical feedings as well as the calculation. Reasonable agreements are also obtained between calculated and measured results especially in those of optical feeding.

Figures 15 and 16 show the frequency characteristics of the electric field amplitude ratio of x to y polarizations and the phase difference between x and y polarizations of electric fields at the point of $\theta = 0$ and $\varphi = 0$, respectively. Reasonable agreements are also obtained between calculated and measured results.

4. Conclusion

We have developed a compact and cost-effective radiation measurement system by using the optical feeding. The system

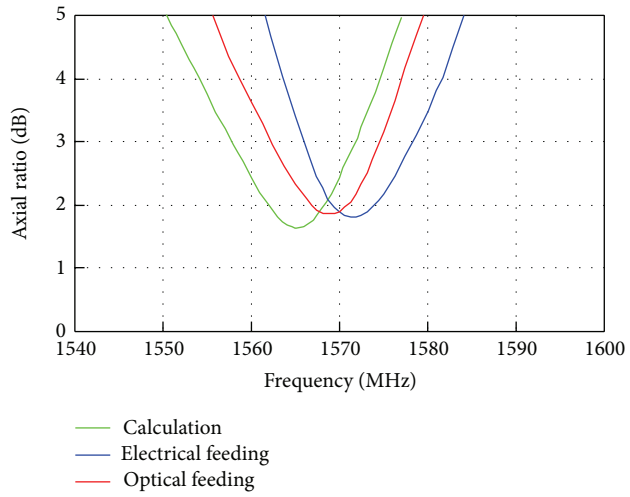

Figure 14: Frequency characteristics of axial ratio.

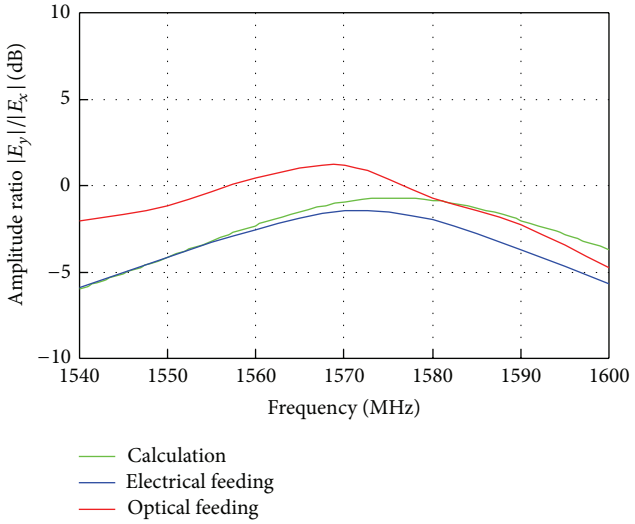

Figure 15: Amplitude ratio for CP patch antenna.

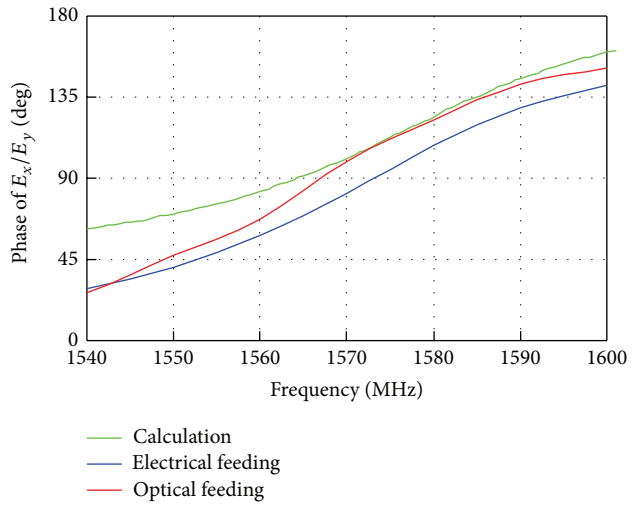

Figure 16: Phase difference for CP patch antenna.

is composed of a VCSEL, a PD and a GI-fiber and provides available measurement up to 6 GHz. It has a compact O/E converter to feed AUT by a micro-coaxial cable. It is demonstrated that the system successfully suppresses unbalanced currents on the feeding line and can be used for precise measurement not only for amplitude but also phase measurements.

References

[1] C. Icheln, J. Ollikainen, and P. Vainikainen, "Reducing the influence of feed cables on small antenna measurements," *Electronics Letters*, vol. 35, no. 15, pp. 1212–1214, 1999.

[2] C. Icheln and P. Vainikainen, "Dual-frequency balun to decrease influence of RF feed cables in small antenna measurements," *Electronics Letters*, vol. 36, no. 21, pp. 1760–1761, 2000.

[3] S. A. Saario, J. W. Lu, and D. V. Thiel, "Full-wave analysis of choking characteristics of sleeve balun on coaxial cables," *Electronics Letters*, vol. 38, no. 7, pp. 304–305, 2002.

[4] P. J. Massey and K. R. Boyle, "Controlling the effects of feed cable in small antenna measurements," in *Proceedings of the 12th International Conference Antennas and Propagat*, vol. 2, pp. 561–564, Exeter, UK, March 2003.

[5] C. Icheln, J. Krogerus, and P. Vainikainen, "Use of balun chokes in small-antenna radiation measurements," *IEEE Transactions on Instrumentation and Measurement*, vol. 53, no. 2, pp. 498–506, 2004.

[6] S. Saario, D. V. Thiel, J. W. Lu, and S. G. O. Keefe, "An assessment of cable radiation effects on mobile communications antenna measurements," in *Proceedings of the IEEE Antennas and Propagation Society International Symposium, Digest*, vol. 1, pp. 550–553, Montreal, Canada, July 1997.

[7] W. A. T. Kotterman, G. F. Pedersen, K. Olesen, and P. Eggers, "Cable-less measurement set-up for wireless handheld terminals," in *Proceedings of the 12th International Symposium on Personal, Indoor and Mobile Radio Communications (PIMRC '01)*, pp. B112–B116, San Diego, Calif, USA, October 2001.

[8] S. Amari, A. Yamamoto, H. Iwai, Y. Koyanagi, and K. Ogawa, "Complex radiation pattern measurement using a optical-fibre cable applicable to a handset adaptive array," in *Proceedings of the International Symposium Antennas and Propagation (ISAP '07)*, pp. 73–76, Niigata, Japan, August 2007.

[9] T. Fukazawa, K. Shimomura, and M. Otsuka, "Accurate measurement method for characteristics of an antenna on a portable telephone," *IEICE Transactions on Communications*, vol. 86, no. 9, pp. 1895–1905.

[10] S. Kurokawa, M. Hirose, and K. Komiyama, "Optical fiber link 1-pass 2-port antenna measurement system," in *Proceedings of the 67th ARFTG Microwave Measurements Conference*, pp. 246–250, San Diego, Calif, USA, June 2006.

[11] R. Lao, W. Liang, Y. S. Chen, and J. H. Tarng, "The use of electro-optical link to reduce the influence of RF cables in antenna measurement," in *Proceedings of the IEEE International Symposium on Microwave, Antenna, Propagation and EMC Technologies for Wireless Communications (MAPE '05)*, vol. 1, pp. 427–430, Beijing, China, August 2005.

[12] I. K. Cho, J. I. Mun, S. M. Kim, and J. H. Yun, "Optical fiber link system for the antenna measurement," in *International Conference on Photonics in Switching (PS '09)*, pp. 1–2, Pisa, Italy, February 2009.

[13] B. Yanakiev, J. O. Nielsen, M. Christensen, and G. F. Pedersen, "Small device for short-range antenna measurements using optics," *IEEE Transactions on Antennas and Propagation*, vol. 53, no. 6, pp. 148–152, 2011.

[14] J. C. Wyss and S. T. Sheeran, "A practical optical modulator and link for antennas," *Journal of Lightwave Technology*, vol. 3, no. 2, pp. 316–321, 1985.

[15] F. Koyama, "Recent advances of VCSEL photonics," *Journal of Lightwave Technology*, vol. 24, no. 12, pp. 4502–4513, 2006.

[16] S. Md. Arefin and T. Mollick, "Analysis of vertical cavity serface emitting laser, resonant cavity enhanced photodetector & their integrated structure," *Engineering and Applied Sciences*, vol. 1, no. 3, pp. 97–104, 2013.

[17] N. Guan, H. Tayama, H. Furuya, D. Delaune, and K. Ito, "A deformed film UWB antenna," *IEICE Transaction on Communications*, vol. 93, no. 10, pp. 2531–2537, 2010.

[18] H. Arai, *Measurement of Mobile Antenna*, Artech House, 2001.

[19] R. F. Harrington, *Field Computation By Moment Methods*, IEEE Press, Piscataway, NJ, USA, 1993.

[20] K. L. Wong, *Compact and Broadband Microstrip Antennas*, John Wiley & Sons, New York, NY, USA, 2002.

[21] F. S. Chang, K. L. Wong, and T. W. Chiou, "Low-cost broadband circularly polarized patch antenna," *IEEE Transactions on Antennas and Propagation*, vol. 51, no. 10, pp. 3006–3009, 2003.

[22] C. T. Rodenbeck, K. Chang, and J. Aubin, "Automated pattern measurement for circularly-polarized antennas using the phase-amplitude method," *Microwave Journal*, vol. 47, no. 7, pp. 68–78, 2004.

[23] G. E. Evans, *Antenna Measurement Techniques*, Artech House, Boston, Mass, USA, 1990.

Hindawi Publishing Corporation
International Journal of Antennas and Propagation
Volume 2013, Article ID 956898, 6 pages
http://dx.doi.org/10.1155/2013/956898

Application Article

A Compact Printed Quadruple Band-Notched UWB Antenna

Xiaoyin Li, Lianshan Yan, Wei Pan, and Bin Luo

School of Information Science & Technology, Southwest Jiaotong University, Chengdu, Sichuan 610031, China

Correspondence should be addressed to Lianshan Yan; lsyan@home.swjtu.edu.cn

Received 10 December 2012; Accepted 18 February 2013

Academic Editor: Alfonso Muñoz-Acevedo

A novel compact coplanar waveguide- (CPW-) fed ultrawideband (UWB) printed planar volcano-smoke antenna (PVSA) with four band-notches for various wireless applications is proposed and demonstrated. The low-profile antenna consists of a C-shaped parasitic strip to generate a notched band at 8.01~8.55 GHz for the ITU band, two C-shaped slots, and an inverted U-shaped slot etched in the radiator patch to create three notched bands at 5.15~5.35 GHz, 5.75~5.85 GHz, and 7.25~7.75 GHz for filtering the WLAN and X-band satellite signals. Simulated and measured results both confirm that the proposed antenna has a broad bandwidth of 3.1~12 GHz with VSWR < 2 and good omnidirectional radiation patterns with four notched-bands.

1. Introduction

Ultrawideband (UWB) technology has received considerable attention due to its high speed data rates, low power consumption, resistant to severe multipath and jamming, and so on. The UWB antenna as a key part of UWB communication systems is also being investigated increasingly in recent years [1, 2]. Various types of UWB antennas with wide band and simple fabrication have developed. However, there are several existing frequency bands, that is, IEEE 802.11a (5.15–5.35 and 5.725–5.825 GHz), downlink of X-band satellite communication systems (7.25~7.75 GHz), and ITU band (8.01~8.5 GHz), which may cause mutual interference with UWB signals [2–5].

In order to avoid interferences with these existing frequency bands, one way is to add band-stop filters to UWB antennas, which may lead to high cost and large size to UWB transceivers. The emerging of the band-notched antenna makes it possible for integrating the filter into the antenna. There are many approaches demonstrated to create band-notches in UWB antennas [2–13]. Generally, the existing techniques widely used to achieve band-notch can be classified into the following two categories: adding and etching resonator units to the antenna [3, 6, 12]. The first method focuses on adding diverse parasitic elements on the antenna, such as strip near radiator patch in [3, 4] and split ring resonators (SRRs) near feed line in [5]. Another effective method is etching various slots in the antenna, such as arc-shaped slot [8, 9], U-shaped slot [10], square-shaped slot [11], and SRR-shaped slot [12]. By employing parasitic strips and etching slots at the same time [11, 14], multiple band-notched functions could be achieved. However, most of the examples can only provide two or three notched bands because of the space restrictions and coupling between band-notched structures; nevertheless, only limited ones can achieve four notched bands [3, 15].

In this paper, a modified planar volcano-smoke antenna (PVSA) is considered to cover the UWB range. The design parameters of the resonator units that affect the resonator frequency based on both of the parasitic elements method and etching slots method are discussed. Subsequently a four band-notched UWB antenna for filtering the WLAN, downlink of X-band satellite communication systems, and ITU band signals is proposed and demonstrated. Band-notch characteristics are achieved by embedding a C-shaped parasitic strip, two C-shaped slots, and a U-shaped slot on the patch. Details of designing the proposed antenna with simulations and measurements are carried out. The configuration of the proposed antenna is shown in Section 2. Both of the simulated and measured results including voltage-standing wave ratio (VSWR), radiation patterns, and peak gain are shown in Section 3. A conclusion will be drawn in Section 4.

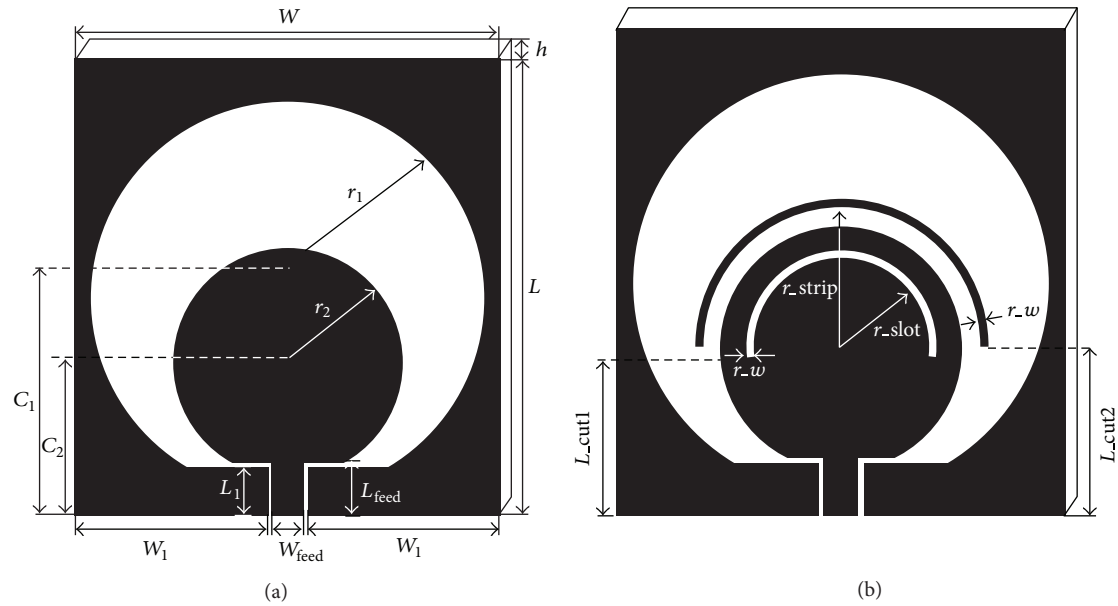

Figure 1: Structure of the antenna.

2. Antenna Design

The proposed quadruple band-notched antenna is based on a planar volcano-smoke antenna that covers the UWB frequency range, whose structure is shown in Figure 1(a) [4, 16, 17]. The based antenna uses FR4 substrate with the dimensions of $26 \times 28 \times 0.4\ \text{mm}^3$, relative permittivity $\varepsilon_r = 4.4$, and a loss tangent of 0.02. The antenna is fed by a CPW line which is designed for 50 Ω characteristic impedance with 1.8 mm feed line width (W_{feed}) and 0.2 mm ground gap. Through simulations with the software Ansoft High Frequency Structure Simulator (HFSS), the optimal dimensions of the designed PVSA are listed as follows: $W = 26$ mm, $L = 28$ mm, $h = 0.4$ mm, $r_1 = 12$ mm, $r_2 = 7$ mm, $C_1 = 13$ mm, $C_2 = 8$ mm, $W_{\text{feed}} = 1.8$ mm, $L_{\text{feed}} = 2$ mm, and $L_1 = 1.8$ mm. In order to eliminate interferences from WLAN, downlink of X-band satellite communication systems, and ITU band, antenna-filtering techniques by etching slots and employing parasitic strips on the PVSA are discussed.

To compare the frequency response characteristics of etching slots on the patch and adding parasitic elements, we investigate and simulate the two methods for creating band notched in the proposed UWB antenna, respectively. The structure of the two methods is shown in Figure 1(b), where the L_cut1 (L_cut2) means the distance between the end of the slot (strip) and the bottom edge of the substrate. Simulation results are shown in Figure 2. It is proved that the length of the slot (affected by the radius of the slot r-slot and the end position L_cut1) determines the resonant frequency, while the position of the slot (affected by md-slot that means the shift about the center of the slot) has relatively slight effect. The length of slots corresponds to half of the wavelength of the designed notch frequency, which can be used to estimate the notched frequency of the slots [8, 10, 11]. The length of the strip also determines the resonant frequency like the slot.

In theory, both the two methods can create any band-notch in the entire band of UWB. However, the size of the antenna and coupling of the band-notched structure make it difficult to create the band-notch in practical applications. For the proposed antenna, circle-like strip/slot aimed at reducing the strip/slot area. From Figure 2(a), it can be seen that the parasitic elements method can only create a band-notch with an upper limit of 8 GHz. As for higher notched band, when the length of the strip gets shorter, its rejection frequency goes higher but with a lower peak rejection ratio. Meanwhile, the shape of the parasitic strip might be too small to perform as a resonator. It also can be seen that the slot method cannot create a band-notch lower than 5 GHz from Figure 2(b), as the length of the slot cannot become longer because of the size restriction of the patch. From both methods, we propose a new antenna design to implement the requirements of any band-notches in the entire UWB band.

A four band-notches UWB antenna has been presented in [3] by feed-line with holes, which is not suitable for printable technology. Here, a novel CPW-fed UWB antenna with a parasitic strip and three slots is proposed, as shown in Figure 3. Slots with different shapes, such as rectangular, circular, and elliptical or any other shapes, can be arbitrarily etched on the patch to generate notched bands. However, a slot/strip with the same shape of the antenna patch can generate a stronger resonance than any other shape because the current distribution is concentrated at the edge of the patch. Meanwhile, the strips/slots with the same structures are useful for saving space [4, 5, 9, 17]. Therefore two C-shape, slots and one C-shape, strip are incorporated. It can be seen from Figure 2(d) that the position of the slot (means the shift of the center of the slot, indicated by md-slot) has little effect on the resonant frequency, but has effect on the bandwidth of the notched band. To obtain the narrow notched band, the slot S_2 is moved up 0.7 mm to decrease its bandwidth. With

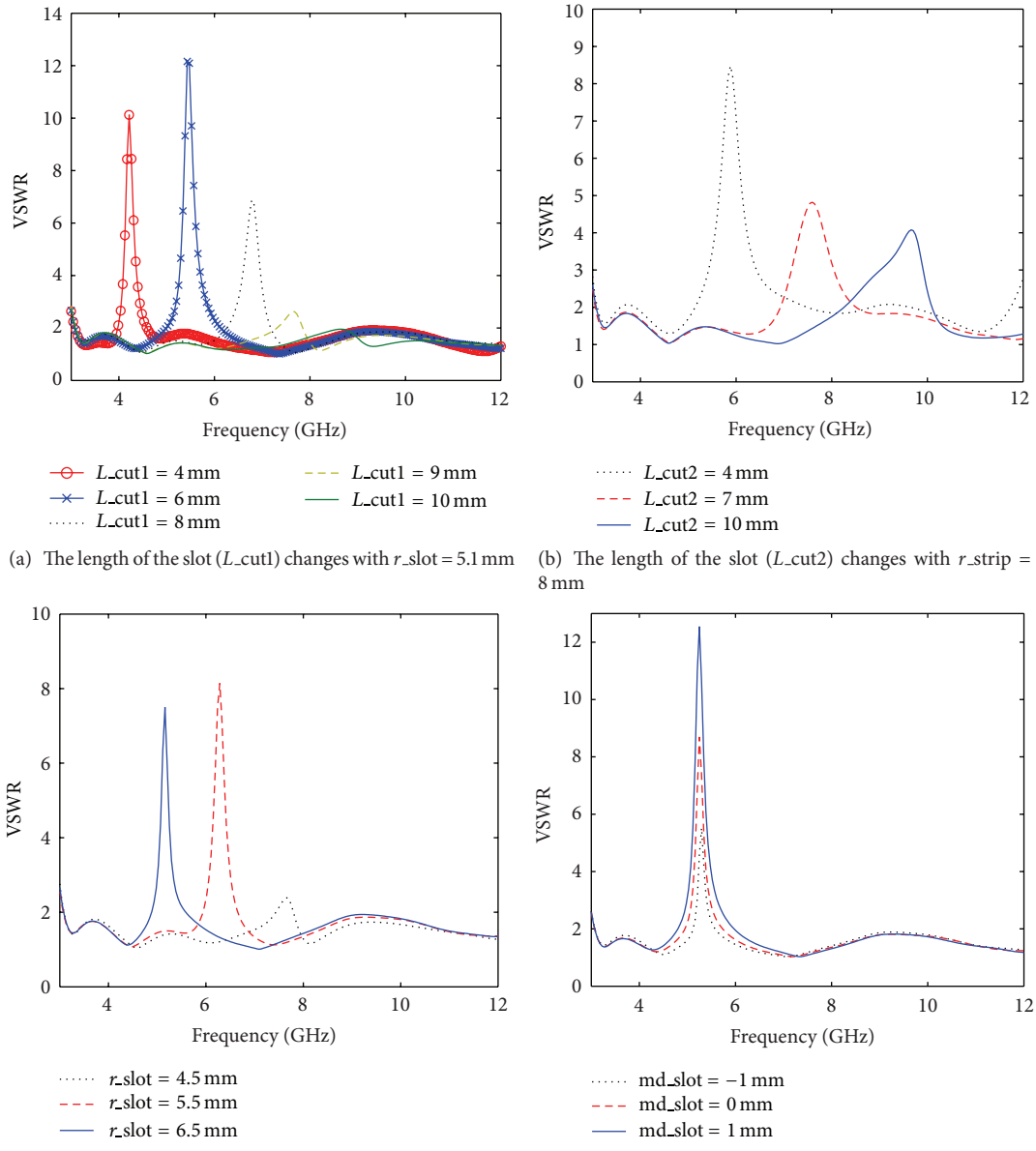

(a) The length of the slot (L_cut1) changes with r_slot = 5.1 mm

(b) The length of the slot (L_cut2) changes with r_strip = 8 mm

(c) The radius of the slot (r_slot) changes with L_cut = 8 mm

(d) The position of the slot (md_slot) changes with r_slot = 5.1 mm and L_cut = 5.7 mm

Figure 2: VSWR of the antenna with different lengths of slots and strips (C_1 = 13 mm, C_2 = 8 mm, and r_w = 0.5 mm).

the restriction of the patch size and the coupling between the nearby slots, a U-shape, slot instead of the C-shape, slot is further added for reducing the coupling with other slots. The optimized parameters of the antenna geometry are listed in Table 1. For convenience, the reference point is considered to be the top left corner.

Table 1: Optimized parameters of the quad band-notched antenna.

Parameters	L_cut	L_cut1	L_cut2	r_w	md_slot
Value (mm)	5.7	9.2	8	0.5	0.7
Parameters	r_slot1	r_slot2	r_strip	L_U	W_U
Value (mm)	6.5	5.1	8	6	4.6
Parameters	L_{feed}	W_{feed}	$L1$	$L2$	$W1$
Value (mm)	2	1.8	1.8	9.6	11.9

3. Results and Discussion

To verify the design concept, a prototype of the quad band-notched antenna is fabricated and measured. The photograph of the fabricated quad band-notched antenna is given in Figure 4. And Figure 5 shows the simulated and measured VSWR of the proposed antenna. The measurement is performed with an Agilent 8719A vector network analyzer. It can be observed that the measurement and simulation results agree with each other well. There is a little discrepancy

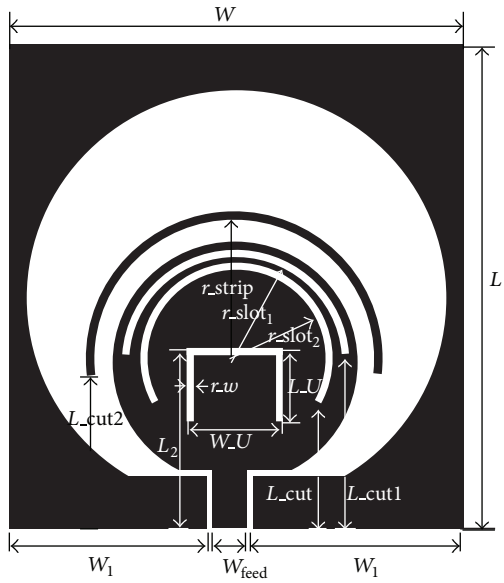

Figure 3: Schematics of the proposed quadruple band-notched UWB antenna.

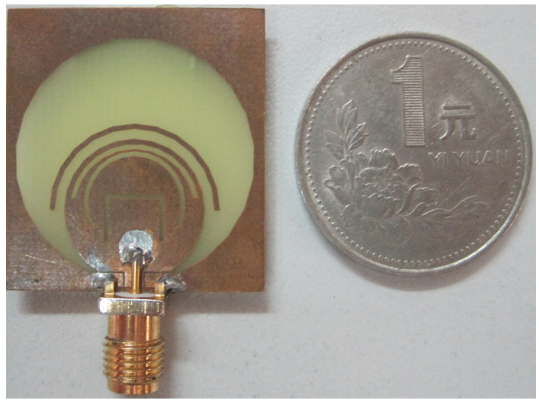

Figure 4: Photograph of the proposed quadruple band-notched UWB antenna.

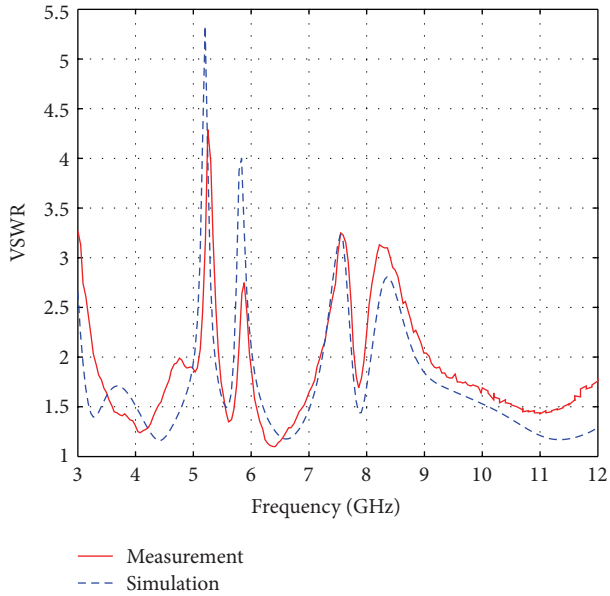

Figure 5: Simulated and measured VSWR of the quadruple band-notched UWB antenna.

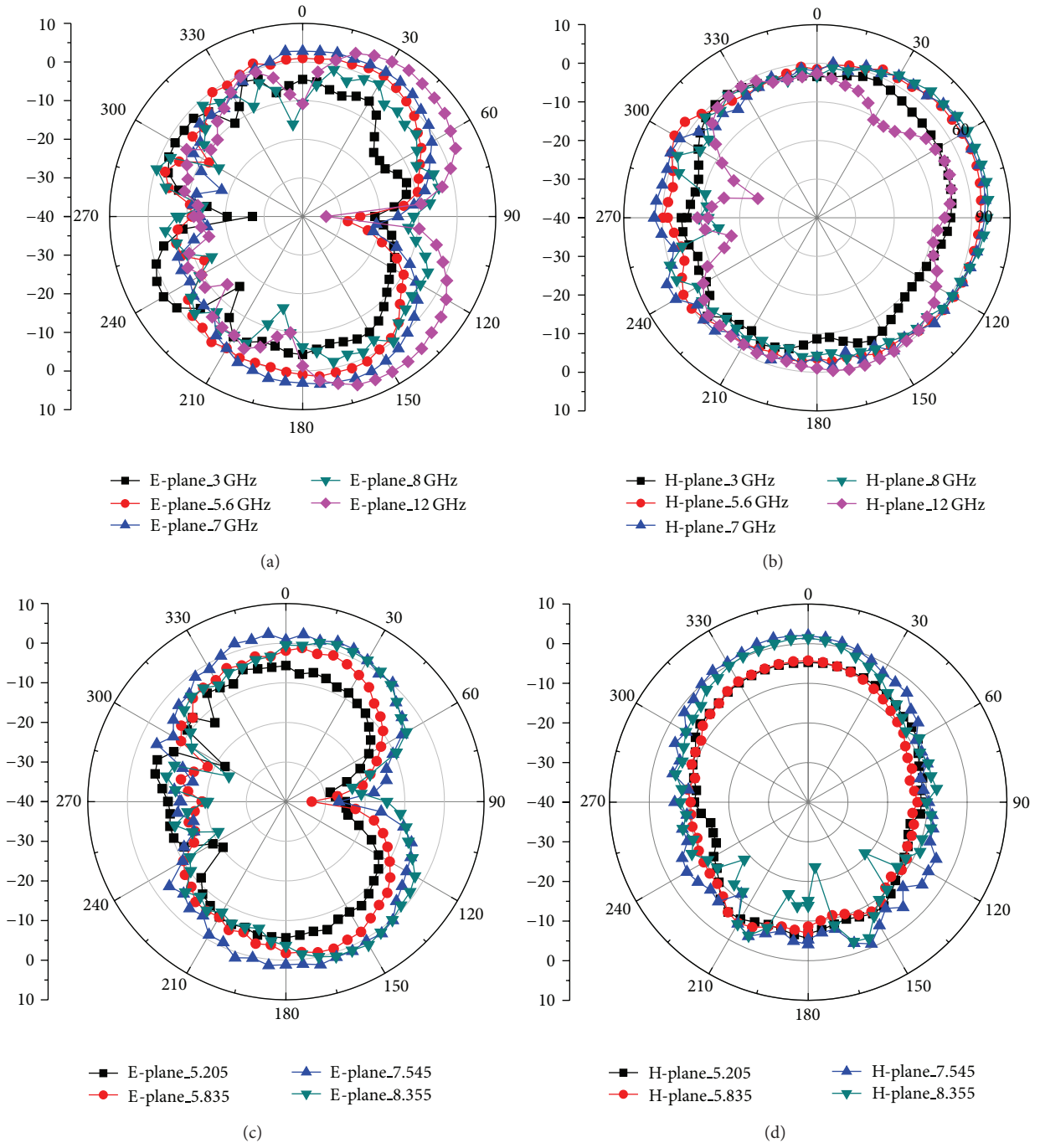

Figure 6: Radiation patterns of the quadruple band-notched UWB antenna.

between the measurement and the simulation results, which may be caused by the interference of the connector and feeding cable in the measurement. The proposed antenna exhibits good wideband performance from 3.1 to 12 GHz with VSWR less than 2, except for the designed four notched bands of 5.1–5.43, 5.78–5.98, 7.2–7.79, and 8.03–8.83 GHz.

The radiation characteristics of the proposed quad band-notched antenna are also measured. The measured far-field radiation patterns of the E-plane and H-plane at the four notched frequencies about 5.205, 5.835, 7.545, and 8.355 GHz and the passband frequencies at 3, 5.6, 7, 8, and 12 GHz are shown in Figures 6(a)–6(d), respectively. At the passband frequencies out of the notched bands, it can be seen from Figures 6(a) and 6(b) that the antenna has good omnidirectional radiation pattern in H-plane, while the antenna E-plane radiation pattern is almost bidirectional. Meanwhile, at the notched-band frequencies, as shown in Figures 6(c) and 6(d), it is noted that the antenna radiation gains reduction due to the slot in the direction of maximum gain.

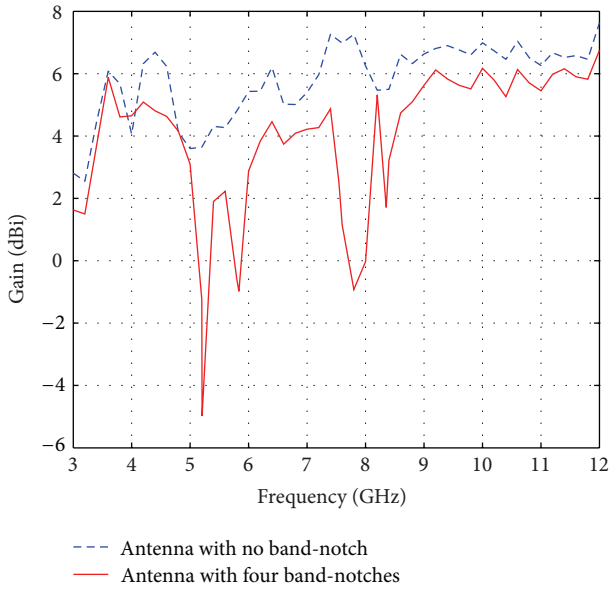

Figure 7: Measured peak gain over the frequency band.

Figure 7 shows the measured peak gains of the proposed antenna with and without the band-notches. It can be seen that there are four sharp decreases of the gain in the antenna at the vicinity of four notched bands. The energy at the notched frequency bands is not radiated so that the radiation efficiency drops at the notched frequency bands. Thus, the peak gain decreases sharply at the four notched bands, which clearly indicates the quad band rejection functions of the proposed antenna.

4. Conclusion

A novel and compact four band-notched UWB antenna is proposed and demonstrated. The proposed antenna exhibits good band rejection in the designed bands and has wideband performance from 3.1 to 12 GHz with VSWR less than 2, covering the entire band of UWB. The fabricated antenna shows good agreement with the simulation and keeps omni-directional radiation performance successfully, which proves it is suitable for UWB applications.

Acknowledgments

The paper is supported by the National Basic Research Program of China (2012CB315704), the National Natural Science Foundation of China (no. 60972003), and the Key Grant Project of the Chinese Ministry of Education under Grant 313049.

References

[1] G. Adamiuk, T. Zwick, and W. Wiesbeck, "UWB antennas for communication systems," *Proceedings of the IEEE*, vol. 100, no. 7, pp. 2308–2321, 2012.

[2] K. S. Ryu and A. A. Kishk, "UWB antenna with single or dual band-notches for lower WLAN band and upper WLAN band," *IEEE Transactions on Antennas and Propagation*, vol. 57, no. 12, pp. 3942–3950, 2009.

[3] L. Li, Z.-L. Zhou, and J. S. Hong, "Compact UWB antenna with four band-notches for UWB applications," *Electronics Letters*, vol. 47, no. 22, pp. 1387–1388, 2011.

[4] C.-Y. Huang, S. A. Huang, and C. F. Yang, "Band-notched ultra-wideband circular slot antenna with inverted C-shaped parasitic strip," *Electronics Letters*, vol. 44, no. 15, pp. 891–892, 2008.

[5] Y. Zhang, W. Hong, C. Yu, Z. Q. Kuai, Y. D. Don, and J. Y. Zhou, "Planar ultrawideband antennas with multiple notched bands based on etched slots on the patch and/or split ring resonators on the feed line," *IEEE Transactions on Antennas and Propagation*, vol. 56, no. 9, pp. 3063–3068, 2008.

[6] J. Xu, D.-Y. Shen, G. T. Wang, X. H. Zhang, X. P. Zhang, and K. Wu, "A small UWB antenna with dual band-notched characteristics," *International Journal of Antennas and Propagation*, vol. 2012, Article ID 656858, 7 pages, 2012.

[7] X. L. Bao and M. J. Ammann, "Printed UWB antenna with coupled slotted element for notch-frequency function," *International Journal of Antennas and Propagation*, vol. 2008, Article ID 713921, 7 pages, 2008.

[8] F. Zhu, S. Gao, A. T. S. Ho et al., "Miniaturized tapered slot antenna with signal rejection in 5-6 GHz band using a balun," *IEEE Antennas and Wireless Propagation Letters*, vol. 11, pp. 507–510, 2012.

[9] G.-M. Zhang, J. S. Hong, and B.-Z. Wang, "Two novel band-notched UWB slot antennas fed by microstrip line," *Progress in Electromagnetics Research*, vol. 78, pp. 209–218, 2008.

[10] W.-S. Lee, D.-Z. Kim, K.-J. Kim, and J.-W. Yu, "Wideband planar monopole antennas with dual band-notched characteristics," *IEEE Transactions on Microwave Theory and Techniques*, vol. 54, no. 6, pp. 2800–2805, 2006.

[11] C. M. Li and L. H. Ye, "Improved dual band-notched uwb slot an-tenna with controllable notched band-widths," *Progress in Electromagnetics Research*, vol. 115, pp. 477–493, 2011.

[12] M. C. Tang, S. Xiao, T. Deng et al., "Compact UWB antenna with multiple band-notches for WiMAX and WLAN," *IEEE Transactions on Antennas and Propagation*, vol. 59, no. 4, pp. 1372–1376, 2011.

[13] T. D. Nguyen, D. H. Lee, and H. C. Park, "Design and analysis of compact printed triple band-notched UWB antenna," *IEEE Antennas and Wireless Propagation Letters*, vol. 10, pp. 403–406, 2011.

[14] W.-T. Li, X.-W. Shi, T.-L. Zhang, and Y. Song, "Novel UWB planar monopole antenna with dual band-notched characteristics," *Microwave and Optical Technology Letters*, vol. 52, no. 1, pp. 48–51, 2010.

[15] A. Foudazi, H. R. Hassani, and S. M. Ali Nezhad, "Small UWB planar monopole antenna with added GPS/GSM/WLAN bands," *IEEE Transactions on Antennas and Propagation*, vol. 60, no. 6, pp. 2987–2992, 2012.

[16] J. Yeo, Y. Lee, and R. Mittra, "Wideband slot antennas for wireless communications," *IEE Proceedings-Microwaves, Antennas and Propagation*, vol. 151, no. 4, pp. 351–355, 2004.

[17] M. A. Habib, A. Bostani, A. Djaiz, M. Nedil, M. C. E. Yagoub, and T. A. Denidni, "Ultra wideband cpw-fed aperture antenna with wlan band rejection," *Progress in Electromagnetics Research*, vol. 106, pp. 17–31, 2010.

Hindawi Publishing Corporation
International Journal of Antennas and Propagation
Volume 2013, Article ID 345908, 6 pages
http://dx.doi.org/10.1155/2013/345908

Research Article

Limits on Estimating Autocorrelation Matrices from Mobile MIMO Measurements

Tricia J. Willink

Communications Research Centre Canada, P.O. Box 11490, Station H, 3701 Carling Avenue, Ottawa, ON, Canada K2H 8S2

Correspondence should be addressed to Tricia J. Willink; tricia.willink@crc.gc.ca

Received 3 December 2012; Accepted 8 January 2013

Academic Editor: Pablo Padilla

On mobile radio links, data samples collected at successive time intervals and at closely spaced frequencies are correlated, so long data records are required to acquire sufficient independent samples for analysis. Statistical analysis of long data records is not reliable because the channel statistics remain wide-sense stationary only over short distances. This is a particular concern for MIMO systems when full autocorrelation matrices may be required for channel modelling or characterisation. MIMO channel responses from mobile measurements in an urban microcell have been used to investigate the limits on estimating autocorrelation matrices, and these are compared to those predicted by commonly used channel models.

1. Introduction

The effectiveness of the spatial processing that provides spectral efficiency gains in MIMO communication systems is dependent on the multipath structure of the channel, that is, the number, powers, and angles of the received multipath components. This structure is highly localised, so in a mobile environment the channel statistics change with time; in other words, the time series of complex channel responses between the transmitter and the receiver is not wide-sense stationary (WSS) except over short distances. This places limits on the length of the time series that can be used to analyse a particular channel characteristic. Within this short time series, there is a finite number of independent channel samples. In the analysis of measured data, therefore, it must be confirmed that there are sufficient independent samples to achieve a valid estimate of the characteristic of interest.

This work addresses the estimation of the full autocorrelation matrix of a MIMO channel. This autocorrelation matrix fully characterises the second order statistics of each of the transmitter-receiver pair links, giving a complete description of a Rayleigh fading MIMO channel; therefore, it has been used extensively in the characterisation and modelling of MIMO channels. For example, it has been applied to decompose the MIMO channel [1], to simulate a correlated MIMO channel [2], to estimate the double-directional angular power spectrum [3], and to evaluate the correlation [4] and diversity [5] of the MIMO channel.

The full autocorrelation matrix is computed using the outer product of channel vectors; hence, the number of independent samples must exceed the dimension of the channel vectors or the autocorrelation matrix estimate will necessarily be rank deficient. The size of the autocorrelation matrix that can be generated is therefore limited by the channel's time and frequency correlation properties as well as the wide-sense stationary interval and signal bandwidth. An important question is then what is the highest dimension mobile MIMO channel that can be characterised using measured data? To answer this, measured data obtained in a typical urban area have been analysed. The results are compared to those that would be obtained using commonly used channel models.

2. Autocorrelation Matrix Estimation

Consider a MIMO radio system with N_t transmit antenna elements and N_r receive antenna elements. The radio channel between transmit element j and receive element i is sampled at intervals kT_s and is represented by the time-varying complex baseband impulse response $h_{ij}(k, \tau)$. The corresponding time-varying frequency transfer function at time kT_s is $H_{ij}(k, n)$, defined at frequency indices $n\Delta f$, obtained as the

discrete Fourier transform of $h_{ij}(k,\tau)$ with respect to delay τ. The $N_r \times N_t$ channel response matrix is then given by $\mathbf{H}(k,n)$, with elements $H_{ij}(k,n)$.

The sample autocorrelation matrix at a single frequency index, n, obtained over the time domain is

$$\widehat{\mathbf{R}}(n) = \frac{1}{N}\sum_{k=1}^{N} \mathrm{vec}(\mathbf{H}(k,n))\,\mathrm{vec}(\mathbf{H}(k,n))^{H}, \quad (1)$$

where vec denotes vectorisation of the matrix and ergodicity is assumed. At least $N_I = N_r \cdot N_t$ independent samples of $\mathbf{H}(k,n)$ are required to ensure that the estimate $\widehat{\mathbf{R}}(n)$ fully reveals the matrix rank: if there are insufficient independent samples, $\widehat{\mathbf{R}}(n)$ will be rank deficient even if the elements of $\mathbf{H}(k,n)$ are uncorrelated.

It is known from [6] that the channel statistics are unlikely to be WSS over distances of more than 2 m in an urban environment at 2 GHz. This can be considered to hold across the UHF band, as the locations of dominant reflecting objects in the local environment, that is, buildings, are the same and their sizes are on the order of many wavelengths, even at the lowest frequency. Estimating statistical functions of the channel response, such as the autocorrelation matrix, must therefore be restricted to intervals that are short enough to be considered WSS.

2.1. Independent Samples. Consider a WSS time series of N samples at intervals T_s, with mean μ and variance σ^2. If the time series is uncorrelated, the variance of the sample mean is $\sigma_m^2 = \sigma^2/N$. However, when the time series is correlated, the variance of the sample mean increases as

$$\sigma_m^2 = \sigma^2 \sum_{k=-(N-1)}^{N-1} \frac{N-|k|}{N^2}\left(\rho(k) - \mu^2\right), \quad (2)$$

where $\rho(k)$ is the normalised correlation coefficient between samples separated by kT_s. It has been shown, for example, in [7, Ch. 5], that the variance of the sample mean does not vanish as T_s increases if the overall duration of the time series remains the same.

As noted in [8, Ch. 3], the number of equivalent independent samples (EIS) in a time series of N correlated samples can be determined by equating the variance of the sample mean to that of a time series of N_I uncorrelated samples. The number of EIS is, therefore, given by

$$N_I = \frac{\sigma^2}{\sigma_m^2} = \left[\sum_{k=-(N-1)}^{N-1} \frac{N-|k|}{N^2}\left(\rho(k) - \mu^2\right)\right]^{-1}. \quad (3)$$

3. Measured Data

Mobile MIMO channel measurements were made in urban Ottawa using available frequency assignments at 2 GHz and 370 MHz, with sounding bandwidths of 25 MHz and 12.5 MHz, respectively. These frequencies are relevant for mobile communications, in particular, personal communications and emergency services and military applications,

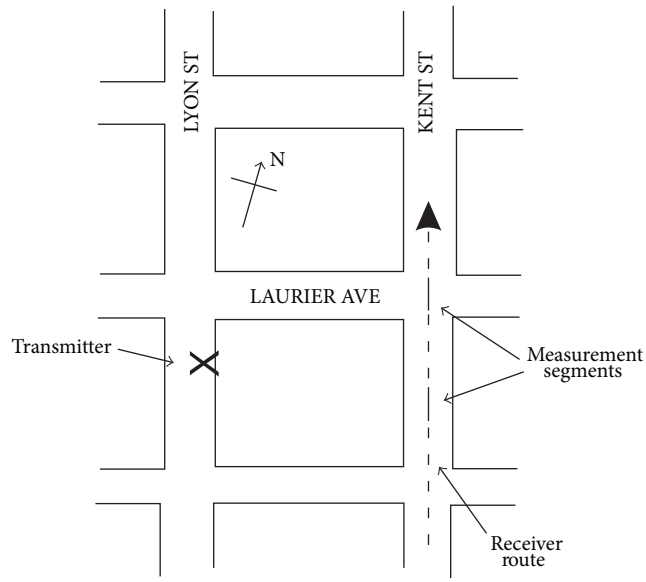

Figure 1: Location of measurement segments in downtown Ottawa, Canada.

respectively. The transmitter was static, with $N_t = 4$ omnidirectional antenna elements arranged in a linear array, spaced at one wavelength for each frequency, and mounted at a height of approximately 3 m. The receiver was mobile and travelled at 30 km/h along a non-line-of-sight route that included intersections and the urban canyon between them. The $N_r = 4$ omnidirectional receiver antennas were mounted on the roof of the measurement van, also in a linear array of one-wavelength spacing with the axis perpendicular to the direction of travel, at a height of approximately 2 m. The location of the measurements is illustrated in Figure 1.

The measurement system and the processing of sampled received data are described in [6]. The measured data yielded $N_r \cdot N_t = 16$ time series of channel impulse response estimates $h_{ij}(k,\tau)$ obtained at intervals of $T_s = 2$ ms, that is, distances of 0.017 m. Each was processed to give the channel transfer function estimates $H_{ij}(k,n)$. The central 20% of each frequency response was retained for analysis, and these frequency components were normalised to have the same average powers over the measurement run; this process retains only channel matrices that have a very high SNR and corrects the spectral shape of the modulated sounding sequence. Two segments of the time series were used, from a mid-block region and an intersection along the measurement route, each 2 s long.

4. Data Analysis

The time series for each measurement segment consisted of 1000 samples, and each was divided into subblocks of 120 samples (0.24 s), corresponding to the 2 m that can be considered WSS [6]. Mean-ergodicity was confirmed by considering the sample covariance, $C(l)$: for each measurement segment, in both the time and frequency dimensions, $(1/L)\sum_{l=0}^{L} C(l)(1 - l/2L)$ decreases monotonically to zero as

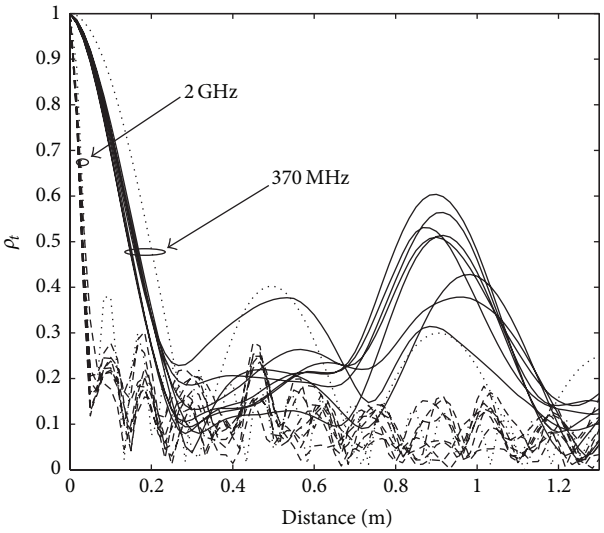

Figure 2: Spatially averaged temporal correlation function for the mid block region at 370 MHz (solid lines) and 2 GHz (dashed lines). The model correlation function at 30 km/hr is also shown (dotted lines).

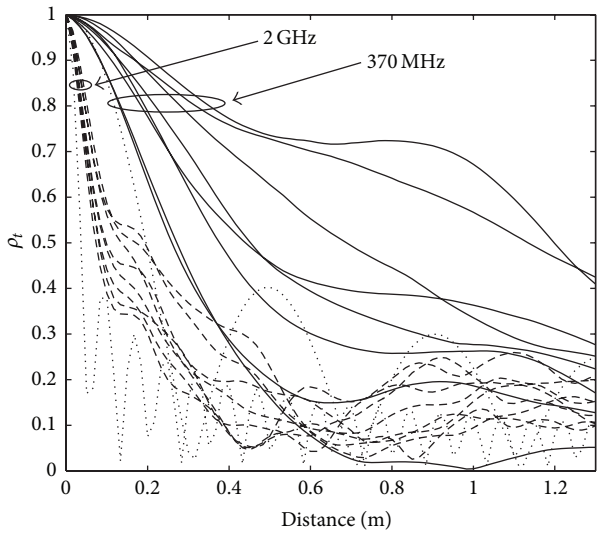

Figure 3: Spatially averaged temporal correlation function for the intersection region at 370 MHz (solid lines) and 2 GHz (dashed lines). The model correlation function at 30 km/hr is also shown (dotted lines).

L is increased to the subblock length. The number of EIS in both time and frequency was investigated, as described below.

4.1. Time Domain. The normalised temporal correlation function estimates were computed for each of the $N_r \cdot N_t$ channel responses as follows:

$$\rho_t(l) = \frac{\mathscr{E}\left\{(H(k,n))(H(k+l,n))^*\right\}}{\mathscr{E}\left\{|H(k,n)|^2\right\}}, \quad (4)$$

where the subscripts on $H(k,n)$ have been dropped for convenience. The expectations were taken over the time and frequency dimensions of each subblock. The autocorrelation functions $\rho_t(l)$ were then averaged over the $N_r \cdot N_t = 16$ spatial channels.

Figures 2 and 3 show the space-averaged autocorrelation functions for the mid-block and intersection regions, respectively. The correlation function for the uniform scatterer model, with a Clarke Doppler power spectral density [9, Ch. 5], is also shown; that is,

$$\rho_t(\Delta t) = J_0\left(2\pi F_d \Delta t\right), \quad (5)$$

where J_0 is the zeroth order Bessel function of the first kind and F_d is the maximum Doppler frequency. At 30 km/hr, $F_d = 55.6$ Hz at 2 GHz and 10 Hz at 370 MHz. In the mid-block region, the measured correlation functions vary only a small amount over each of the eight 2 m long subblocks, whereas there is considerable variation in the intersection. The measured data in the mid-block region is also better represented by the model, although the accuracy is not high. This is because the model is based on the assumption of many multipath components arriving with random amplitudes and uniformly distributed angles of arrival. In practice, within an urban canyon, the strongest multipath components arrive from angles close to the front and/or rear of the vehicle, and not from the sides [6]. In the intersection, as seen in [10], the signal power arrives predominantly from the side, along the direction of the intersecting street, with some reflections off the buildings on opposite corners. These directional components lead to higher temporal correlations and greater variation from subblock to subblock as the angles of arrival change with distance.

The number of EIS was obtained by applying (3) to the correlation function computed for each subblock and averaging. The results are shown in Figure 4 for each frequency and region, along with the number of EIS expected when using the idealised model (5). As expected, the number of EIS is larger at the higher frequency, as the correlation function decreases more rapidly with delay or distance. The average number of EIS is greater in the mid-block region than in the intersection, but none of the measured data provide the number of EIS predicted by the model. As noted above, the spatial characteristics of the observed multipath are not matched by the assumptions in the model.

The asymptotic behaviour is of particular significance. While the model predicts an increase in EIS of 1.75 per 10 ms at 2 GHz and 0.33 per 10 ms at 370 MHz, for the measured data the observed EIS increases are approximately 0.1–0.2 per 10 ms at 2 GHz and 0.05–0.15 per 10 ms at 370 MHz. This is because $\rho_t(l)$ is much greater for large delays, l, than predicted by the model, as shown in Figures 2 and 3, which significantly reduces N_I (3).

4.2. Frequency Domain. The normalised frequency correlation function estimates were estimated for each subblock and for each element in the channel matrix time series using

$$\rho_f(m) = \frac{\mathscr{E}\left\{(H(k,n))(H(k,n+m))^*\right\}}{\mathscr{E}\left\{|H(k,n)|^2\right\}} \quad (6)$$

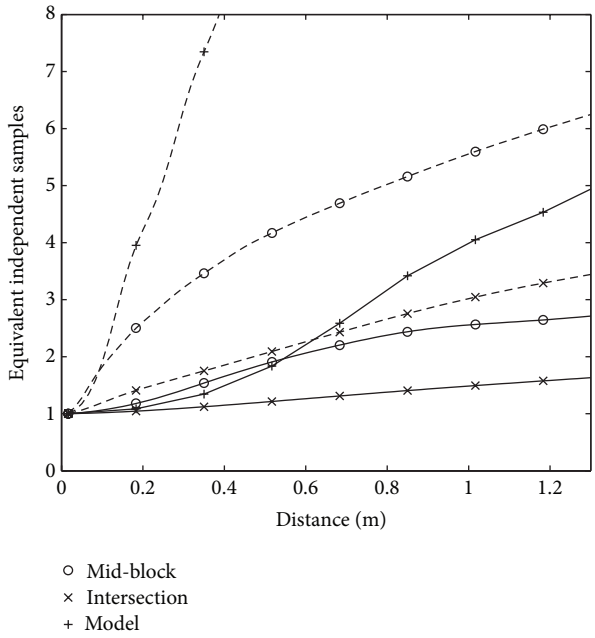

Figure 4: Average equivalent independent samples for time-correlated data at 30 km/hr for 370 MHz (solid lines) and 2 GHz (dashed lines) and for the Clarke Doppler model (5).

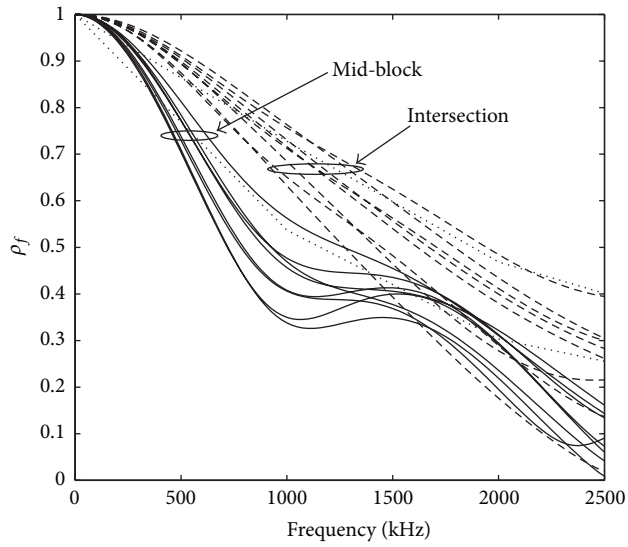

Figure 5: Spatially averaged frequency correlation function at 2 GHz for the mid-block region (solid lines) and the intersection (dashed lines). The model correlation functions for $\tau_0 = 0.25\,\mu$s and $\tau_0 = 0.15\,\mu$s are also shown (dotted lines).

and were then averaged over the $N_r \cdot N_t = 16$ spatial channels. The necessity to the average over time as well as frequency when computing a frequency correlation estimate was pointed out in [11], as a single snapshot in time represents only one relationship of multipath phases and amplitudes. The variation across the subblocks is quite small, as shown in Figure 5 for the 2 GHz measurements, and is similar for both frequencies and regions.

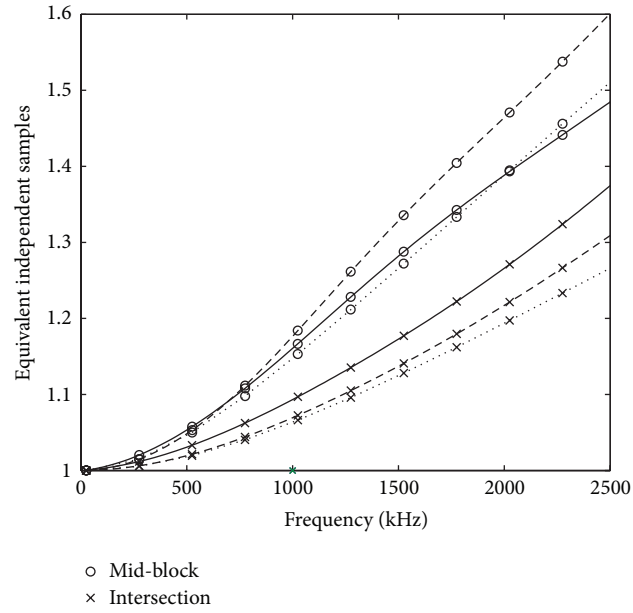

Figure 6: Average equivalent independent samples for frequency-correlated data at 370 MHz (solid lines) and 2 GHz (dashed lines) and for exponential delay model (7) (dotted lines).

The number of EIS was then computed for each subblock using (3), and the average is shown in Figure 6 for each frequency and region. The figure also shows the number of EIS computed for the exponential delay profile model [9, Ch. 7], which has the correlation function

$$\rho_f(\Delta f) = \left(1 + j2\pi\tau_0\Delta f\right)^{-1}, \tag{7}$$

where τ_0 is the root-mean-square delay spread. From the measured data, τ_0 was estimated to be 0.25 μs in the mid-block region and 0.15 μs in the intersection. The computed model correlation functions are shown in Figure 5.

The numbers of EIS over the bandwidths considered here, which are limited by the measurement bandwidth, are very small. At both 370 MHz and 2 GHz, the number of EIS per bandwidth is greater in the mid-block region where a richer multipath environment results in a larger delay spread and therefore a reduced correlation across the channel bandwidth.

The measured channel impulse responses do not follow a simple exponential delay profile but are better modelled using multiple clusters of multipath components, as described in [9, Ch. 7]. In spite of this, the simple and tractable exponential delay profile model, using an appropriate rms delay spread parameter, does provide a good estimate of the EIS. This is because the rms delay spread is strongly related to the frequency correlation, and the parameterisation of τ_0 leads to a reasonably representative correlation function even if the delay profile itself is not accurately represented, as shown in Figure 5. The EIS for the measured data slightly exceed those of the model, because the measured correlation function (Figure 5) tends to decay faster than that of the model; however, this simple model does lead to similar asymptotic

behaviour, with measurements and model predicting an increase of approximately 0.15–0.25 EIS per 1000 kHz.

5. Discussion

The analysis of measured data indicates that the full autocorrelation matrix, **R**, can be generated only for a small number of antenna elements in urban environments. The main limitation is the distance over which the time series of channel responses can be considered to be WSS. This distance has been estimated to be approximately 2 m in the type of environment considered here. The time correlation model that is usually considered, with a Clarke Doppler power spectral density, indicates that there are approximately 8 and 42 independent samples in 2 m, at 30 km/hr, for 370 MHz and 2 GHz, respectively. For a MIMO system with $N_r = N_t$, the autocorrelation matrix can then be estimated for maximum array sizes of 2 and 6, respectively.

The impact of insufficient independent samples is illustrated in Figure 7, which shows the average estimated diversity, using the diversity metric proposed in [5]. The narrowband channel is modelled using $N_t = N_r = 4$, $R_{ii} = 1$, and $R_{ij} = \rho$, for $i \neq j$, for $i, j = 1, \ldots, 16$, using a Clarke fading model at a carrier frequency of 2 GHz and a speed of 30 km/hr. The diversity metric is given by [5]

$$\Phi = \frac{\left[\sum_{i=1}^{N_t \cdot N_r} \lambda_i\right]^2}{\sum_{i=1}^{N_t \cdot N_r} \lambda_i^2}, \tag{8}$$

where λ_i, $i = 1, \ldots N_t \cdot N_r$, are the eigenvalues of the autocorrelation matrix estimate $\widehat{\mathbf{R}}$ in (1), and the channel is sampled at intervals $T_s = 5$ ms. For the spatially uncorrelated channel, the diversity is significantly underestimated for distances even up to 8 m. This deficit is reduced as the spatial correlation increases, but even for $\rho = 0.3$, there are not enough independent samples in a measurement length of 2 m to fully reveal the rank of $\widehat{\mathbf{R}}$, resulting in an underestimation of the diversity by approximately one unit.

In practice, the assumptions of rich, uniformly distributed scattering are not met in this urban environment. The number of equivalent independent samples over 2 m is actually observed to be between 3 and 4 at 370 MHz and between 6 and 9 at 2 GHz. The richer multipath scattering environment of the mid-block region provides more EIS than that in the intersection, where there is a small number of dominant multipath components.

The frequency domain does not provide much to supplement the number of EIS. For a measurable bandwidth of 10 MHz, less than 3 EIS are achieved, depending on the local environment. At 100 MHz, based on the exponential power delay profile model, this would increase from 10 to 16 EIS, which is sufficient to estimate arrays with $N_r = N_t = 4$ in a mid-block region, but not in an intersection. In [12], measurements with $N_t = N_r = 4$ were reported for a bandwidth of 240 MHz, at a carrier frequency of 5.2 GHz; the analysis presented herein indicates that averaging over a bandwidth that large would certainly provide sufficient independent samples to generate the full autocorrelation matrix,

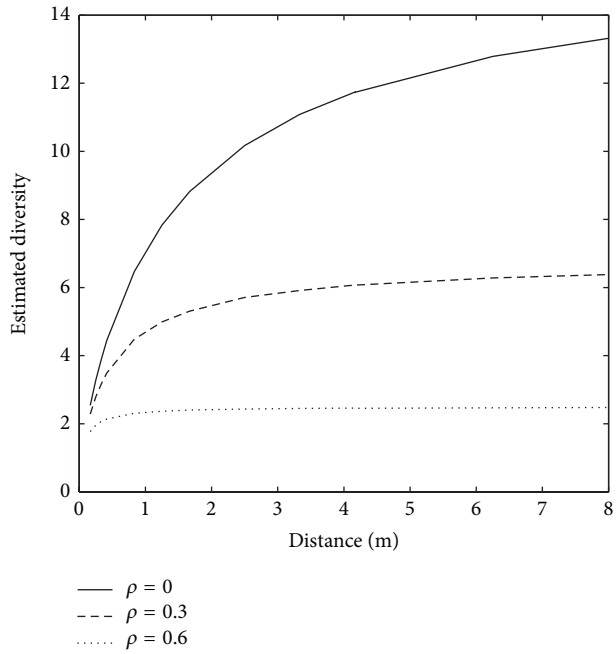

Figure 7: Estimated diversity (8) for correlated fading model at 30 km/hr for 2 GHz.

assuming a typical urban delay profile. The higher frequency also enables more independent samples to be obtained over the same measurement distance than for the 2 GHz results reported herein. Obtaining such a large spectrum assignment for measurements, especially at lower frequencies, can be difficult, so in general care must be taken to ensure that the bandwidth used does indeed provide enough equivalent independent samples such that the autocorrelation matrix will not necessarily be rank deficient.

For the measurements presented, combining both time and frequency domains for a measurable bandwidth of 2 MHz and distance of 2 m at 30 km/hr, the autocorrelation matrix **R** cannot be generated for more than $N_r = N_t = 2$ at 370 MHz nor for more than $N_r = N_t = 3$ at 2 GHz. Note that this only ensures the estimated autocorrelation matrix is not rank deficient, as analysed [13, Ch. 5]; the accuracy of the estimate also depends on the number of independent samples.

6. Conclusions

The analysis of mobile MIMO measurement data reported herein has shown that the estimation of the full autocorrelation matrix, **R**, should be restricted to small numbers of antenna elements due to the limited number of independent samples in a typical wide-sense stationary interval. Estimating **R** with too few independent samples will prevent its full rank from being revealed. If the channel bandwidth is very large and the channel's delay spread is sufficiently large; that is, it has a sufficiently small correlation bandwidth, averaging the autocorrelation matrix across the bandwidth as well as in time will help supplement the number of equivalent

independent samples. The number of EIS is dependent on the local environment as well as operating frequency, with more EIS in the mid-block region than in the intersection. Conventional fading models do not provide good estimates of EIS for localised measurements because the assumptions used in their derivations are often not satisfied, but it has been seen that simple delay profile models may be more useful if appropriately parameterised.

References

[1] W. Weichselberger, "On the decomposition of the MIMO channel correlation tensor," in *Proceedings of the ITG Workshop on Smart Antennas*, pp. 268–273, March 2004.

[2] J. P. Kermoal, L. Schumacher, K. I. Pedersen, P. E. Mogensen, and F. Frederiksen, "A stochastic MIMO radio channel model with experimental validation," *IEEE Journal on Selected Areas in Communications*, vol. 20, no. 6, pp. 1211–1226, 2002.

[3] H. Özcelik, N. Czink, and E. Bonek, "What makes a good MIMO channel model?" in *Proceedings of the IEEE 61st Vehicular Technology Conference (VTC '05)*, vol. 1, pp. 156–160, Stockholm, Sweden, May 2005.

[4] D. S. Shiu, G. J. Foschini, M. J. Gans, and J. M. Kahn, "Fading correlation and its effect on the capacity of multielement antenna systems," *IEEE Transactions on Communications*, vol. 48, no. 3, pp. 502–513, 2000.

[5] M. Ivrlač and J. Nossek, "Quantifying diversity and correlation in Rayleigh fading MIMO communication systems," in *Proceedings of the 3rd IEEE International Symposium on Signal Processing and Information Technology (ISSPIT '03)*, pp. 158–161, December 2003.

[6] T. J. Willink, "Wide-sense stationarity of mobile MIMO radio channels," *IEEE Transactions on Vehicular Technology*, vol. 57, no. 2, pp. 704–714, 2008.

[7] W. B. Davenport and W. L. Root, *An Introduction to the Theory of Random Signals and Noise*, McGraw-Hill, 1958.

[8] F. E. Nathanson, J. P. Reilly, and M. N. Cohen, *Radar Design Principles: Signal Processing and the Environment*, SciTech Publishing, 1999.

[9] A. F. Molisch, *Wireless Communications*, John Wiley & Sons, 2005.

[10] C. C. Squires and T. J. Willink, "Impact of vehicular array position on urban MIMO channel characteristics," *International Journal of Antennas and Propagation*, vol. 2011, Article ID 675343, 14 pages, 2011.

[11] R. J. C. Bultitude, "Estimating frequency correlation functions from propagation measurements on fading radio channels: a critical review," *IEEE Journal on Selected Areas in Communications*, vol. 20, no. 6, pp. 1133–1143, 2002.

[12] A. Paier, T. Zemen, J. Karedal et al., "Spatial diversity and spatial correlation evaluation of measured vehicle-to-vehicle radio channels at 5.2 GHz," in *Proceedings of the IEEE 13th Digital Signal Processing Workshop*, pp. 326–330, January 2009.

[13] Y. Eldar and G. Kutyniok, Eds., *Compressed Sensing, Theory and Applications*, Cambridge University Press, 2012.